TECHNISCHE UNIVERSITÄT WIEN

Dissertation

The ASACUSA Antihydrogen Detector: Development and Data Analysis

Ausgeführt zum Zwecke der Erlangung des akademischen Grades eines Doktors der technischen Wissenschaften, unter der Leitung von

Hon.-Prof. Dipl.-Phys. Dr. Eberhard Widmann

am Stefan-Meyer-Institut für subatomare Physik der Österreichischen Akademie der Wissenschaften.

Eingereicht an der Technischen Universität Wien, Fakultät für Physik,

von

Dipl.-Ing. Clemens Sauerzopf, BSc

Matrikelnummer 0625446
Untere Hauptstraße 57, 7122 Gols

_____   _____
Ort, am Datum   Unterschrift (C. Sauerzopf)

Kurzfassung

Die theoretische Beschreibung der Natur im Rahmen des Standardmodells der Teilchenphysik enthält eine Vielzahl an Symmetrien. Die fundamentalste ist die kombinierte Symmetrie aus Ladungsumkehr-, Paritäts- und Zeitumkehrsymmetrie ($\mathcal{CPT}$ Symmetrie). Nach allen verfügbaren experimentellen Befunden wurde bisher keine Verletzung dieser Symmetrie gefunden. Die ASACUSA Kollaboration am „Antiproton Deceleator" der Europäische Organisation für Kernforschung, CERN, versucht Übergänge in der Hyperfeinstruktur im Grundzustand von Antiwasserstoff zu messen. Antiwasserstoff ist das leichteste Element das vollständig aus Antimaterie besteht. Durch den Vergleich der Übergangsfrequenzen mit seinem Materie-Äquivalent, Wasserstoff, erlaubt diese Messung ein direktes Testen der $\mathcal{CPT}$ Symmetrie.

Im Rahmen dieser Dissertationsschrift wurde ein Detektorsystem entwickelt, um die Annihilation der Antiatome am Ende des experimentellen Aufbaus nachzuweisen. Im Rahmen der vorliegenden Arbeit wird der vollständige Aufbau des Detektors, inklusive der Datenerfassung und Steuerung beschrieben. Besonders Augenmerk wird auf die Elektronik des Systems, die Funktionsweise der Datenaufnahme und die Struktur der gemessenen Daten gelegt.

Mit dem Detektorsystem aufgezeichnete Daten wurden mittels bayesianischer Methoden analysiert. Es wird sowohl die Identifikation der Annihilationen und ihre Unterscheidung von Untergrundereignissen, als auch die tatsächliche statistische Analyse im Detail erläutert. Abschließend wird, aufbauend auf die statistische Analyse, die Signifikanz der erhobenen Daten und der Nachweis von Antiwasserstoff-Annihilationen im Detektor präsentiert.

Abstract

The theoretical description of nature, within the standard model framework of particle physics, gives rise to a manifold of different symmetries. The most fundamental one is the combined symmetry of charge conjugation, parity transformation, and time reversal ($\mathcal{CPT}$ symmetry). Currently all experimental evidence opposes the idea of a broken $\mathcal{CPT}$ symmetry. The ASACUSA collaboration, at the "Antiproton Decelerator", at the European Organisation for Nuclear Research (CERN), tries to measure the ground state hyperfine splitting of antihydrogen. By comparing this splitting with the similar signal in ordinary hydrogen, the $\mathcal{CPT}$ symmetry can be directly tested.

During the course of this thesis, a detector system for detecting annihilations from antihydrogen at the end of the experimental setup was developed. In this work the construction of the detector will be described in detail, including control and data acquisition of the setup. A special focus will be on the electronic components, the inner working of the data acquisition, and the structure of the measured data.

The recorded data was analysed using Bayesian methods. Both, the identification of annihilation events and their consequent distinction from background signals, and the statistical analysis of the data are covered in detail. Finally, based on the statistical analysis, the data significance is presented.

Dissertation

The ASACUSA Antihydrogen Detector: Development and Data Analysis

Clemens Sauerzopf

10th March 2016

Danksagung

Contents

List of Tables

List of Figures

1. Introduction

The hydrogen atom is known to be the most abundant element in the observable universe. It is as well the most simple atomic system built only from a proton as nucleus and one single electron in its shell. Its simplicity allows analytical calculations and was the cornerstone for the development of the atomic models.

On the other hand, antimatter is very rare in our observable universe. This baryon asymmetry can be partly explained by a $\mathcal{CP}$ (charge and parity) violation as being one of the Sakharov criteria [1]. Although this qualitative explanation is sound, a quantitative explanation is still lacking. An investigation of these problems can be done by directly comparing ordinary matter with antimatter with precision experiments.

The first discovered anti particles in 1932 by Carl David Anderson [2] was named positron. It is the positively charged antimatter counterpart of the electron. This observation fitted well to the interpretation of Paul Dirac's equation as a "sea" of particles where antimatter would be a negative energy state [3]. In 1955 the antimatter counterpart of the proton, named the antiproton was discovered by Emilio Segrè and Owen Chamberlain [4].

In 1996 the first bound atomic structures made purely of antimatter, antihydrogen atoms, were produced [5] at Organisation Européene pour la Recherche Nucléaire (CERN) and later confirmed by Fermilab [6]. The first anti atoms were very hot and not usable for precision experiments. At the CERNs Antiproton Decelerator (AD) facility the first cold antihydrogen was created in 2002 [7, 8]. In addition to antihydrogen also antideuteron nuclei [9], and antihelium has been produced [10–12] in very hot and in very small quantities.

1.1. Motivation

The preservation of the combined charge, parity and time symmetry ($\mathcal{CPT}$) together with the invariance under Poincaré transformations is the backbone of the standard model of particle physics and as such should be constantly questioned [13, 14].

For investigating the relations between matter and antimatter, a theoretical guideline is preferable. There is no fully developed theory that incorporates a violation of the $\mathcal{CPT}$ symmetry or of the invariance under Lorentz transformations. A minimal extension of the standard model is available [15] that includes both $\mathcal{CPT}$ and Lorentz violating terms. With the charge q, the mass m_e , the Coulomb potential A^μ and $iD_\mu := i\partial_\mu - qA_\mu$, the standard model extension (SME) for free hydrogen and antihydrogen is [15]:

$$\left(i\gamma^\mu D_\mu - m_e - a^e_\mu \gamma^\mu - b^e_\mu \gamma_5 \gamma^\mu + \frac{1}{2} H^e_{\mu\nu} \sigma^{\mu\nu} + ic^e_{\mu\nu} \gamma^\mu D^\nu + id^e_{\mu\nu} \gamma_5 \gamma^\mu D^\nu \right) \psi = 0.$$

(1.1)

Components highlighted in red mark Lorentz and $\mathcal{CPT}$ violating terms, components in blue violate only Lorentz invariance.

The atomic transitions in hydrogen are among the most precisely understood quantities in physics. For experimental results, relative precisions of 12 orders of magnitude are possible [16]. In case of the 1S-2S transitions the leading order energy shifts for hydrogen and antihydrogen are identical within the SME framework. In case of hyperfine transitions in the ground state, some of the Lorentz and $\mathcal{CPT}$ violating coefficients contribute to an energy shift. The coefficients have the dimension of an energy. Therefore, a good relative measurement precision is not enough, precision on an absolute energy scale is required for investigating $\mathcal{CPT}$ and Lorentz violating components [15].

In addition to the minimal SME a non-minimal extension is available [17]. The main difference between those two extensions is that the minimal model only includes operators of rank $\leq$4. Relaxing this condition gives rise to an infinite amount of additional $\mathcal{CPT}$ and Lorentz violating coefficients. For the non-minimal SME also the 1S-2S transition would acquire energy shifts from a violation of the $\mathcal{CPT}$ symmetry.

A summary table with current limits for $\mathcal{CPT}$ and Lorentz violation and all available components and operators can be found in the "Data tables for Lorentz and $\mathcal{CPT}$ violation" [18, better arXiv:0801.0287].
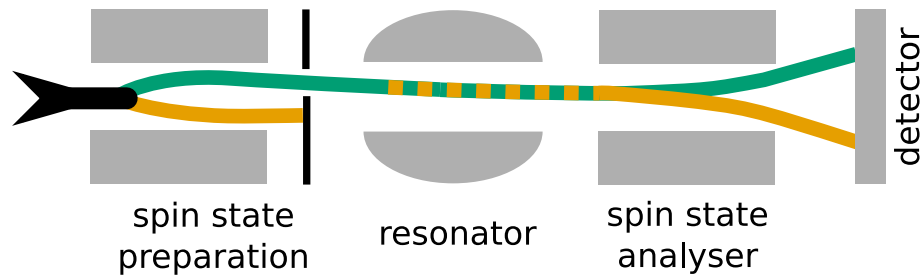
Figure 1.1.: Schematic overview showing the Rabi method. The primary unpolarised beam enters the setup from the left side. In the spin state separation stage the beam is split into two spin states and one of them is removed from the beam. Inside the resonator the atoms can undergo a transition between the two states. Finally, the analyser separates the states again before the beam reaches a detector.

The prominent 21 cm (1.4 GHz) ground state hyperfine line, conventionally named "The hydrogen line" in astrophysics, is know with an absolute precision of 1 mHz. Following the arguments given above, and [15, 17] the ground state hyperfine transition is a viable candidate to investigate possible violations of the $\mathcal{CPT}$ symmetry within the framework of the SME. Consequently, the line was chosen by the Atomic Spectroscopy And Collisions Using Slow Antiprotons (ASACUSA) collaboration at the CERN AD facility to investigate the differences between matter and antimatter.

1.2. The Rabi method

The most precise experiments to determine the ground state hyperfine splitting of hydrogen were performed with a hydrogen maser. Unfortunately, this type of experiment is currently out of question for antihydrogen due to the technical difficulties involved when constructing a box of anti Polytetrafluorethylen (PTFE).

The most sensible approach is building a Rabi-like experimental setup [19]. In Figure 1.1 a schematic graph of a Rabi type apparatus is shown.

The Rabi experiment uses a beam of atomic hydrogen. When entering the apparatus the atoms undergo a spin state selection by passing a strong inhomogeneous magnetic field

similar to the field of a Stern-Gerlach apparatus. The states are split by their magnetic moment and half of the beam is discarded by an aperture.

The polarised beam then passes through a resonator with an oscillating[1] magnetic field. By selecting the appropriate frequency a spin flip can be induced, changing the orientation of the magnetic moment of the atom.

The resonator is followed by another Stern-Gerlach type magnetic field analysing the spin states by spacial separation on the detection plane. By evaluating the beam intensities for the separated states in dependence of the resonator frequency the resonance line for the transition can be recorded.

An apparatus following the principle of the Rabi experiment was constructed by the ASACUSA collaboration in order to measure the ground state hyperfine splitting of antihydrogen. The spectroscopy beamline will be presented in section 3.3. This thesis focuses on the antihydrogen detection stage for the experiment (chapter 5) and the analysis of the recorded data (chapter 6).

---

[1]Rabi's original experiment used a rotating magnetic field produced by four wires being switched with a high current.

2. Theory

Antihydrogen, as the $\mathcal{CPT}$ conjugate counterpart to hydrogen, is the simplest atom which is built purely of antimatter. All calculations for hydrogen can be easily adapted to antihydrogen. In this chapter the basic theoretical framework for calculating the ground state hyperfine splitting of antihydrogen and hydrogen will be presented. All calculations in this chapter are textbook knowledge. As consequence only the necessary calculations for understanding this thesis will be covered. Consequently, only the vector quantities are written in bold letters (e.g. $\mathbf{B}$), operators are marked with a circumflex (e.g. $\hat{\boldsymbol{\mu}}$) and expectation values of operators carry a bar on top (e.g. $\bar{\mathcal{H}}$). The arguments in this section follow the book "Quantum Mechanics of One- and Two-Electron Atoms" ([20, chapter III, a]).

Calculating the hyperfine structure of hydrogen requires a similar ansatz as for the Zeemann effect:

$$\mathcal{H} = -\hat{\boldsymbol{\mu}}\mathbf{B} \quad \hat{\boldsymbol{\mu}} = g_n \mu_n \hat{\mathbf{I}} \tag{2.1}$$

with $\hat{\boldsymbol{\mu}}$ as the operator for the magnetic moment, the magnetic flux density $\mathbf{B}$, the gyromagnetic factor of the nucleus (g_n), the nuclear magneton (μ_n) and the nuclear spin operator $\hat{\mathbf{I}}$. The Hamilton operator $\mathcal{H}$ can be split into two independent components, one for the external magnetic field and one for the coupling between electron and nuclear spin [20, section 47.γ]:

$$\mathcal{H} = \underbrace{A g_n \hat{\mathbf{I}}\hat{\mathbf{J}}}_{\mathcal{H}'} - \underbrace{\hat{\boldsymbol{\mu}}\mathbf{B}_{\text{ext}}}_{\mathcal{H}''} \tag{2.2}$$

with A being the zero field hyperfine structure constant, $\hat{\mathbf{J}}$ is the total angular momentum operator and $\mathbf{B}_{\text{ext}}$ denotes the external magnetic field. $\mathcal{H}''$ represents the interaction with the external magnetic field. The operator $\mathcal{H}'$ on the other hand represents the magnetic coupling between the nuclear and the electron spin. When analysing the case of a vanishing external field ($\mathbf{B}_{\text{ext}} = 0$) the coupling between $\hat{\mathbf{I}}\hat{\mathbf{J}}$ can be solved in a

similar fashion as the coupling between electron spin and orbital angular momentum by introducing a new quantum number $\hat{\mathbf{F}} = \hat{\mathbf{I}} + \hat{\mathbf{J}}$ with Eigenvalues for $\hat{\mathbf{F}}^2 = F(F+1)$. This directly leads to $\hat{\mathbf{I}}\hat{\mathbf{J}} = 0.5(\hat{\mathbf{F}}^2 + \hat{\mathbf{I}}^2 + \hat{\mathbf{J}}^2)$ which in turn solves the Eigenproblem for

$$\bar{\mathcal{H}}' = Ag_n \frac{1}{2} \left(F(F+1) + I(I+1) + J(J+1) \right). \tag{2.3}$$

Hydrogen is built from one proton and one electron, and antihydrogen is built from one antiproton and one positron. Therefore, it is possible to simplify expression (2.3) by selecting $I = \frac{1}{2}$ and $J = \frac{1}{2}$, fixing the calculation to the ground state. By this method F reduces to a two level system with the allowed states $F = 0$ and $F = 1$. The energy difference ΔE between the two hyperfine states is then given by:

$$\Delta E = Ag_n = h\nu_{HF}, \tag{2.4}$$

allowing to identify the ΔE and the hyperfine structure constant for the ground state of hydrogen and antihydrogen with the Planck constant h and the ground state hyperfine level splitting ν_{HF} of hydrogen. The transition frequency ν_{HF} is one of the most precisely determined physical quantities and was measured to be [16, 21–24]:

$$\nu_{HF} = 1420405751.768 \pm 0.001 \text{ Hz}. \tag{2.5}$$

The general solution for equation (2.2) is a longish calculation. By defining the reduced magnetic flux density χ:

$$\chi = \frac{\mu_B |\mathbf{B}|(g_j - \frac{g_n \mu_n}{\mu_B})}{h\nu_{HF}} \approx \frac{2\mu_B |\mathbf{B}|}{h\nu_{HF}} \tag{2.6}$$

with μ_B representing the Bohr magneton, the Landé-factor of the coupled spin and angular momentum (g_j equals the Landé-factor of the electron g_e for J=1/2) and the approximation $\frac{g_n \mu_n}{\mu_B} \approx 0$. The famous Breit-Rabi formula for the ground state energy shift $E_\pm$ emerges [25, 26]. Differences between hydrogen ($E_\pm(H)$) and antihydrogen ($E_\pm(\bar{H})$) are highlighted in red in equation (2.7) and (2.8):

$$E_{\pm}(H) = -g_n\mu_n|\mathbf{B}| \pm \frac{\Delta E}{2}\sqrt{1 - \frac{4m_F}{2}\chi + \chi^2} \qquad (2.7)$$

The F quantum number can either take the value 0 or 1. It is indicated by $\pm$ ("$-$" for F=0 and "$+$" for F=1) and splits the ground state into one singlet state ($F = 0$, $m_F = 0$) and a triplet state ($F = 1$, $m_F = [-1, 0, 1]$). Due to the $\mathcal{CPT}$ conjugation, the Breit-Rabi formula for antihydrogen is slightly different. The states $|F = 1, m_F = 1 >$ and $|F = 1, m_F = -1 >$ exchange their energy. This behaviour follows from an additional phase of π acquired by the $\mathcal{CPT}$ conjugation.

The effect can be understood qualitatively by imagining a point like particle orbiting the nucleus, when inverting the charge ($\mathcal{C}$) the direction of the induced magnetic field flips, by performing a parity transformation ($\mathcal{P}$) the direction of movement is reversed and the magnetic field has its original orientation. Now after reversing the flow of time ($\mathcal{T}$) the field direction is again flipped.

It follows that one would need to change the signs of the Landé-factors (g_j and g_n) in the definition of the reduced magnetic field χ for the transition between hydrogen and antihydrogen. By removing the additional factor of -1 the only effect of this change is the highlighted sign in equation (2.7). This way, the matter Landé-factors can be used in χ even for antihydrogen.

As a consequence, the Breit-Rabi formula for antihydrogen reads:

$$E_{\pm}(\bar{H}) = -g_n\mu_n|\mathbf{B}| \pm \frac{\Delta E}{2}\sqrt{1 + \frac{4m_F}{2}\chi + \chi^2} \qquad (2.8)$$

In Figure 2.1 the energy shifts calculated in equation (2.7) and (2.8) are shown together with the microwave transitions σ_1 and π_1. Both transitions can be measured with the ASACUSA apparatus. The σ_1 transitions does not involve a change of the magnetic quantum number m_F within the SME. Therefore, the transition is $\mathcal{CPT}$ even, whereas π_1 is a $\mathcal{CPT}$ odd transition. It can be calculated that $\mathcal{CPT}$ violating terms would contribute to $\mathcal{CPT}$ odd transitions [15, 17].
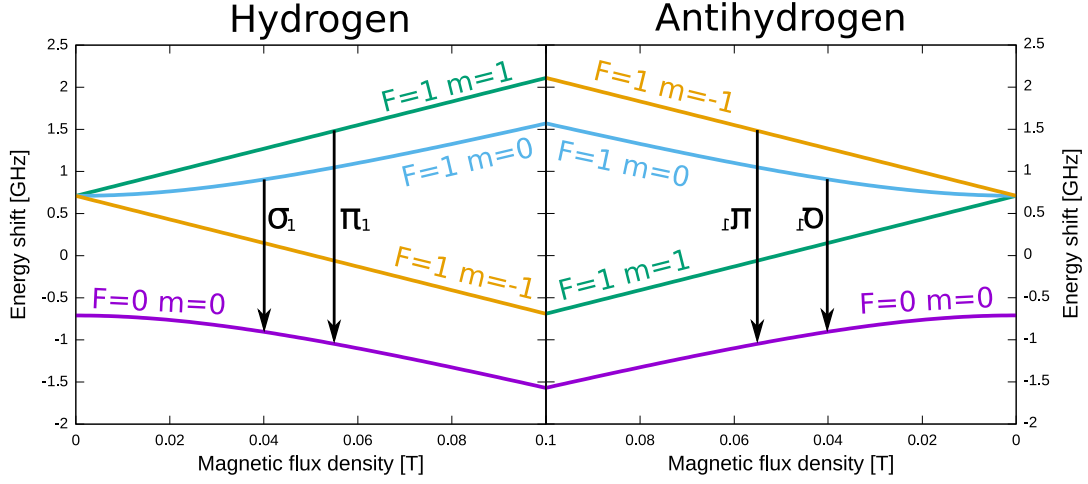
Figure 2.1.: Breit Rabi diagram for hydrogen and antihydrogen. The microwave transitions σ_1 and π_1 are measurable with the ASACUSA microwave cavity (compare section 3.3). States with a magnetic quantum number 1 or -1 are exchanged when moving from a matter to an antimatter system.

From equation (2.8) and (2.7) the magnetic moments (μ) dependence on an external magnetic field and the quantum numbers F and m_F are calculated by using the relations[1]

$$E = -\mu B; \quad F = -\nabla E = -\frac{dE}{d|\mathbf{B}|}\nabla|\mathbf{B}|; \quad -\nabla E = \nabla(\mu \mathbf{B}) = \mu \nabla(|\mathbf{B}|). \tag{2.9}$$

F represents the force in equation (2.9). The relation holds under the assumption that μ and $\mathbf{B}$ are aligned (assuming adiabaticity). In the case of hydrogen, the derivative of the Breit-Rabi formula with respect to the total magnetic field yields[2]

$$-\frac{\partial E_\pm(H)}{\partial|\mathbf{B}|} = \mu_\pm(H) = g_n \mu_n \mp \frac{-m_F + \chi}{2\sqrt{1 - 2m_F\chi + \chi^2}} \mu_B \left(g_j - \frac{g_n \mu_n}{\mu_B}\right)$$

$$\approx \pm \frac{-m_F + \chi}{\sqrt{1 - 2m_F\chi + \chi^2}} \mu_B. \tag{2.10}$$

---

[1] Originating from the electric dipole model for the magnetic moment. Electrical currents vanish, no oscillating electric fields in the near vicinity.

[2] In [20, page 217] the magnetic moment is defined as $\mu = +\frac{dE}{d|\mathbf{B}|}$. This is not consistent with the usual definition of energy and force for a magnetic dipole.
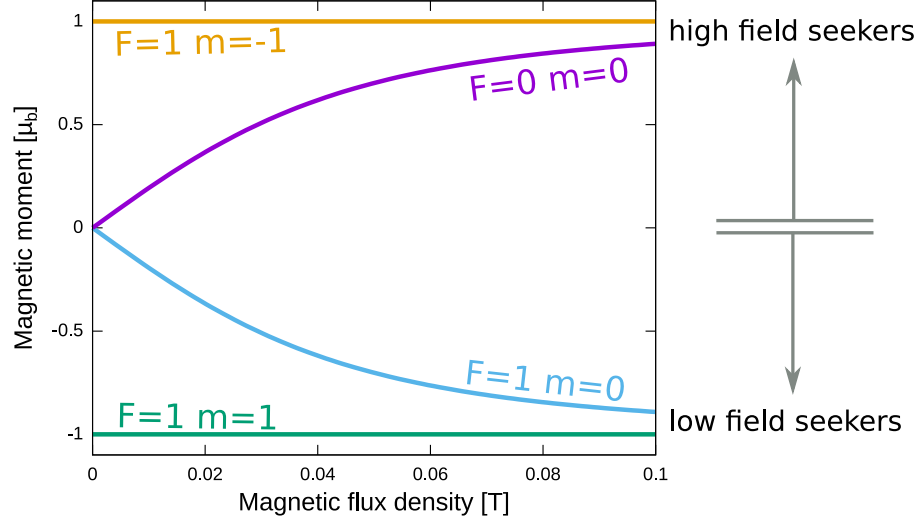
Figure 2.2.: Magnetic moment in units of μ_B of hydrogen in dependence of the magnetic field and quantum numbers F and m_F. States with a positive magnetic moment are low field seeking and states with a negative magnetic moment are high field seeking. In case of antihydrogen $F = 1\ m_F = 1$ is a HFS and $F = 1\ m_F = -1$ is a LFS.

and for antihydrogen the relation becomes

$$-\frac{\partial E_{\pm}(\bar{H})}{\partial |\mathbf{B}|} = \mu_{\pm}(\bar{H}) = g_n \mu_n \mp \frac{+m_F + \chi}{2\sqrt{1+2m_F\chi+\chi^2}}\mu_B\left(g_j - \frac{g_n\mu_n}{\mu_B}\right)$$
$$\approx \pm\frac{+m_F + \chi}{\sqrt{1+2m_F\chi+\chi^2}}\mu_B. \tag{2.11}$$

Calculating the magnetic moment in equation (2.10) and (2.11) allows the states to be classified by their movement in a magnetic field gradient. States that align their magnetic moments with an external magnetic field have a lower energy in higher fields ($\mu > 0$). States that follow gradients towards stronger fields are called high field seekers (HFS). Consequently, if the atoms follow a gradient towards lower magnetic fields ($\mu < 0$) they are called low field seekers (LFS). This dependence of the magnetic moment can be used for spin state selection in a Stern-Gerlach type apparatus like the ASACUSA superconducting sextupole magnet in section 3.3.

3. Beamline and experimental setup

Creating antihydrogen requires careful preparation, a well equipped laboratory, and high energetic particles to produce antimatter. This chapter focuses on the required preparation and the machines involved. Furthermore, creating antimatter and antihydrogen is not sufficient to do spectroscopy. A full beamline for atomic spectroscopy is required. In the following sections I will describe at first the required CERN facilities namely the accelerator chain. After acceleration, antiproton production and deceleration, the particles are handed over to the ASACUSA beamline for the experiments for the production of antihydrogen in the ASACUSA particle traps. After producing antihydrogen the now neutral anti atoms escape the production trap and form a beam that traverses the spectroscopy setup and finally annihilates in the antihydrogen detector (chapter 5).

3.1. The CERN accelerator chain

The very beginning of the accelerator chain is the LINAC 2, a linear accelerator that is used to produce a bunched beam of protons with an energy of 50 MeV [27]. The protons are then injected into the Proton Synchrotron Booster (PSB). The PSB is a synchrotron ring accelerator with four superimposed rings and a circumference of 157 m. The final particle energy when injecting into the Proton Synchrotron (PS) is 1.4 GeV [27]. The PS is also a synchrotron with a circumference of 628 m. It further accelerates the protons up to 28 GeV and every 100-120 s a bunch gets ejected into the AD target area.

The PS proton beam is extracted onto a 60 mm length Iridium rod to produce antiprotons. A magnetic horn extracts the antiprotons at a momentum of 3.5 GeV/c and focuses them to the AD. The Antiproton Decelerator is a storage ring with a circumference of 188 m. The initial particle momentum of 3.5 GeV/c gets reduced in three deceleration steps down to 100 MeV/c. During deceleration the beam emittance increases. As countermeasures
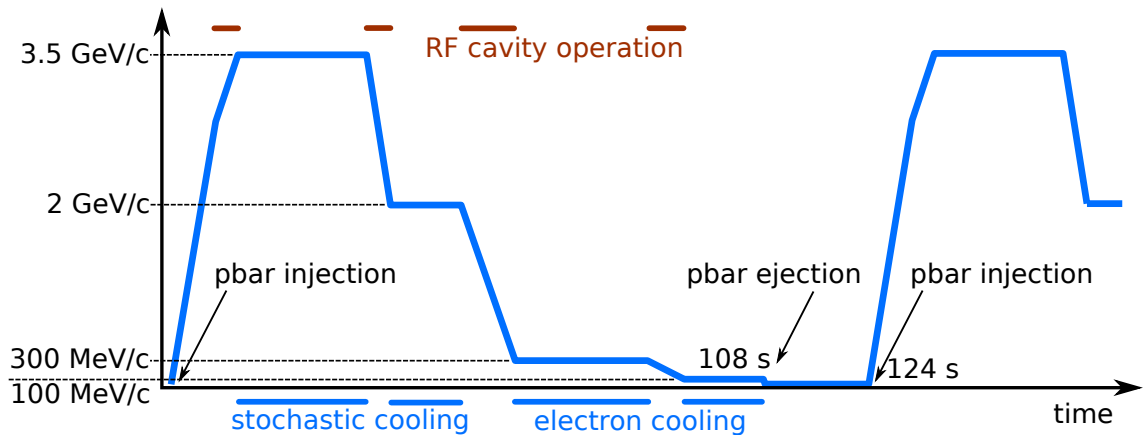
Figure 3.1.: Antiproton Decelerator cycle. The blue curve resembles the ramping of the magnets, the horizontal blue lines indicate the cooling steps and the lines on top show the activity of the "reverse" RF cavities.

stochastic cooling is implemented for higher energies and electron cooling for lower energies. The total AD cycle length was 108 s in 2015 with a repetition time of ≈124 seconds. For deceleration purposes the RF cavities operate in a "reverse" mode, meaning they decelerate the antiprotons instead of accelerating them. After the full deceleration cycle the antiproton bunch is extracted to the experimental areas. An overview graph for the deceleration cycle is drawn in Figure 3.1.

3.2. Antihydrogen beamline

In Figure 3.2 a technical overview drawing for the full ASACUSA apparatus including the antihydrogen and the spectroscopy beamline is shown. This section describes the beamline required for antihydrogen production: a positron source and accumulator, an antiproton accumulator (MUSASHI), and a double cusp trap for antihydrogen formation. The spectroscopy beamline (featuring a field ioniser, a microwave cavity, a superconducting sextupole magnet and a detector) will be discussed in section 3.3 .

An antiproton beam momentum of 100 MeV/c is too high for efficient trapping. Therefore, the ASACUSA collaboration uses the Radio Frequency Quadrupole Decelerator (RFQD) [27, 29] for further deceleration of the beam down to energies between 10 and 120 keV. The
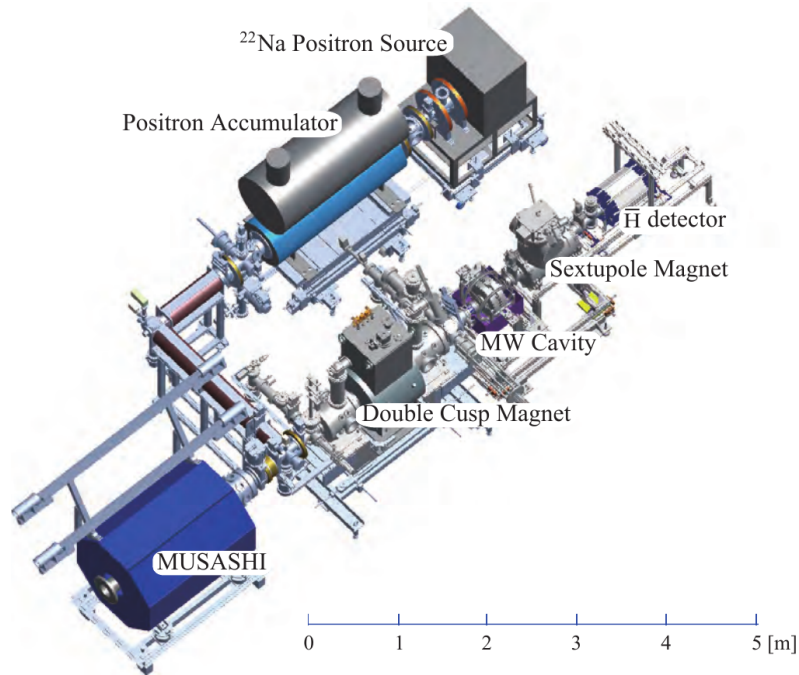
Figure 3.2.: Technical drawing of the ASACUSA apparatus for antihydrogen production and ground state hyperfine measurement. Labelled are the ^{22}Na source with the positron accumulator, the MUSASHI antiproton accumulator, the double cusp for antihydrogen production, and the components of the spectroscopy beamline, the microwave cavity, the superconducting sextupole magnet, and the antihydrogen detector. The graph is taken from [28].

slowed down beam passes a degrader foil at the entrance of the antiproton accumulator – the Monoenergetic Ultra Slow Antiproton Source for High-precision Investigations (MUSASHI) trap.

The MUSASHI trap [30] is a Penning type catching trap which is equipped with multi-ring electrodes for rotating wall compression and electron cooling. Inside of the trap the antiprotons are cooled and compressed and afterwards extracted with a selectable voltage to the cusp or double cusp mixing trap.

In addition to antiprotons, positrons are also requires for the production of antihydrogen. The ASACUSA collaboration produces positrons with a colliminated ^{22}Na source. The high energy positrons from the β^+ decay (≈ 0.2 MeV) are cooled using a solid neon
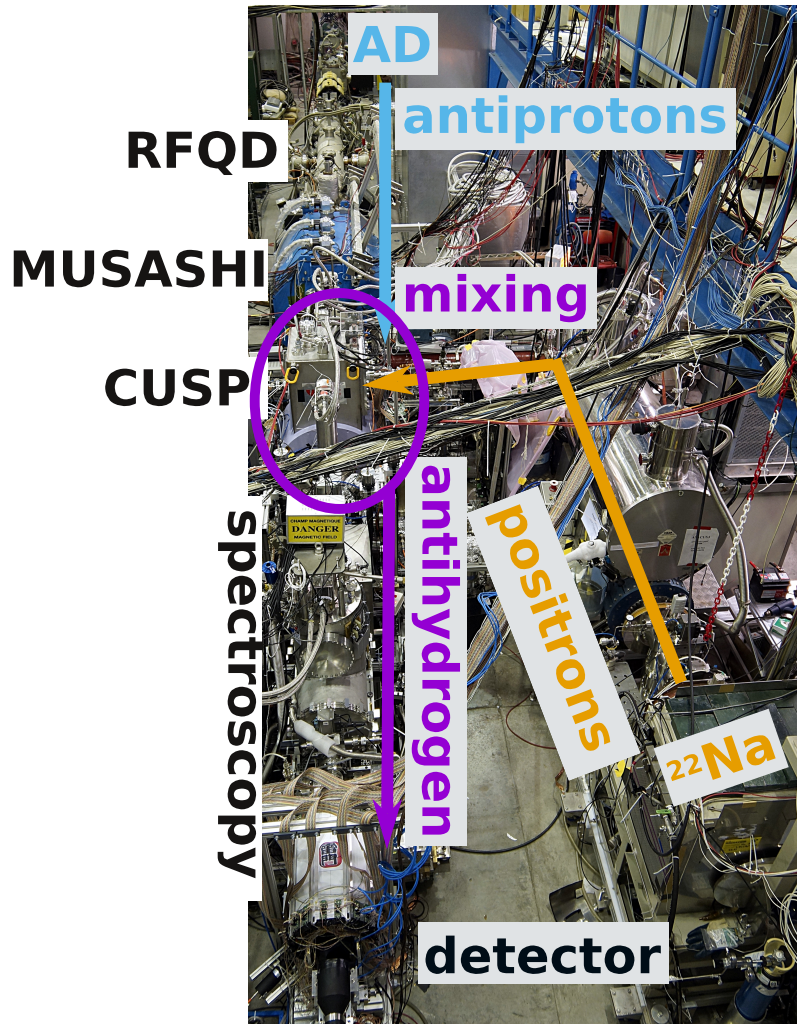
Figure 3.3.: Overview of the ASACUSA experimental area. In orange: ^{22}Na source with positron accumulator. Blue: Antiprotons from the AD, travelling through the RFQD, undergoing preparation in the MUSASHI trap. Violet: Mixing process in the cusp trap and antihydrogen traversing the spectroscopy apparatus with the detector (chapter 5) at the end.

moderator to ≈ 2 eV and afterwards further cooled (≈ 25 meV) and prepared for trapping in a N_2 buffer gas Penning trap [31]. After cooling, the positrons are compressed and extracted to the cusp / double cusp mixing trap.

The process of finally combining antiprotons and positrons to antihydrogen is a very difficult process that involves precisely manipulating the trapped particles. The cusp / double cusp trap consists of multi-ring electrodes for particle manipulation and trapping and a set of anti-Helmholtz coils. Prior to 2014 a cusp trap (equipped with a pair of anti-Helmholz coils) was used. This magnet produces a very strong magnetic gradient for focusing the neutral antihydrogen atoms towards the spectroscopy apparatus [32] by using the induced magnetic moment of the hyperfine states in antihydrogen (compare equation (2.11) and Figure 2.2). The trap magnet was upgraded in 2014 with a so-called "double-cusp" magnet featuring a pair of two anti-Helmholz coils in order to increase the field gradients for focusing and polarisation while reducing the residual field at the position of the microwave cavity. A symbolic representation of the double cusp field lines is shown in Figure 3.4. The mixing process itself occurs near the entry point of the magnet system in a region with homogeneous magnetic field. This is necessary for operating a Penning style particle trap with a nested well potential. By gently injecting the antiproton plasma into the positron plasma cold antihydrogen is formed by a three-body recombination process [33–36]. After recombination to antihydrogen the now neutral anti atom escapes the trap. The whole beamline is shown in Figure 3.3.

3.3. Spectroscopy beamline

The spectroscopy apparatus consists of a microwave cavity, a superconducting sextupole magnet and an antihydrogen detector. In the microwave cavity ground-state hyperfine transitions are driven and the magnet operates as a spin-state selector. Together these building blocks are constituents of a Rabi like experimental setup [19, 37, 38] to measure the ground-state hyperfine splitting of antihydrogen (compare Figure 1.1). In Figure 3.4 the spectroscopy beamline is shown as a rendering from CAD drawings and a schematic sketch.

As described above, the cold and neutral antihydrogen atoms can leave the trapping region. Depending on their spin state they are either focused by the inhomogeneous double cusp field onto the cavity entrance, or defocused. In the latter case the anti

double cusp | cavity | sextupole | detector
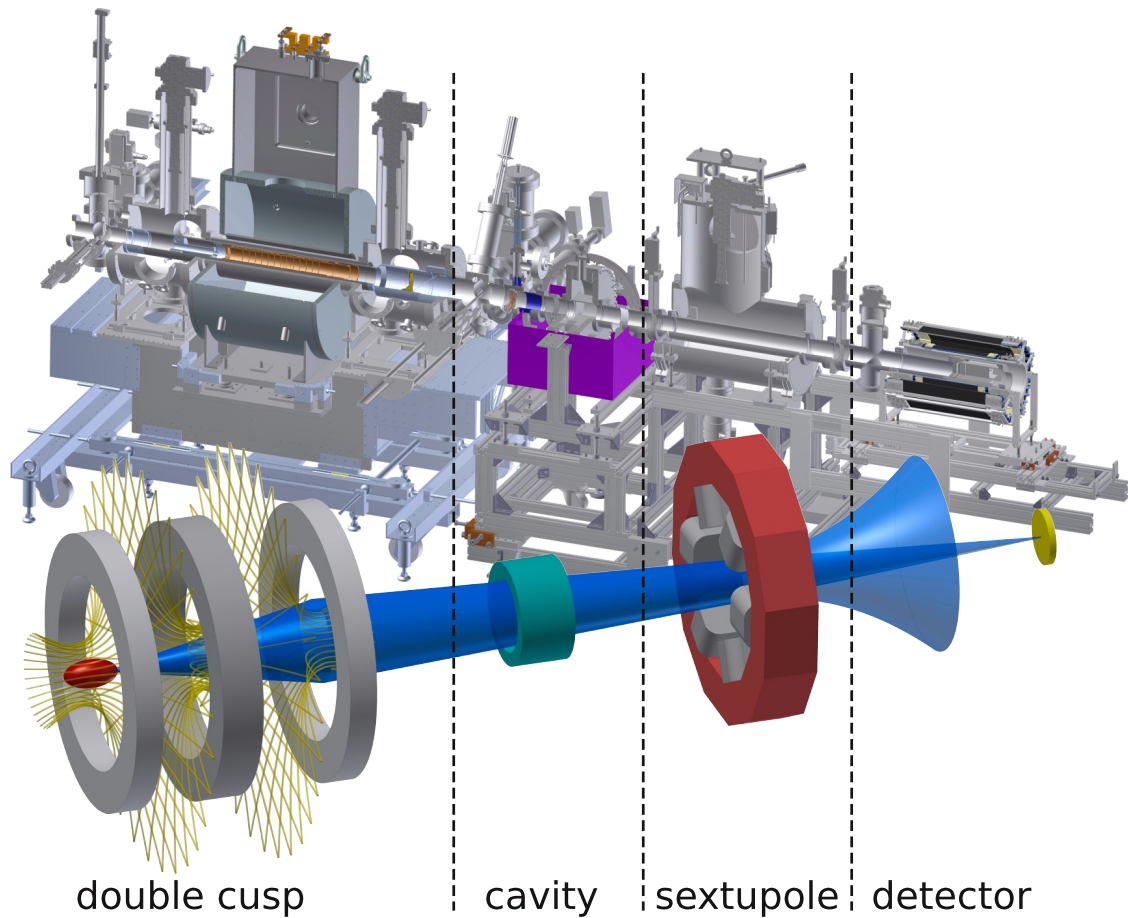
Figure 3.4.: Spectroscopy beamline with double cusp production trap. The top graph shows a rendering of the beamline CAD drawing with the double cusp on the left, the microwave cavity including the Mu-metal shielding (purple) in the centre. The superconducting sextupole magnet and the antihydrogen detector. The bottom graph is a schematic view of the spectroscopy apparatus. The red region on the left is the antihydrogen production (mixing) region. Followed by the double cusp field (yellow). The low-field seeking antihydrogen atoms traverse the microwave cavity and the sextupole magnet. In case the atoms undergo a spin flip in the cavity they are defocused and annihilate on the beam pipe wall. Without a spin flip the atoms are focused onto the detector. Both graphs were produced by Doris Pristauz-Telsnigg.

atoms annihilate on the walls. By this mechanism a cold and spin polarised beam of antihydrogen is created [33]. After the double cusp apparatus a field ioniser chamber is mounted. This chamber serves two purposes: it creates a strong and tunable electrostatic field for measuring the primary quantum number (n) distribution of antihydrogen by ionising quantum states down to $n \geq 12$, and at the same time the electrostatic field reflects antiprotons that have escaped the trap. The same vacuum chamber houses a movable active beam blocker. Together with plastic scintillator panels mounted outside of the field ioniser chamber, the active beam blocker serves as a beam normalisation counter. A fraction of the antihydrogen atoms in the beam annihilate on the active surface and the annihilation pions are detected in coincidence by the outside plastic scintillators. This way the antihydrogen flux can be monitored and corrected during a microwave resonance scan.

The microwave spin flip cavity is a strip-line cavity operating at a wavelength of 21 cm (1.42 GHz) [39]. To produce resonance scans the cavity has a low quality factor (≈ 200). This allows detuning in a broad range covering the σ_1 and the π_1 resonances using the same device. Depending on the detune the spin-flip conditions are met and the low-field seeking states flip into high-field seeking states. The beam with a mixture of spin states propagates towards the sextupole magnet. This type of magnet is characterised by its strong radial field gradients. Similar to a Stern-Gerlach apparatus the magnet operates as an energy and spin-state dependent lens, focusing low-field seeking states onto the detector and defocusing high-field seeking states. By using this spin state selection a dip in the normalised count rate can be observed if the resonance condition is met. Due to the properties of the strip line cavity the line shape does not follow the simple shape as it is described in Kellogg, Rabi and Zacharias [19]. A detailed discussion of the line shape follows in chapter 4.

4. Simulations and numerical calculations

This chapter touches two distinct topics, first Monte-Carlo simulations of the full beamline geometry including trap fields, magnets and hyperfine transitions using the Geant4 toolkit [40, 41]. Secondly, numerical calculations of the hyperfine transitions in the stripline microwave cavity will be discussed.

In the case of the Geant4 simulations, the following section will focus on parts of the code that were developed or improved during this thesis. In addition some results are discussed. All other parts of the simulation will be briefly mentioned without an in-depth discussion. The numerical calculations section focuses on describing microwave transitions in the cavity. Due to the cosine distribution of the microwave field inside the cavity volume a non-trivial line shape arises. This line shape and its effects on measuring the ground-state hyperfine structure of hydrogen and antihydrogen are discussed.

4.1. Geant 4 beamline simulation

Simulating a low energy atom beamline is a challenging task in Geant4. In a collaborative effort, a simulation program that combines simulation of the beamline geometry, the magnetic and electric field in the trap and magnets, the microwave transition between hyperfine states, and the annihilation in the detector was developed. The first version of this code was developed by Bertalan Juhasz.

In the following three subsections the basic idea of how to implement tracking of neutral atoms into Geant4 is discussed. This is followed by a short introduction on antiproton

annihilation codes. Finally, results for the polarisation of ground state antihydrogen after traversing a cusp or double cusp field will be presented.

At this point, it should be noted that none of the simulation results for the detector are included in this section. Simulations for detector multiplicities and angular distributions are shown and compared with measured data in section 6.3.

4.1.1. Beamline, geometry and tracking

Up to Geant4 version 10 the magnetic field dependent tracking of neutral particles was completely ignored. Implementing tracking of antihydrogen required a modification of the Geant4 library code. Thankfully, since version 10 neutral particle tracking in magnetic fields is possible with some limitations that can be overcome. The new possibilities for neural particle tracking were introduced by the Geant4 core developers after the ASACUSA tracking code was presented to them.

Hydrogen and antihydrogen are not elementary particles, they are atoms with an inherent inner structure. In the presence of external field this inner structure leads to magnetic and electric dipole moments due to Zeemann and Stark effects and of course, due to the hyperfine splitting. In the present situation the simulation code focuses on magnetic effects. The experimental setup only utilises electric fields in the field ioniser chamber and in the production trap. The Zeemann effect, more precisely the complete Paschen-Back effect [20, chapter 46], induces a magnetic dipole moment. For tracking atoms with this field dependent magnetic moment (μ) a modified equation of motion is required:

$$\mathbf{F} = q\left[\mathbf{E} + (\mathbf{v} \times \mathbf{B})\right] + \nabla(\mathbf{\mu B}) \tag{4.1}$$

Higher states of Hydrogen and antihydrogen can also produce a non-vanishing magnetic moment. The simulation of deexcitation processes and higher quantum states is covered in Lundmark et al. [42]. The implementation of the Stark-Effect is an ongoing effort. In the following only ground state atoms will be considered.

In Figure 4.1 the simulated geometry for antihydrogen is shown, on the right side the cusp or double cusp trap acts as a particle source with a Gaussian production region (full width at half maximum (FWHM) 1 mm) that is located 1.75 m upstream since 2014 and 1.65 m
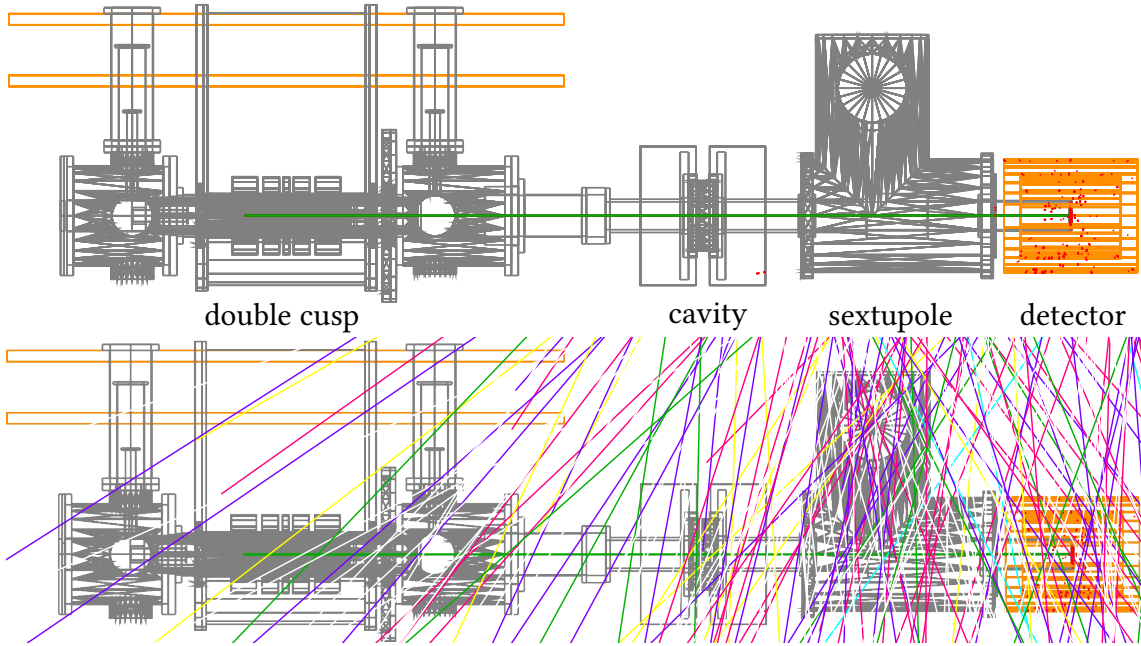
Figure 4.1.: **Top**: simulated beamline geometry with double cusp including magnetic and electric fields, microwave cavity, sextupole magnet and annihilation detector. A narrow beam of antihydrogen was simulated for the graph (green), the hit positions of the annihilation pions are visible in the detector (red). **Bottom**: simulated beamline geometry with CRY simulation. Colour coded are neutrons (green), electrons (yellow), muons (dark and light violet), and positrons (cyan)

upstream prior to 2014 with respect to the microwave cavity centre. The simulated atoms traverse the cavity, pass through the sextupole magnet, and finally annihilate on the central detector. The annihilation pions are then detected by the surrounding two-layered hodoscope. The Hamilton operator for the hyperfine transition (equation (2.1)) is solved using an adaptive step Runge-Kutta solver on a step by step basis in the simulation. In Figure 4.2 an example for a simulated microwave scan for both the σ_1 and the π_1 transition is shown. A detailed description of the microwave cavity implementation and simulation performance can be found in the master's thesis of Bernadette Kolbinger [43] and in Kolbinger et al. [44].

For simulating background, the CRY library [45] is used with an emitting surface of 3×3 mm^2 placed 30 cm above the detector centre. The magnetic field inside of the
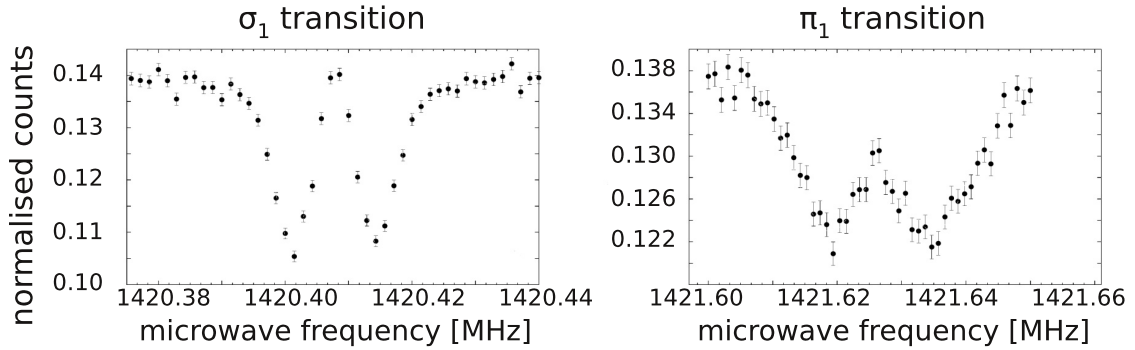
Figure 4.2.: Simulation of a resonance scan for the σ_1 (**left**) and π_1 (**right**) transition with a measured static magnetic field map with a mean of 88 µT and a FWHM of 1.6 µT was used. The simulation was done with a polarisation of 70% LFS and a beam temperature of 50 K. (graph is modified, original from the master's thesis of Bernadette Kolbinger [43])

sextupole magnet is calculated using the analytic solution for an ideal sextupole magnet. The commonly known general solution for multipole magnets can be easily derived from Maxwell's equations. When selecting z as beam direction and with n being the pole number and C_n representing the total B field strength the multipole equation is:

$$B_y + iB_x - C_n(x + iy)^{n-1} = 0. \tag{4.2}$$

In addition, the simulation can also use measured or calculated field maps for the cusp and double cusp field and for the static field inside of the microwave cavity.

4.1.2. Antiproton annihilation

Low energetic antiprotons annihilating on target nuclei are problematic in Geant4. The available models do not reproduce the available data if one is comparing the multiplicities from the different decay channels (Table 4.1). To compensate this, a simple phenomenological decay model was originally developed by Bertalan Juhasz. Various improvements for the generalisation to heavier nuclei were introduced in this thesis. It should be noted that this model is tailored to reproduce experimental multiplicities from low energetic antiprotons. This model completely ignores secondary effects in the target nucleus like recoil effects and further hadronic interactions. Simulations that are required to produce valid energy deposits in the primary annihilation material should use the Geant4

Table 4.1.: Comparison of some antiproton annihilation channels in different Geant4 models and with experimental data. [†]model discontinued in Geant4 10. [‡]described in this work. Simulations for the comparison were carried out by Bálint Radic. The experimental data are taken from [46].

Channel	QGSP_BERT_CHIPS[†]	CHIPS[†]	FTFP_BERT	SMI Code[‡]	Exp. data
$1\pi_+, 1\pi_-, 3\pi_0$	5.3%	4.6%	5.5%	23.6%	23.3%
$2\pi_+, 2\pi_-, 1\pi_0$	11.9%	11.2%	12.1%	19.9%	19.6%
$1K_+, 1K_-, 1K_0$	0.0%	0.0%	0.0%	0.231%	0.237%
$1K_+, 1K_-, 1\pi_0$	0.167%	0.4%	0.182%	0.239%	0.237%

FTFP_BERT_TRV model. All simulations in section 6.3 were performed using the SMI annihilation code which outputs the measured experimental multiplicities.

In general, the model uses a table of measured branching ratios for $\overline{p}p$ and $\overline{p}n$ reactions [46]. Afterwards, the target material is used to determine the antiproton capture probability for the constituent nuclei (scales with $Z^{\frac{2}{3}}$ [47]) and to select a target nucleus. Depending on the target nucleus, its charge, nucleon number, and the target nucleon (Proton or Neutron) is selected according to [48, 49]. Finally, the annihilation products are created and the initial pion energy is modified to incorporate energy loss mechanisms due to inelastic scattering with a quasi-free scattering model in the production nucleus [50–53].

4.1.3. Antihydrogen spin polarisation

The cusp field can act as an optical lens for low-field seeking antihydrogen [32] in the ground state. However, this simple approach neglects a variety of geometric effects, therefore a full beamline simulation was performed to estimate the spin polarisation under certain initial conditions and temperature distributions. In Figure 4.3 the spin polarisation at the microwave cavity entry is shown colour coded as a function of the initial polarisation during production on the abscissa and the particle temperature on the ordinate.

For each polarisation setting 10^5 atoms were simulated with a flat velocity distribution between 0 and 4000 m/s. The source (Gaussian shape with FWHM 1 mm, emittance angle 30°) was placed at the position of the mixing region in the cusp (-1.65 m) and

double cusp field (-1.75 m), emitting particles in a cone with direction downstream and an opening angle of 30°. A dummy detector to record the number of anti atoms with their hyperfine state was placed at the entry of the microwave cavity (-0.05 m). All positions are given with respect to the centre of the cavity. The maps for the cusp and double cusp fields were produced by Simon van Gorp with a software package named COMSOL[1]. In a post processing step the resulting joint velocity-polarisation distribution was weighted with a Maxwell-Boltzmann distribution to produce a joint temperature-polarisation map. Non-adiabatic processes that could lead to spin-flips have been neglected in these simulations.

When comparing the results (shown in Figure 4.3) for cusp and double cusp field it can be seen that the polarisation strength is better for the double cusp field. Higher temperatures with lower initial LFS fraction are acceptable with the double cusp providing an overall higher spin polarisation. The cusp field provides for an unpolarised beam in ground state (50% LFS) and a temperature of 100 K a polarisation of ≈60% LFS while a double cusp field produces ≈70% LFS.

4.2. Numerical calculation of microwave transitions

The line shape produced by the stripline geometry of the microwave cavity is characterised by two peaks around the ideal resonance frequency of the hyperfine transition. To study this effect and its impact on the analysis of measurements, numerical studies were performed.

In the case of small uniformly distributed oscillating magnetic field on top of a stronger uniform magnetic field, the time evolution of the state population density[2] of any atomic two level system can be described analytically by Rabi oscillations

$$p(t) = \frac{\Omega^2}{\Omega'^2} \cos^2\left(\frac{\Omega' t}{2}\right). \tag{4.3}$$

The frequency of the oscillation, the so called generalised Rabi frequency (Ω'), depends on the Rabi frequency (Ω) and a detuning (Δ). The gyromagnetic factor of the electron

---

[1]A proprietary software by COMSOL Inc. (www.comsol.com)
[2]The same relation holds for the probability of occupancy.
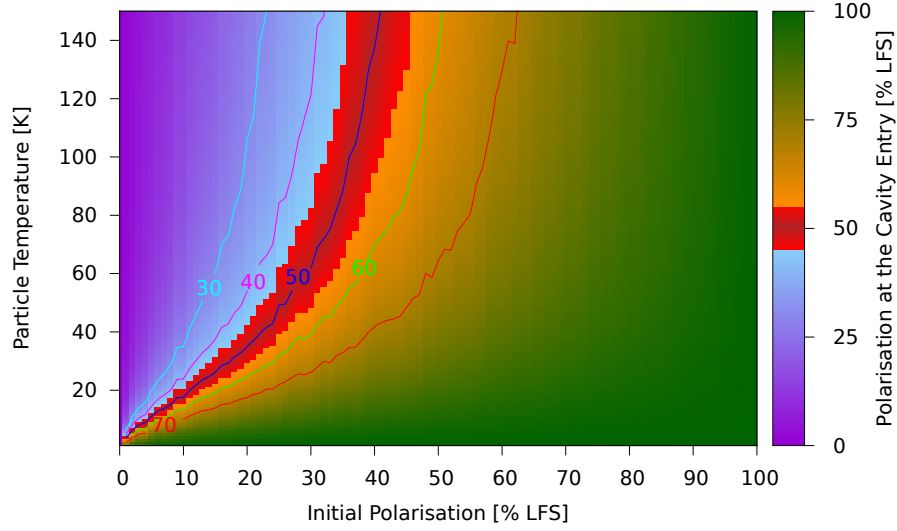
(a) single cusp field
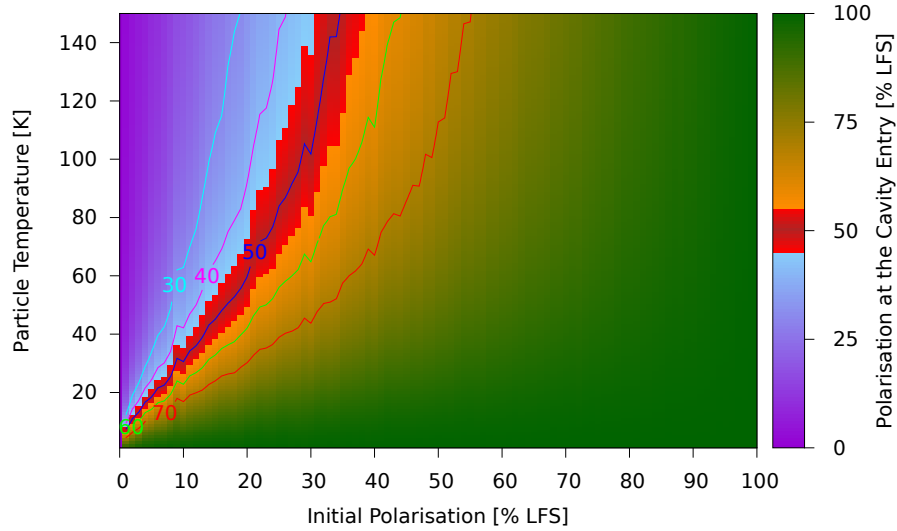
(b) double cusp field

Figure 4.3.: Spin polarisation of the antihydrogen beam at the microwave cavity entry in dependence of temperature and initial polarisation during production. Purple-blue favours high-field seeking states, orange-green favours low-field seeking states, the red band indicated a region between 45-55 % LFS. **a**: resulting polarisation after traversing a single cusp field. **b**: polarisation after passing through a double cusp field. The double cusp field creates a low-field seeking beam even for higher temperatures and lower initial polarisations.

or positron (γ), and the absolute value of the rotating or oscillating magnetic field amplitude ($|\mathbf{B}|$) are required for the computation of the Rabi frequency. The generalised Rabi frequency then becomes

$$\Omega^{'} = \sqrt{\Omega^2 + \Delta^2} \tag{4.4}$$

with the Rabi frequency in rotating wave approximation being

$$\Omega = \gamma|\mathbf{B}|. \tag{4.5}$$

In the case of an oscillating magnetic field, the Rabi frequency can be calculated as

$$\Omega = \frac{\gamma|\mathbf{B}|}{2}. \tag{4.6}$$

The ground state hyperfine states in hydrogen and antihydrogen form a four level system (chapter 2). In combination with the non-uniformly distributed oscillating magnetic field in the stripline cavity, the time evolution of the state population densities has to be calculated numerically. The transition between ground state hyperfine states in hydrogen and antihydrogen is calculated by solving the Von Neumann Equation

$$\frac{\partial\hat{\rho}}{\partial t} = \frac{i}{\hbar}\left[\hat{H}_i, \hat{\rho}\right] \tag{4.7}$$

with the interaction Hamilton operator ($\mathcal{H}$) in equation (2.1) in density matrix (ρ) formalism. This gives a set of 16 coupled differential equations describing the state density development over time. Those equations can be expressed in terms of Rabi frequencies for the individual states as optical Bloch equations. The Rabi frequencies become a 4×4 matrix, where only the off-diagonal elements contribute to the Von Neumann Equation. The Rabi frequencies contain not only the gyromagnetic factor, but also the Clebsch-Gorden coefficients for the transitions.

By using the fact that ρ is hermitian, the problem can be reduced to 10 independent equations which are solvable using the ZVODE algorithm [54, 55]. The implementation was done in python by using the numpy and scipy packages [56, 57].

In Figure 4.4 a full calculation of the state density development is shown. The horizontal axis shows the frequency detune in units of the Rabi frequency (compare equation (4.4)) for the maximum microwave amplitude in the cavity and the vertical axis represents the length of the microwave cavity in beam direction. Colour coding of the state population

density for a given transition and a fixed combination of particle velocity and microwave power is displayed. Power and velocity were chosen to produce a full state conversion. The red graph on top contains the final line shape after undergoing a full conversion in the stripline cavity. The graph on the left side shows the distribution of the absolute amplitude of the oscillating field along the beam axis of the cavity.

From Figure 4.4 it can be immediately seen that if the detune is zero, meaning the cavity is tuned to the resonance frequency of the transition, no change of the final state will happen. Tracing the state development back to the cavity centre reveals that the transition of the particle ensemble was driven to 50%. Due to a change of sign in the B-Field distribution this process is reversed and the ensemble returns to its initial distribution. Repeating this argument for different cavity settings allows to conclude that: Under all conditions, if the cavity is tuned to a resonance, the initial state will be preserved.

It follows that a full transition is only possible if the cavity is detuned. As mentioned before the Von Neumann Equation for the ground state hyperfine transitions can be expressed in terms of Rabi and transition frequencies. Since the line shape stays constant in those units (similar to the simple case in equation (4.4)), the width and separation of the peaks is dependent on the time a particle spends in the cavity (proportional to the velocity of the atom) and the external magnetic field.

On one hand, this fact impacts the measurement of the transition frequency as sidebands are washed out by broad velocity distributions in the atomic beam. On the other hand, this dependence on external factors can be used to characterise the microwave cavity and its static magnetic field when performing measurements. The ASACUSA spectroscopy apparatus was tested and characterised using a cold spin polarised beam of hydrogen [58–60]. For the data analysis of the hydrogen beam experiment a set of numerical calculations for the state population density in dependence of the absolute microwave frequency and the microwave amplitude/power were used. In Figure 4.5 one of the calculated microwave power scans is shown. The calculation was done for a fixed beam velocity of 1000 m/s and a static magnetic field of 44 µT. It can be seen that on the resonance frequency the transition probability is always zero and that the distance of the peaks increases with higher microwave amplitude.

In the PhD thesis of Martin Diermaier [58], the calculated frequency-power scan is compared with actual measurements showing good agreement. For analysing measured line shapes, frequency-power scans were calculated for different particle velocities, and the static magnetic field in the experiment. By using spline interpolation and superposition of
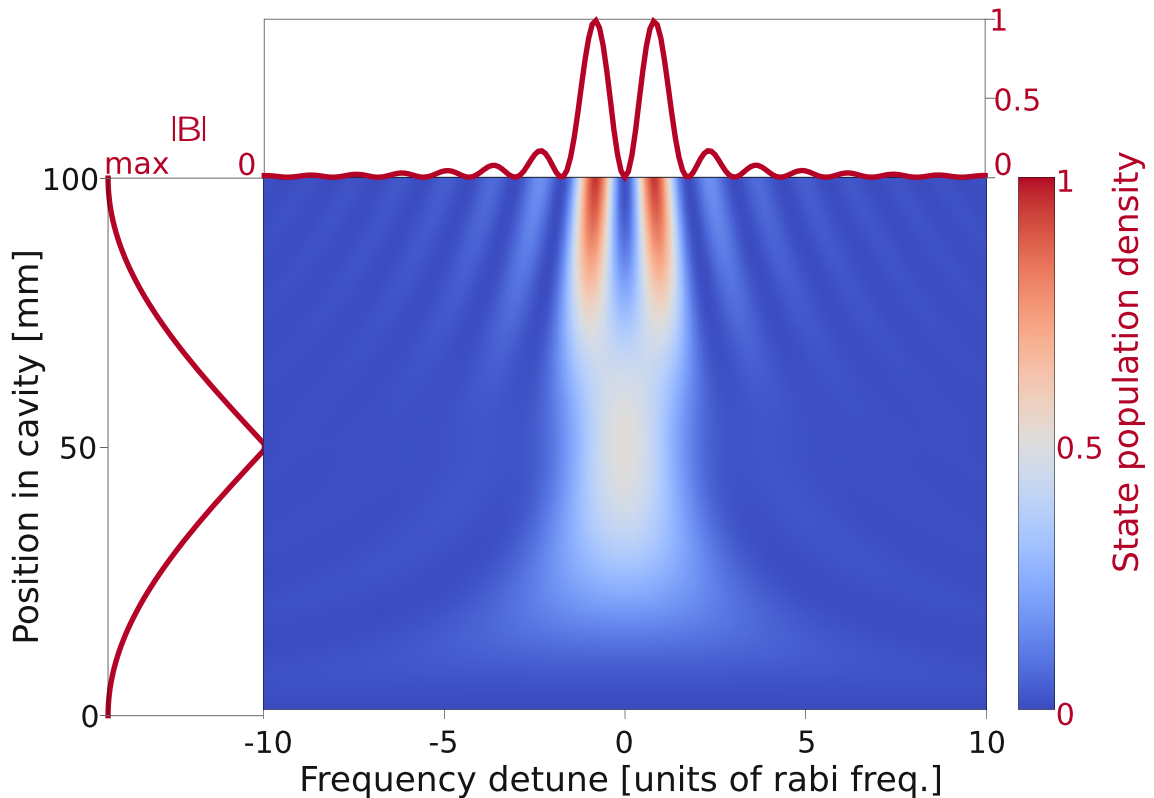
Figure 4.4.: Development of the state population density for an ensemble of spin polarised anti-/hydrogen atoms inside of the stripline microwave cavity depending on the cavity detune in units of the Rabi frequency for the maximum microwave amplitude. On the left side the distribution of the absolute microwave B field (cosine distributed) is plotted along the cavity length. On top the resulting line shape is shown. The double peak structure arises from the oscillating field distribution driving the states to 50 % and then back due to the change of sign in the B field if the detune is zero.

calculated line shapes for different velocities the resulting shapes for velocity distributions can be modelled [61].
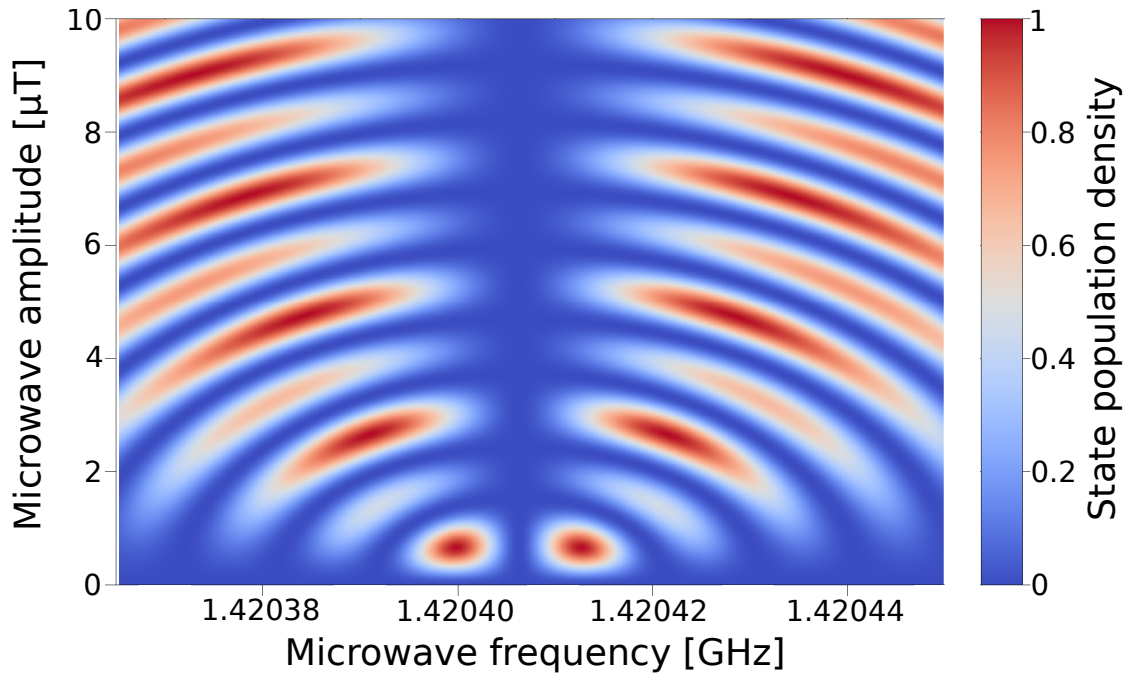
Figure 4.5.: State population density for an ensemble of spin polarised atoms in dependence of microwave frequency and microwave power/amplitude. The displayed calculation was done for an ensemble of fully spin polarised atoms with a fixed beam velocity of 1000 m/s and a static magnetic field of 44 μT. For all microwave powers the transition probability is zero if the exact resonance frequency of the transition is selected due to the stripline cavity effect.

5. Antihydrogen Detector

A detector for in-beam measurements of the ground state hyperfine structure of anti-hydrogen needs to fulfil two independent tasks. First it has to be able to discriminate between spin states of the incident anti atoms. This means it should only detect those particles that actually reach the very end of the beamline and ignore those who annihilate at the beampipe walls due to defocusing. On the other hand, the same detector is required for beam diagnosis and tuning of the $\overline{\text{H}}$ production. It follows that the detector needs a big solid angle acceptance and at the same time the ability to detect even very low signal rates within high background.

In section 5.1 I will discuss the basic ideas and concepts of the detector design, including all properties like material choice, geometric structure and active elements. Afterwards, section 5.2 will feature an in-depth description and evaluation of the detector electronics, namely the intelligent front-end electronics for silicon photo detectors (IFES) boards that were developed during the course of this work [62]. The last two sections in this chapter will cover the design of the trigger (section 5.3) and the setup of the Maximum Integrated Data Acquisition System (MIDAS) based data acquisition (DAQ) system (section 5.4).

5.1. General concept

A summary of the detector material employed can be found in Table 5.1 for reference. This table summarises the scintillator material used and the electronic detector elements.

Table 5.1.: Active detector material

Type	Description	Size	Quantity
EJ-200	scintillator, inner hodoscope bars	$450{\times}35{\times}5$ mm^3	32
EJ-200	scintillator, outer hodoscope bars	$300{\times}20{\times}5$ mm^3	32
BGO	scintillator, central calorimeter	r=5 cm, width: 5 mm	1
H8500	MAPMT, central detector readout	$49{\times}49$ mm^2	4
PM3350TS	SiPM, hodoscope readout	$3{\times}3$ mm^2	256
BC-680	reflective paint, light guides	surface	n.a.

5.1.1. Central detector

The antihydrogen detector consists of an inner calorimeter with position sensitive readout. This part of the detector is a 10 cm diameter bismuth germanate (BGO) disc with 5 mm thickness. The disc is located inside of the beamline vacuum, with an air gap to a vacuum window. Coupled to the vacuum window with optical grease are four Hamamatsu H8500 multi-anode photo multiplier tubes (PMTs) with $8{\times}8$ pixels each. The readout is done using a ClearPulse CP80057 Versa Module Europa (VME) bus card and four CP80190 front-end modules, from the same vendor, that directly couple to the PMTs. This setup can resolve tracks and impact positions with a resolution of $16{\times}16$ pixel and at the same time accurately, measure the energy deposit [63]. The central calorimeter is supplied and developed by Yugo Nagata from the Atomic Physics Laboratory, RIKEN. As it was not developed as part of this work, I will only cover it to an extent that is necessary for the understanding of this thesis.

5.1.2. Hodoscope

The surrounding hodoscope is composed of two layers. Each layer consists of 32 scintillating bars. As scintillating material Eljen Technologys EJ-200 was chosen. This material is a good choice for long attenuation length, high light output and cost effectiveness (equivalent to St. Gobain BC-408). The inner hodoscope layer has an overall length equal to that of the scintillators, 300 mm with a cross section of $20{\times}5$ mm^2. A light guide on each side of the bar, with a length of 40 mm reduces the cross section surface to $8{\times}5$ mm^2. Two silicon photo multilpiers (SiPMs) connected in series detect the scintillation light

on each side of the bar. A detailed description of the assembly and construction of the hodoscope detector can be found in the master's thesis of Aaron Capon [64].

The bars of the outer hodoscope have a length of 450 mm and a cross section surface of 35×5 mm^2. Again, a light guide with length 75 mm reduces it down to 8×5 mm^2. The readout is identical to the inner hodoscope layer. Each bar is individually wrapped in aluminium foil with an air gap to provide reflectivity and suppression of crosstalk. During the beamtimes in 2014 and 2015, the light guides were painted with reflective paint of type BC-680. For the inner hodoscope four bars are wrapped together in light blocking foil. Triangular plastic pieces are added to support the light guides. The outer hodoscope bars are wrapped in bundles of two bars.

SiPMs of the type KETEK PM3350TS are used. They have a 3×3 mm active surface and a technology called optical trench separation (metal filled trenches between the individual avalanche photo diodes (APDs) on the chip). This technology is the main advantage of this type. It dramatically reduces the dark count rate ($\leq$300 kHz/mm^2) and the crosstalk (20%), which allows for use cases where precise timing is required. The geometric fill factor is 60%, resulting in a photon detection efficiency of $\geq$ 40% at the peak wavelength (420 nm).

Gluing the SiPMs on both side of the bars ensures dark noise suppression by requiring the coincidence between the upstream and downstream side. The distribution of the pulse height between both sides and their respective timing difference can be combined to provide a hit position along the bar to a limited extent. Figure 5.1 is an overview drawing of the installed detector on the beampipe.

The detector is a barrel with an octagonal shape. Each of the sides is a removable panel supporting four individual bars. For every panel there is defined colour code, mirrored between inner and outer layers (Figure 5.2). Additionally, each channel has a defined wire colour associated to it. This guarantees a quick wiring and ensures easy detection of any wiring errors (For a full table see section A.2). The most inner part of the hodoscope is a pipe of 1 mm thick aluminium to stabilise the structure. From Geant4 simulations it was determined that the scattering probability of pions from $\overline{p}$ annihilations can be neglected. The total length of the outer hodoscope is 606 mm and the whole structure is mounted on a movable cart.

The rails on the Bosch-profile table allow for complete retraction of the detector for both mounting and dismounting, as well as easier access in case of malfunction. Reproducibility
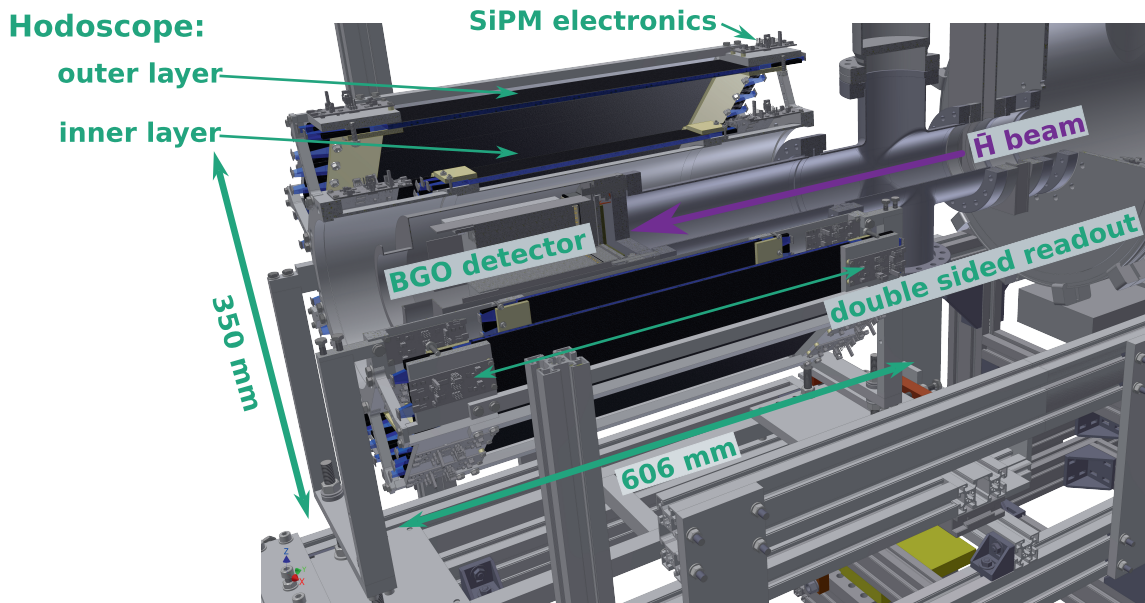
Figure 5.1.: A schematic view of the detector arrangement. The antihydrogen beam originates from the right and hits the BGO calorimeter in the centre. On the hodoscopes the positions of the IFES modules (section 5.2) are visible. CAD rendering by Doris Pristauz-Telsnigg.

of the final position is ensured with four metal plates that can be screwed to the structure. The plates upstream define the position for productive operation and the downstream plates prevent an accidental moving of the detector. The detector is mounted with four adjustable screws on a stable metal plate which by itself is mounted on plastic gliders with adjustment screws for fine positioning.

5.1.3. Electronics and cabling

In the following section I will use the term *front-end electronics* for all electronics placed in direct vicinity of the beam or inside of the experimental area. All other electronics are placed outside and are accessible during operation. In Figure 5.3 the front-end electronics are shown in the upper half of the flow chart marked with the word "beam area".

In Figure 5.3 a colour scheme for easy identification of signal types is employed. Red signals correspond to digital signals, this can be either a signal following the nuclear
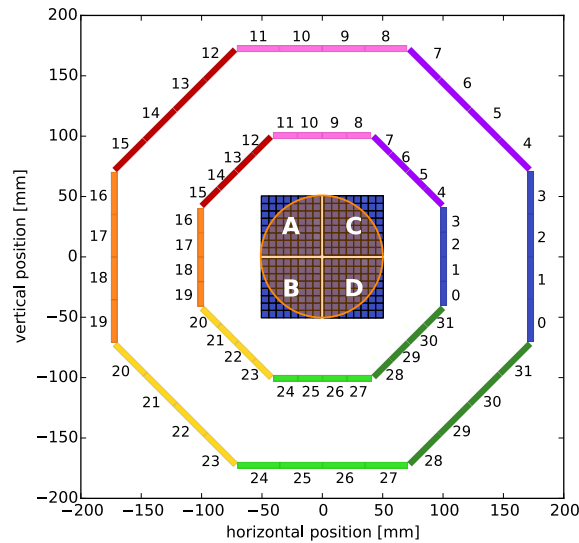
Figure 5.2.: This diagram shows a cut through the detector, with the hodoscope bars are marked with their corresponding panel colour and number. In the centre the BGO crystal is drawn in orange and the multi anode PMTs are blue. The white letters mark the readout port of the Clearpulse CP80057 VME module. The displayed view is from behind looking upstream.

instrumentation standard (NIM) standard, the low voltage differential signaling (LVDS) standard or in one case they are emitter coupled logic (ECL) signals. Analogue signals are encoded in blue, and control signals are displayed in green.

Front-end electronics

A special role, in terms of front-end electronics, is taken by the IFES boards that were developed during this thesis. A detailed discussion follows in the next section (5.2).

The hodoscope detector is read out via the 64 IFES modules. They are powered using standard low voltage laboratory power supplies in a chain. The slow control of the boards is handled by an Arduino[1] Yún single board micro controller, which accesses the boards via a daisy-chained bus connections (Figure 5.7). All digital trigger signals and all

---

[1]http://www.arduino.cc
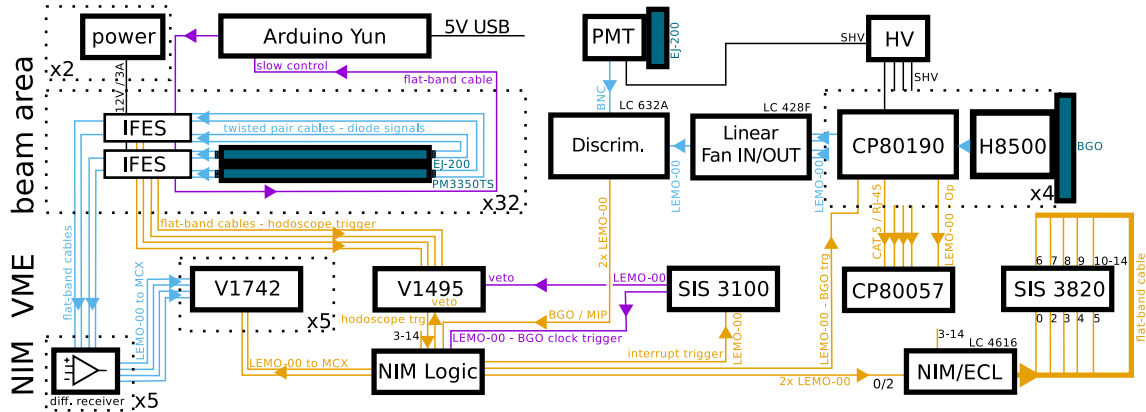
Figure 5.3.: Flow diagram of the electronics. Analogue signals are blue, digital signals are orange and control signals are violet. Power lines are drawn in black. The upper half of the graph contains electronics that are directly in the experimental area, the NIM and VME electronics are outside.

analogue signals are transferred out of the experimental area to NIM and VME modules. The generation of the trigger and its logic will be discussed in section 5.3.

The BGO calorimeter is read via four H8500 multi anode PMTs directly connected to the CP80190 front-end modules. Those devices contain 64 pulse shaping amplifiers with peak sensing analogue to digital converters (ADCs). The four dynode pulses from the H8500 are combined using a NIM linear fan-in. The combined signal is sent through a discriminator to provide a fast trigger signal from the BGO calorimeter ($\approx 50 - 100\,\mathrm{ns}$). After triggering, the CP80190 modules process the shaped pulses and produce a 12 bit energy signal for every of the 256 calorimeter channels. The data are transported out of the beam area by four Ethernet cables.

For energy calibration an additional scintillator is placed downstream of the BGO calorimeter. This detector is a 10 cm diameter EJ-200 disc that is read using a PMT. The analogue signal is discriminated and the resulting pulse is sent to the readout electronics.

Readout electronics

Accelerator facilities are notorious for being electronically noisy areas due to the high currents and voltages applied during operation. To reduce the impact of this hostile environment on the data, all analogue signals use balanced differential transmission. This way pickup noise is removed when passing the differential to single-ended converter outside of the beam area. The single-ended signal is directly fed to a CAEN VME waveform digitisers of type V1742.

The V1742 modules are 5 GS/s ADCs based on the Digital Ring Sampler 4 (DRS4) [65] chip from the Paul Scherrer Institut in Switzerland. On arrival of a trigger signal the analogue ring sampler is frozen and each individual storage cell is digitised using an ADC. To get accurate timing we operate the boards in a mode where the trigger signal is also digitised. This way timing is always accurately defined in relation to the trigger signal. The five V1742 modules are phase synchronised via clock distribution from a master board to the four slave boards. All trigger signals are distributed in parallel to the waveform digitisers. The total digitisation time window is 204.8 ns in 1024×200 ps bins with 12 bit resolution. Hereby resulting in 1536 byte (12*(32*2*2)) bytes) of raw data for every channel. For every digitiser module with 32+4 channels this results in 54 kB of raw data. Giving in total in total 270 kB of raw data without event header information. Applying the factory measured calibration data to every channel requires converting to double precision floating point numbers. Therefore, resulting in 1040 kB per trigger. To save on storage space the waveforms are recorded as uncalibrated raw data together with their calibration data in a MIDAS file. The data structure of the raw data and the data acquisition is discussed in section 5.4.

Digital trigger signals from the IFES modules are directly processed by a CAEN V1495 field programmable gate array (FPGA) module. The logic inside is described in Figure 5.11. The trigger signals from the BGO calorimeter and the downstream scintillator are combined with the result from the FPGA inside the NIM logic (Figure 5.12 and 5.13). A final trigger pulse is eventually created and distributed to the CP80057 VME module, its front-end modules, the V1742 digitisers, and as interrupt signal to the Struck SIS3100 VME master controller. At the same time the Struck SIS3820 scalar counts accepted and missed triggers.

5.2. Intelligent Front-end Electronics for Silicon photo detectors (IFES)

Major parts of this section have been published by Nuclear Instruments and Methods in Physics Research Section A: Accelerators, Spectrometers, Detectors and Associated Equipment in March 2016 [62].

The IFES module that was developed during the course of this thesis is an electronic control and measurement device for operation of silicon based photo detectors like SiPMs. The modules feature a feedback loop controlled constant current source based on a Boost-Converter. The readout of the detector is realised via fully differential balanced signal transmission, followed by an amplifier stage, and a time-over-threshold (ToT) discriminator, providing both a differential analogue signal, and a LVDS pulse encoding a timestamp and energy information. The whole system is built to operate large detector arrays with simple remote control of the current source and the comparator threshold.

5.2.1. Hardware

The block diagram of the IFES modules is shown in Figure 5.4. Figure 5.5 displays an overview of the board. The IFES modules are constructed out of four main components:

1. current supply for the detectors:
    Starting with a DC/DC converter, the current supply for the detectors is produced via a Boost DC/DC converter (LT3482 [66]). On the other hand, a highly precise reference voltage is created to precisely control the high voltage for the detector and the discriminator thresholds by using a digital to analogue converter (DAC) (MAX5135 [67]). The control of the bias voltage uses current control. This way a stable low-noise point of operation can be selected.

2. input stage:
    Starting from the detector itself, the whole signal path is differential. The signal is picked up on the anode and cathode of the detector. Amplification follows with a broad band differential amplifier (AD8351 [68]). Due to the differential signal the cable length of a twisted-pair cable can be as long as 50 cm without distorting the

signal. For cases where no precise timing is required, a signal path of more than 10 m between detector and IFES module has been successfully tested. The input stage is similarly constructed to the "NINO chip" [69, 70]. The main difference is that the whole stage is built from industry grade, easily available components. In contrast to the "NINO chip", both the amplified analogue differential signal and the digital pulse are available to the user. For detector calibration a jumper just in front of the detector is available. This jumper can be used to analyse and monitor the dark current, and the current drawn during operation.

3. discriminator:
   Each channel of the discriminator can be controlled individually with the onboard DAC. The zero point of the discriminator is determined by the precise reference voltage for the detector, allowing the discriminator threshold to have a precision that is better than 1 mV down to the baseline of the signal. The produced pulse is a ToT signal. The start time of the pule is determined by the leading edge of the analogue signal and the threshold. The length of the pulse encodes the length of the analogue signal at the threshold. This is illustrated in Figure 5.8.

4. output stage:
   Noise reduction was one of the leading principles for the design of the IFES modules. To operate the modules in harsh environments like accelerator facilities, signal transportation without distortion or pick-up from noise sources is mandatory. In order to achieve this, all data, all signals, and the control bus are differential. For the control bus and the digital ToT output LVDS drivers are used. This ensures a standardised stable and low-noise signal even for long signal paths. The analogue output is a balanced differential signal produced directly by the amplifier. While this setup cancels the pick-up noise it also suppresses the formation of ground loops by providing a ground-free way of connecting distant DAQ modules with the front-end electronics.

5.2.2. Operation

The main principle of operation is easy handling. An overview graph is shown in Figure 5.6. One or more IFES modules share a common controller, in case of the ASACUSA $\overline{\text{H}}$ experiment this is an Arduino Yún micro controller board. The controller is connected to the IFES modules via the serial peripheral interface (SPI) bus. An user input to the
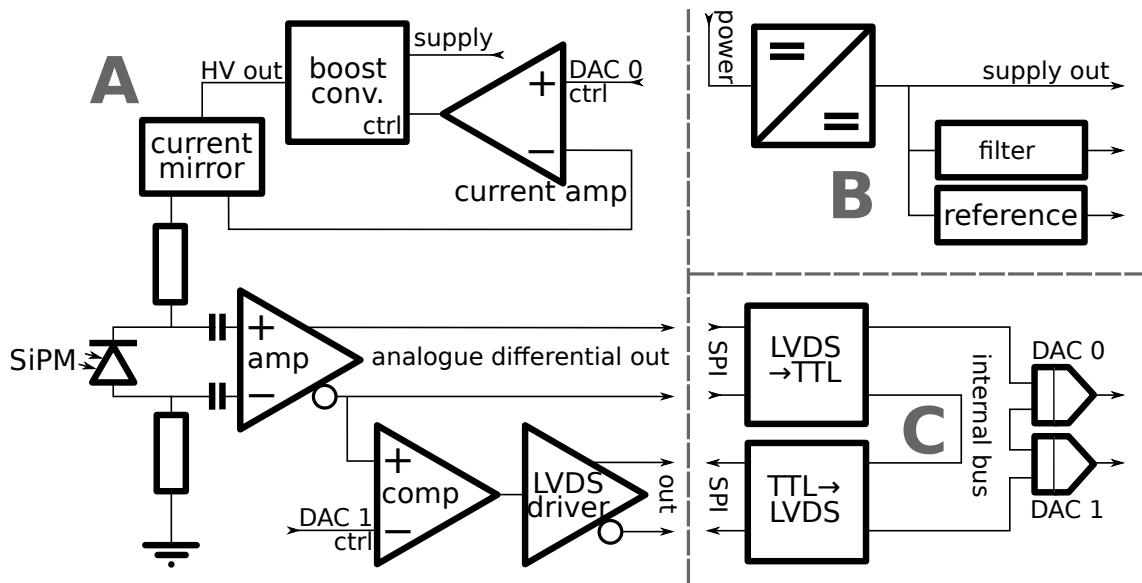
Figure 5.4.: IFES block diagram. **A**: detector bias, differential amplifier and comparator, the signal is produced within the detector marked as SiPM. **B**: power supply with filter and reference voltage. **C**: control bus with daisy chain capability and DAC connections.

controller triggers the writing of the DAC values to the boards. This sets the bias voltage in a range defined by the coarse adjustment screws (Figure 5.5) and it also defines the discriminator threshold. The set bias voltage can be measured on a current measurement port that is usually bridged by a jumper. The signal produced by the detector is transported back to the IFES module, amplified and afterwards provided as output. This output is the amplified analogue waveform. The ToT pulses are sent as LVDS signals to the DAQ electronics. If a temperature sensor is mounted on the board, a feedback look can be created to correct or log temperature drifts. The possible range of the bias voltage in this setup is up to 90 V.

Usually the modules are used to operate arrays of detectors. This case is shown in Figure 5.7. The primary power supply can be daisy-chained from one module to the next. The same is possible for the control bus. As soon as a command is processed by one of the onboard DACs, a ready signal is issued that activates the chip select on the next DAC. By issuing the commands sequentially, all channels can be programmed individually. In the end, the last DAC issues a ready signal that is connected to the controller. This last ready signal can be used to count the number of connected channels in the daisy chain.
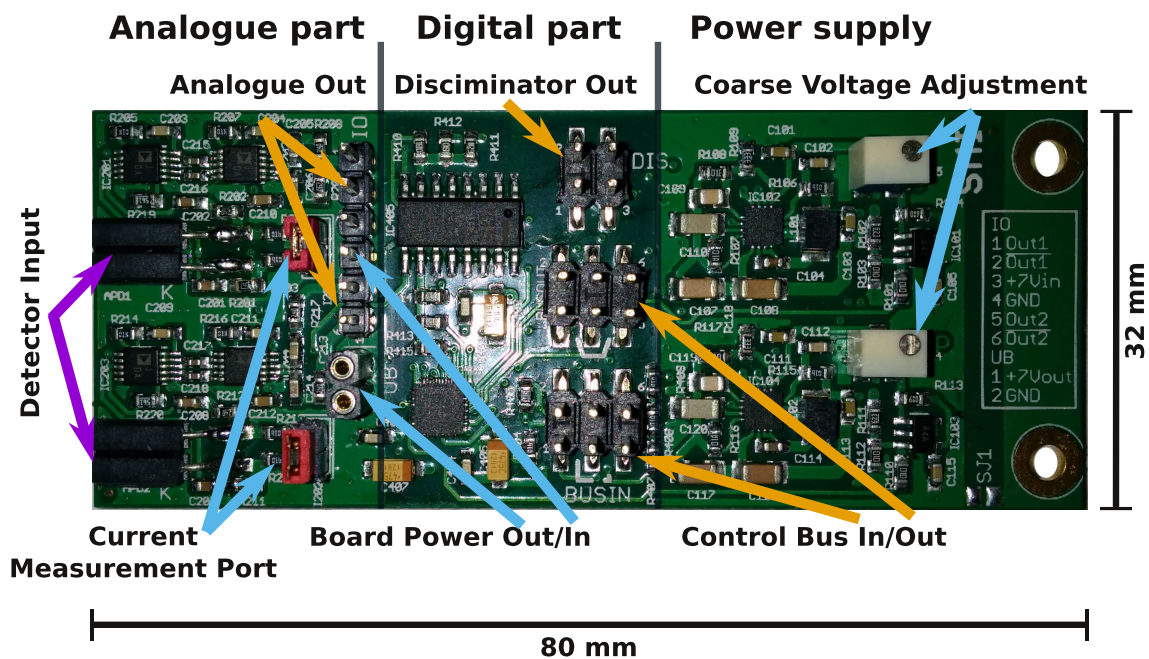
Figure 5.5.: Photograph of an IFES module. The mounting holes can be used for grounding if necessary by closing a soldering bridge (SJ1).
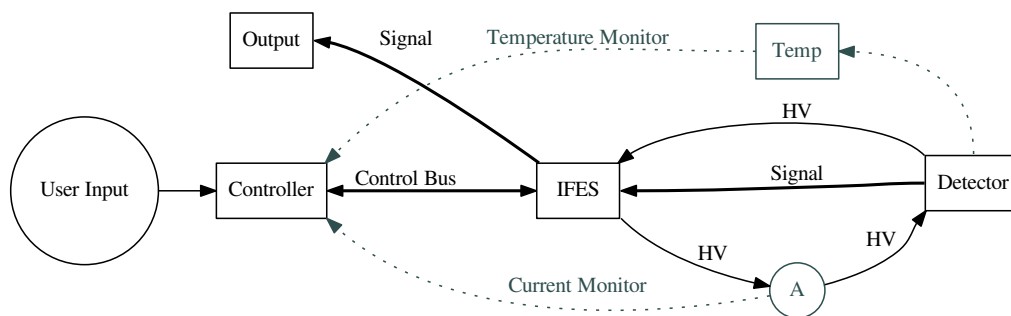
Figure 5.6.: IFES operation, schematic overview. Optional components are gray, mandatory components black. HV is short for the high voltage system, up to 90 V.
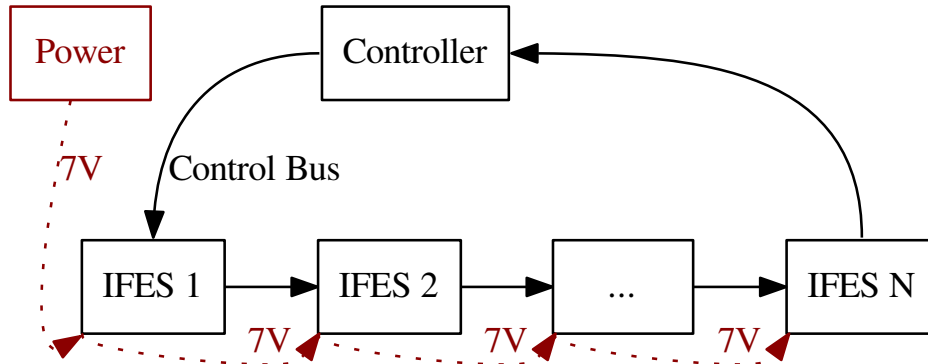
Figure 5.7.: Schematic view of an IFES daisy chain. Power connections are red, control connections are black.

Theoretically this allows an unlimited number of connected channels. For the operation with the ASACUSA $\overline{\text{H}}$ experiment 128 channels, meaning 64 modules, are in operation with one controller. The cascading of many modules allows very compact and dense setups.

5.2.3. Performance of the modules

The evaluation of the board performance was done for timing resolution and for the correlation between the analogue waveform amplitude and ToT length. An example waveform with its time-over-threshold signal as recorded with a V1742 waveform digitiser is shown in Figure 5.8.

Measurements for timing resolution have been performed in January 2014 as a parasitic experiment at the JESSICA beamline at the COSY facility of the Forschungszentrum Jülich in Germany with a 1.471 GeV/c proton beam. The tests were done using EJ-232 (SC1) and EJ-228 (SC2) scintillators with dimensions $28.5 \times 28.5 \times 5$ mm^3 as detector material. KETEK 3350TS and KETEK 3360TS SiPMs (3×3 mm^2 surface area and 50×50 μm^2 and
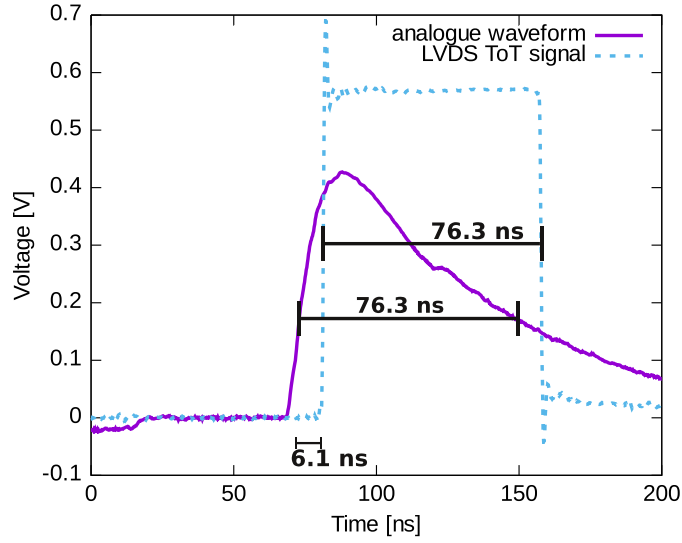
Figure 5.8.: Analogue waveform (solid) and digital ToT signal (dashed), recorded using a V1742 waveform digitiser. The LVDS pulse was converted to an inverted NIM pulse for recording. The rise time (10%-90%) of the analogue signal is 6.1 ns.

$60{\times}60\ \mu\mathrm{m}^2$ micropixel size and optical trench separation) were used as photodetectors [71, 72]. The SiPMs were mounted on opposite sides on the centre of the small surfaces of the scintillator. All signals were recorded using CAEN V1742 VME waveform digitisers operated at 5 GHz sampling rate. The analysis of the waveforms was performed using a self developed library [73], ROOT [74], and rootpy [75]. The bandwidth was limited by a software Fourier filter to 204 MHz.

For evaluation of the timing performance, the time-of-flight (ToF) spectra between the reference counter and the detectors SC1 and SC2, and in between those detectors were measured. The reference signal was produced by calculating the mean time of three scintillators that were read by two photomultipliers each.

The ToF measurements used to determinate the timing resolution of the detectors is shown within Figure 5.9. The histograms were created using constant fraction timestamps derived from the analogue waveforms. The ToF resolution between reference counter and SC1 (EJ-232, KETEK 3360TS) was 174.1$\pm$1.1 ps. Between SC2 (EJ-228, KETEK 3350TS) and the reference signal the ToF resolution was 208$\pm$1.8 ps and between SC1 and SC2 a resolution of 207.2$\pm$0.7 ps was measured. The individual contributions of the detectors
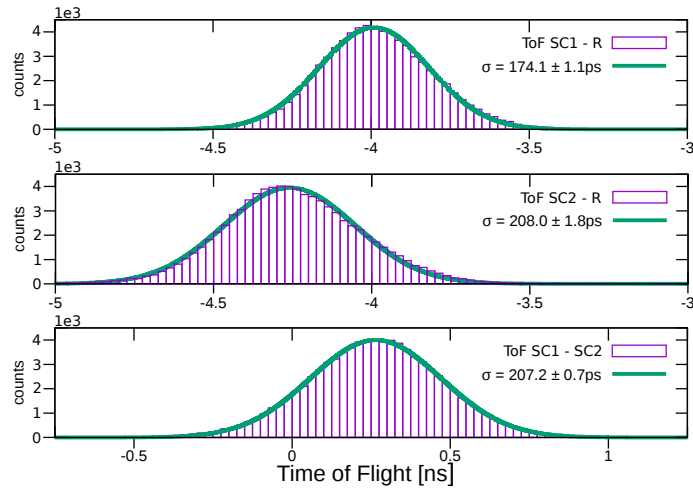
Figure 5.9.: Time-of-flight measurements between the scintillators (SC1 and SC2) and a mean time reference counter (R).

were calculated using a likelihood method. SC1 has a timing resolution of $\sigma = \textbf{122} \pm \textbf{1.3 ps}$, SC2 reaches $\textbf{167} \pm \textbf{1.0 ps}$ and the reference counter contributes $\textbf{123} \pm \textbf{1.3 ps}$.

During the parasitic test beam experiment the main goal was to test every part of the IFES modules under realistic conditions. The board was evaluated with respect to stability of the analogue and digital signals and reproducibility of bias voltage and discriminator threshold settings. It follows that the achieved timing resolution should be considered as easily achievable with the described detectors without tuning the system for high resolution timing.

The correlation between analogue pulse height and ToT signal features two linear regions. After measuring this relation it is possible to use the ToT signal in combination with a multi hit TDC to measure charge deposit and timing in the same instance. A measurement of this relation is displayed in Figure 5.10. Furthermore, timewalk correction of the leading edge timestamp is possible with the ToT signal.
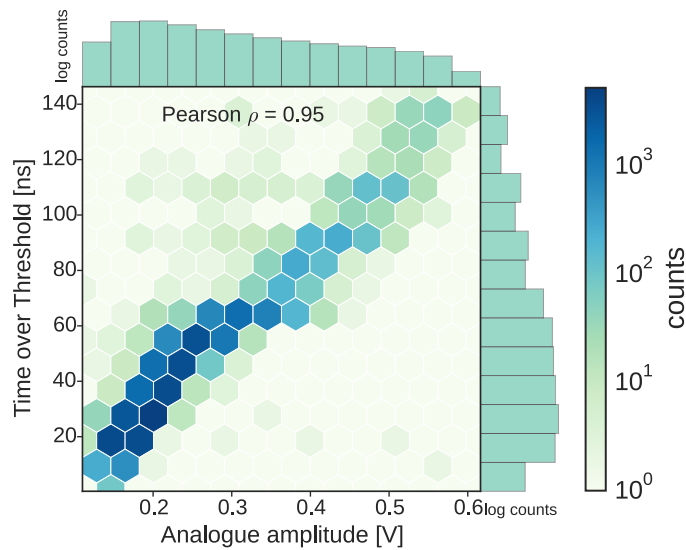
Figure 5.10.: Correlation between analogue pulse height and ToT. The bin content for the bivariate histogram and both marginalised distributions is on a logarithmic scale to emphasise the correlation. The Pearson product-moment correlation coefficient ρ is 0.95.

5.3. The trigger

Theoretically the system can operate with two different trigger types. In the case of the main event trigger, it can be operated with three different trigger modes. During the experiment the main trigger mode and the calibration trigger were integrated in the same DAQ channel. For the sake of a continuous discussion I will start the discussion with the calibration trigger. A summary of the different modes is in Table 5.2.

Calibration / MIP trigger

The calibration trigger is set to record upstream annihilation of $\overline{p}$s on the beampipe walls or inside of the cusp trap. The charged pions travel through the beamline vacuum and produce a signal in the BGO calorimeter and the downstream scintillator.

Table 5.2.: trigger types, x = do not care

Trigger name	Inner hodoscope	Outer hodoscope	BGO	Downstream scintil.
MIP trigger	0	0	1	1
hodoscope only	≥ 1	≥ 1	x	x
BGO only	x	x	1	x
event trigger	≥ 1	≥ 1	1	x

The fast dynode trigger from the BGO detector and the trigger signal from the downstream scintillator pass a coincidence unit and if no veto signal is on a "logical one" state the final state trigger signal is produced.

The main purpose of this signal type is recording data for energy calibration of the BGO calorimeter.

Event trigger

This trigger type is produced by a combination of all individual hodoscope channels and the fast dynode trigger from the BGO calorimeter.

Each individual hodoscope channel can trigger on an individually selectable threshold, producing in total 128 trigger sources for the hodoscope alone. These pulses are transported as LVDS signals to the V1495 FPGA module. The flow diagram in Figure 5.11 shows the treatment of the individual hodoscope signals inside the FPGA. The programming of the Altera Cyclone EP1C20F400C6 FPGA on board was done in very high speed integrated circuit hardware description language (VHDL) using the Altera Quartus 2 development environment. To avoid artificially introduced delays, an asynchronous VHDL design was used. This way the signal propagation is not delayed by registers that operate on clock edges. Verification of the design was done using the simulator inside the Quartus 2 environment. The total trigger propagation time was measured to be ≈ 6 ns using a pulser. The same setup revealed a gate transition time of ≈ 1 ns per look-up-table. The trigger condition for the hodoscope is built of three stages inside the FPGA:

1. coincidence between upstream and downstream SiPM for every bar separately.

2. logical "or" of each full hodoscope layer

3. logical "and" between both layers and the inverted signal from a veto "or".

After leaving the FPGA the coincidence between the hodoscope signal and the BGO dynode trigger is checked. If this condition is satisfied, a final state trigger is issued and distributed to the V1742 waveform digitisers, the CP80057 BGO readout module, and the scalar for reference. At the same time a deadtime veto is produced to suppress trigger generation during the digitisation and readout process, and an interrupt is raised in the SIS3100 VME master to signal the DAQ the availability of data.

During injection the experimental area is flushed with annihilation pions and all detectors saturate. Therefore, the AD injection pulse is used as veto condition to block all data recording. One issue that arises from not using this veto is, that the phase lock synchronisation of the V1742 modules is lost; this would compromise all data till the module undergoes a full reset.

The detailed process flow is displayed in Figure 5.12 and Figure 5.13. Data acquisition and interrupt handling is discussed in the next section (section 5.4). The timing diagrams of the different trigger types and the AD veto are shown in Appendix section A.3.

5.4. Data acquisition

As noted in earlier sections the data acquisition is implemented in MIDAS[2], which is a DAQ system developed by the Paul Scherrer Institute (PSI) and the Tri University Meson Facility (TRIUMF). It is a multi-process system with a core server, called the MIDAS server or *mserver*, a separate data logger (*mlogger*) and an integrated web server (*mhttpd*) for monitoring and controlling of the operation. Configurations and intermediate data are stored in an online database called ODB. The values stored in this data base can be modified either via the web interface or conveniently using a commandline interface (CLI) called *odbedit*. Note taking during operation can be done using an integrated electronic

---

[2]https://midas.triumf.ca
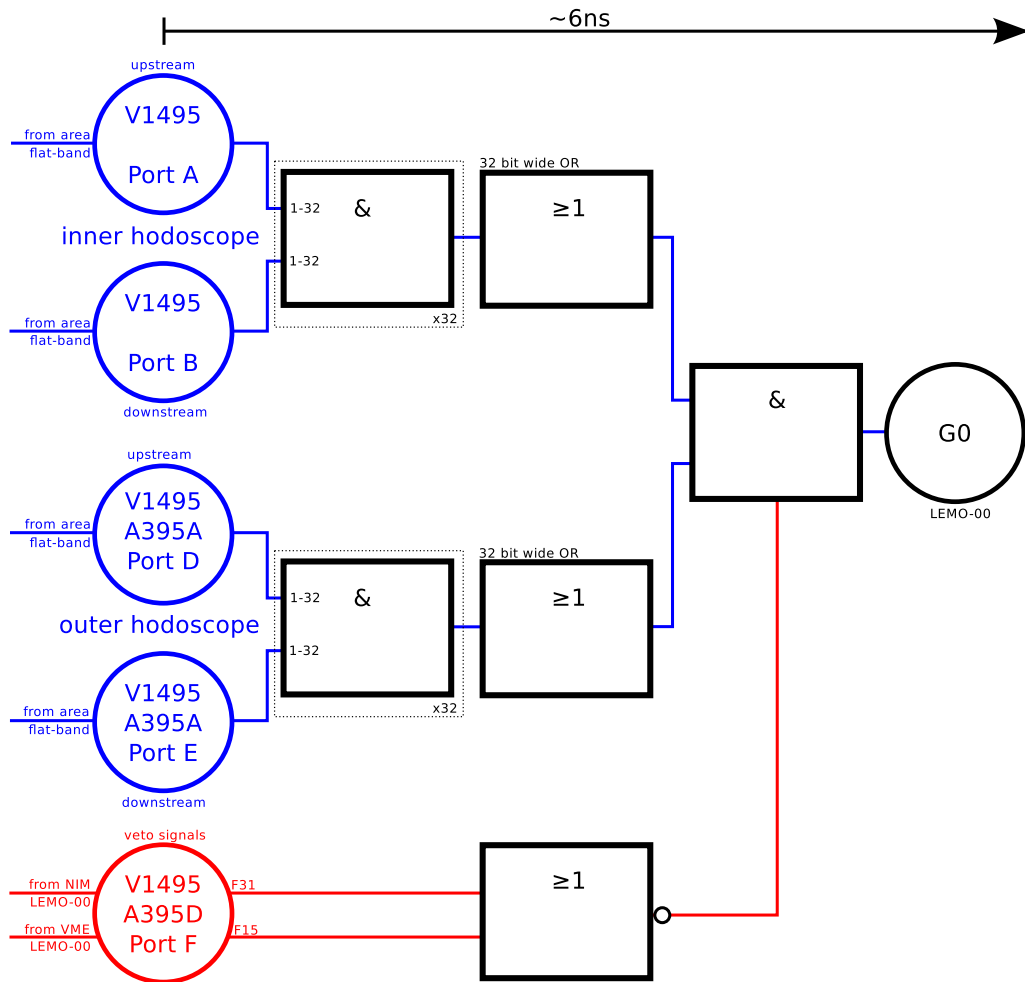
Figure 5.11.: FPGA logic. red: veto path, blue: trigger signals
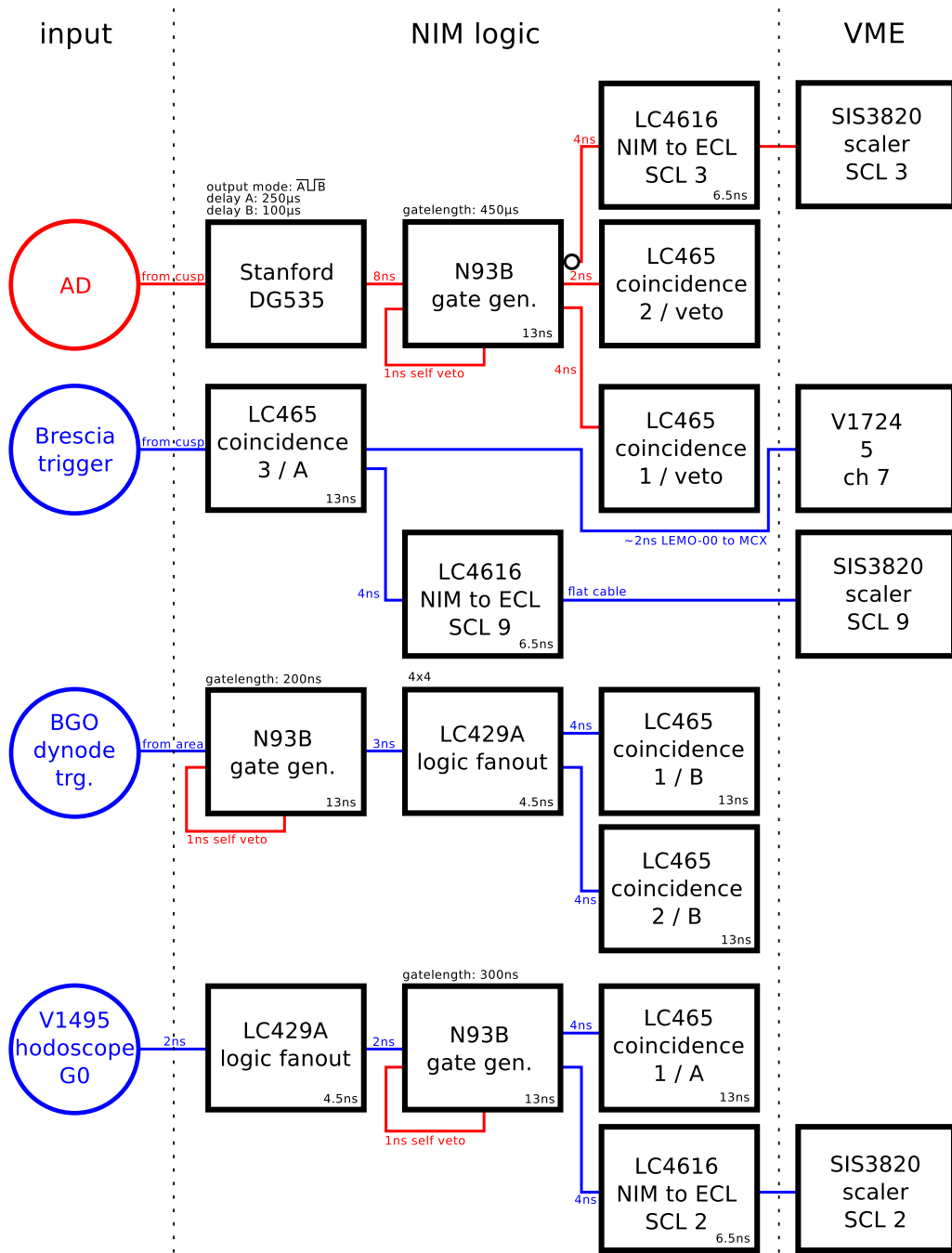
Figure 5.12.: Trigger layout part 1. red: veto path, blue: trigger signals. Delays are written for each component. Circles indicate signals coming from or going into the beam area.

input

NIM logic

VME

LC4616
NIM to ECL
SCL 0
6.5ns

SIS3820
scaler
SCL 0

flat cable

1ns

1x16

LC465
coincidence
1 / OUT

1ns

LC429A
logic FanOut
4.5ns

4ns

4ns

SIS 3100
IN 1

~2ns LEMO-00 to MCX

V1742
1 - 5
Trg 0 &1

gatelength: 200μs

N93B
gate gen.
13ns

1ns

vetos BGO MIP trigger

LC465
coincidence
2 / C
13ns

1ns self veto

4ns

V1495
FPGA
veto 1

vetoed by BGO+hodos.

LC465
coincidence
2 / OUT

1ns

4x4

0.5ns

LC429A
logic FanIn
4.5ns

to area

BGO
trigger

MIP
trigger

from area

LC465
coincidence
2 / A
13ns

4-8
&
10-14

from area

LC4616
NIM to ECL
4-8/10-14
6.5ns

flat cable

SIS3820
scaler
4-8/10-14

Figure 5.13.: Trigger layout part 2. red: veto path, blue: trigger signals. Delays are written for each component. Circles indicate signals coming from or going into the beam area.

logbook (ELOG) system. In case of our DAQ setup, the internal ELOG is used and regularly synchronised to a central logbook on the Stefan Meyer Institute for subatomic physics (SMI) servers in Vienna.

For operation of the DAQ system, a minimum of two user supplied programs are required, one or more *front-ends* and an *analyser*. The internal workings of the analyser, together with its performance on raw data analysis, will be discussed in section 6.1. This section focuses on the structure of the front-end code and its generated raw data.

The following subsections will discuss the structure of the front-end code including timed readouts, followed by the handling of the interrupt based event trigger and closed by a description of the raw data structure. Currently, only the VME front-end is in operation, additional front-ends for temperature readings and slow control of the detector are prepared but not fully implemented. Programming MIDAS front-ends to run on the Arduino Yún microprocessor modules needs special care as the endianness differs[3] from the x86_64 processor used in the server machine. In the following only the VME front-end will be discussed.

5.4.1. The VME front-end

MIDAS provides a common structure for front-ends that take the form of a system provided module *mfe.o*. By linking against this module, the resulting program is prepared to integrate into MIDAS. The user is must provide equipment information as a C structure and functions to start, stop, pause, and resume a data taking run. It is also required to provide a function for initialisation on startup of the program and another one for a clean shutdown. Those functions are activated by the MIDAS server using remote procedure call (RPC) in case of state transitions. In addition a loop function can be defined. In the case of our DAQ, the loop function is used to check hardware responses and monitor if the hardware is still in a sane state or if it needs a restart.

Four equipment types are defined:

InterruptTrigger this type uses the EQ_USER flag for interrupt driven readout. A detailed explanation follows in subsection 5.4.2.

---

[3]The Atheros AR9331 is a big-endian processor [76]

ClockTrigger a periodic readout event for measuring the pedestal of the BGO calorimeter. Every minute a software trigger is issued to sample random data for a precise determination of the pedestal. At the same time, drifts of the pedestal can be monitored.

V1742 this event type is used to manually, and additionally at the beginning of every run, record snapshots of waveforms. At the same time, the correction data for the current setting of the waveform digitisers are stored within the MIDAS file. This correction data are essential for a high resolution of the recorded waveforms.

SIS3820 a periodic readout of the scalar. If a new trap cycle starts, an asynchronous readout call in a thread is started to store the cusp trap run number in the MIDAS files and tag every event with this number. In case a start signal is detected by the scalar, the current run can be stopped and restart with a new run number to get a separate MIDAS file for every trap cycle.

The main thread of the front-end program takes care of initialisation of all modules, state tracking, and issuing a warning in case a hardware component reaches a critical state. In terms of data taking, the main thread reads periodically the SIS3820 scalar, handles manually issued triggers and start of run triggers for the V142 waveform digitisers and periodically creates and reads the software defined clock trigger.

Automatic starting and stopping of runs is done if a trap cycle start signal is detected by launching a separate thread that calls *odbedit* with a "stop" and followed by a "start now" command.

Synchronisation of the cusp run number is done by accessing a file *traprunnumber* via network file system (NFS) on the cusp control computer *pcad308*. Again, a separate thread is used for reading the file, and if for some reasons the network file can not be read this would still guarantee data taking without artificial deadtime.

5.4.2. Threaded interrupt trigger handling

Interrupt processing and configuration is handled by the sis3100 class[4]. This class is constructed in a way that it can seamlessly integrate into MIDAS, but at the same time it can operate as a standalone program for easy debugging and testing of VME code.

The sis3100 class constructor

The constructor takes a sis3100 device number and a function pointer to a readout function (described below in "Trigger handling"). Afterwards, an empty signal mask is created and masked with *SIGUSR1* according to the Struck SIS3100 manual [77].

```cpp
sis3100::sis3100(int sisDeviceNum, bool (*eventFunction)(int, int, int)
    ){
  sigemptyset(&mask);
  sigaddset(&mask, SIGUSR1);
```

The signal is blocked in the main thread and the old signal masked is saved. A new thread is started thereafter, which inherits the blocked signal. The threadData object, containing pointers to the MIDAS status variables, and to the function pointer eventFunction, is passed to the new thread.

```cpp
  pthread_sigmask(SIG_BLOCK, &mask, &old_mask);
#if HAVE_MIDAS__
  create_event_rb(0);
  thread = ss_thread_create(&interruptThread, (void *) &threadData);
#else
  pthread_create(&thread, NULL, &interruptThread, (void *) &threadData)
      ;
#endif
```

Trigger handling

The interrupt handling thread is described in the UML 2 activity diagram in Figure 5.14. The entry point is a *sigtimedwait* with a time limit of 500 ms. If the time limit is reached,

---

[4]The source code is published on GitHub: https://github.com/Stefan-Meyer-Institut/MIDASdrivers

the system state is checked to ensure proper shutdown and reaction to state changes in MIDAS. The 500 ms time limit are a good compromise between keeping the deadtime as low as possible and on the other hand getting prompt reactions from the readout thread.

If the system is running, and a proper interrupt accepted, meaning not only the SIGUSR1 is checked but also the SIS3100 status, then the readout chain is started. At first, a software veto gate is created on the NIM output of the SIS3100, later the MIDAS ring buffer handle is acquired and the system prepared. At this point, the user defined readout function is invoked.

The readout function can be programmed in the same way as any other MIDAS function, creating bank entries and storing data. Next, the interrupt vector is checked, and if it corresponds to a front panel interrupt on NIM input one, the event is processed. The event structure is initialised, the cusp run number is stored for synchronisation, the V1742 module and the CP80057 module are read.

After assembling the event, it is sent to the MIDAS ring buffer. When returning from the user function the interrupts are acknowledged and the veto gate is closed. At this point, the thread is ready to receive another trigger.

5.4.3. Data structure

Within a MIDAS file, the data follows two hierarchical structures. The first one is the event identification number (ID), which is closely related to the equipment type. This number is the primary identifier to distinguish different types of events. If one equipment type can produce different events depending on trigger conditions a trigger mask can be used to further structure the data.

The second level are the MIDAS banks. Each event type can have multiple banks. Each bank has a defined data type and holds the actual data. Naming of banks has to follow a strict system. Each bank name can only be a combination of four alphanumeric symbols. A full overview of the raw data structure in the MIDAS files is shown in Table 5.3.

If the system detects a trigger in one of the equipment types, a new event is created and for each event ID an event number is assigned. This way the raw data can be accessed

Table 5.3.: Structure of raw data, BOR means "begin of run", and EOR stands for "end of run"

Equipment	ID	MIDAS banks		ROOT TTree
SIS3820 (periodic)	11	SCL0	data	ScalarDataTree
		SCLT	timestamp	
V1742 (BOR, EOR, manual) InterruptTrigger	20 1	A1DA	raw data	ManualEventTree HbarEventTree
		A1TP	DRS4 temp.	
		A2DA	raw data	
		A2TP	DRS4 temp.	
		A3DA	raw data	
		A3TP	DRS4 temp.	
		A4DA	raw data	
		A4TP	DRS4 temp.	
		A5DA	raw data	
		A5TP	DRS4 temp.	
ClockTrigger (periodic) InterruptTrigger	10 1	CPAD	ADC data	ClockEventTree HbarEventTree
		CPAR	raw data	
		CPBD	ADC data	
		CPBR	raw data	
		CPCD	ADC data	
		CPCR	raw data	
		CPDD	ADC data	
		CPDR	raw data	
		CPAH	event header	
		CPBH	event header	
		CPCH	event header	
		CPDH	event header	
		CPTD	timestamps	
		CPQD	integrated charge	
V1742 (BOR, EOR, manual)	20	AxyC	cell correction	x=ADC, y=group
		AxyN	nSample corr,	
		AxyM	time correction	
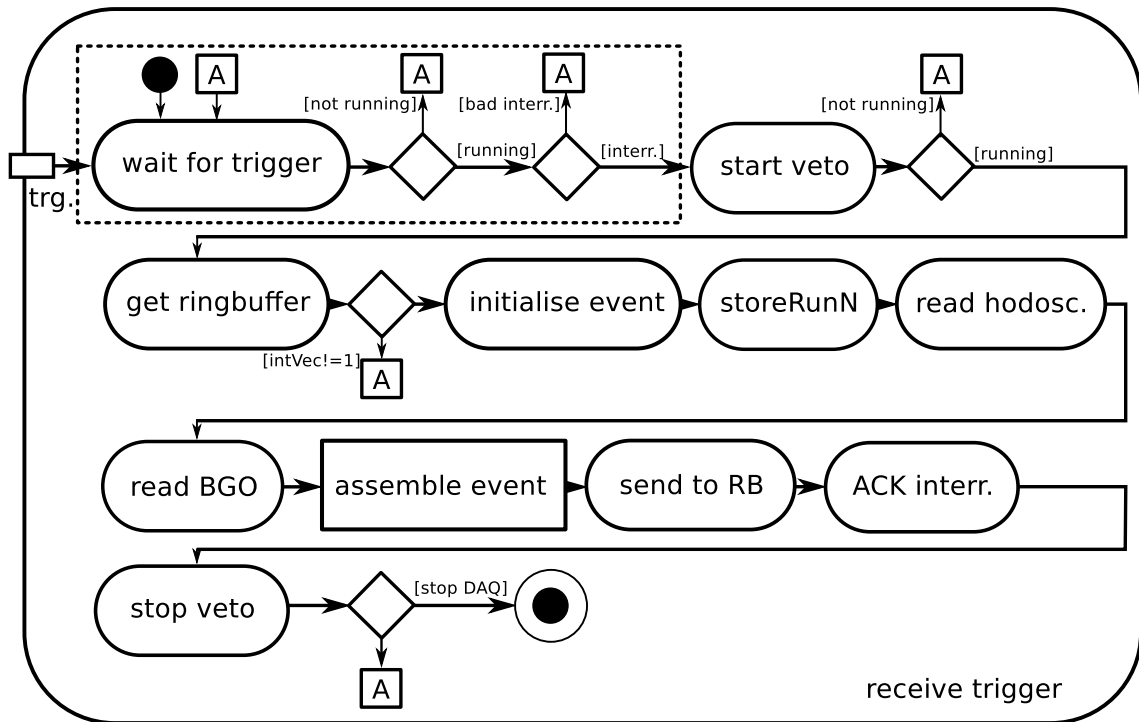
Figure 5.14.: Trigger readout activity diagram. The program entry point is in the top left corner together with the external trigger signal. The "A" label represents a jump for returning the function flow back to "wait for trigger".

using the event ID, and afterwards by the event number. If a certain analysis only requires loading some of the banks, only the necessary data need to be loaded from the file. The ROOT TTrees are created using the analyser as a separate program as described in section 6.1.

6. Data analysis and Results

The following chapter is dedicated to all forms of data analysis performed for the ASA-CUSA $\overline{\text{H}}$ experiment. In particular, in the first section I will discuss the analysis of the raw data recorded by the DAQ system. This includes the preparation of recorded waveforms and the procedure to create ROOT files from the MIDAS raw data storage files.

Within the second section, methods for data cleaning, removing coincidence noise, the evaluation of the detector performance, and identifying anitproton annihilations are presented. The third section will briefly deal with analysing the resulting data by comparing the average antihydrogen count rate during production with background measurements.

6.1. Raw data analysis

The conversion of the recorded raw data is done using a program called `OnlineAnalyser`. This analyser can operate in two distinct modes:

1. **online mode**: Data are directly accessed in memory through the MIDAS framework. In this configuration, the analyser ROOT files are produced on-the-fly while recording the data and writing the raw files to the hard disc. Operation in this mode is time critical. If the analysis runs slower than data are recorded, the analyser might crash due to memory issues.

2. **offline mode**: Raw data files stored on disc are processed. This mode runs separately from the data acquisition. Therefore, more computation intensive analysis methods can be employed, leading to significantly longer processing times.

In general, both modes could be used for processing live data and for processing MIDAS files. The only difference is in feasibility due to the longer processing time of the offline mode. The process of analysing the data follows a common structure:

1. read event ID and check if the event structure is valid and if all expected data are available.

2. dispatch event data to the correct analysis routines identified by the event ID.

3. collect analysis results and store in ROOT `TTrees`.

In the following, I will discuss the details of the analysis, starting with the individual event IDs. Then later on continuing with the details of the waveform analysis.

ID 1: $\overline{\mathrm{H}}$ trigger event

1. get MIDAS event timestamp

2. check sanity of data, especially if all MIDAS banks are present

3. prepare event data for waveform analyser

4. analyse waveforms

5. decode BGO data from CP80057

6. *(optional)* plot data using `gnuplot` every 5 seconds when running in online mode

7. decode V1742 temperatures

8. read cusp run number

9. store data in ROOT TTree

ID 10: clock trigger event

1. get MIDAS event timestamp

2. check sanity of data, especially if all MIDAS banks are present

3. decode BGO data from CP80057

4. *(optional)* plot data using `gnuplot` every 5 seconds when running in online mode

5. store data in ROOT TTree

ID 11: scalar event

1. get MIDAS event timestamp

2. check sanity of data, especially if all MIDAS banks are present

3. decode raw scalar data stream

4. store data in ROOT TTree

ID 20: waveform digitiser correction data and random sample data

1. get MIDAS event timestamp

2. check sanity of data, especially if all MIDAS banks are present

3. check and update V1742 correction tables

4. prepare event data for waveform analyser

5. analyse waveforms

6. plot waveforms

7. decode V1742 temperatures

8. store data in ROOT TTree

The analysis of the recorded waveforms is done using a self developed waveform library [73]. The key concept behind this development was to create a versatile, easy to use, and expandable library that can be tuned to perform different analysis tasks. In the case of the `OnlineAnalyser`, the signal channels and the trigger channels are treated differently. The following sequence is used for the triggers:

1. convert ADC bits to voltage

2. subtract baseline by calculating the arithmetic mean of the first 10 ns.

3. calculate leading edge (LE) timestamp and time-over-threshold.

4. calculate constant fraction (CF) timestamp.

To achieve an improved timing resolution, the signal timestamps are measured with respect to the trigger signal as indicated in the V1742 manual [78]:

1. shift signal by 200 ns (ensures that final times are positive after subtraction of the trigger)

2. subtract trigger timestamp for each ADC group

3. convert ADC bits to voltage

4. apply fast fourier transform (FFT) low-pass filter with cut-off frequency 205 MHz (*offline mode only*). The left side of Figure 6.1 shows the effect of the filter.

5. subtract baseline by calculating the arithmetic mean of the first 10 ns.

6. detect if signal is negative or positive

7. calculate LE timestamp and time-over-threshold.
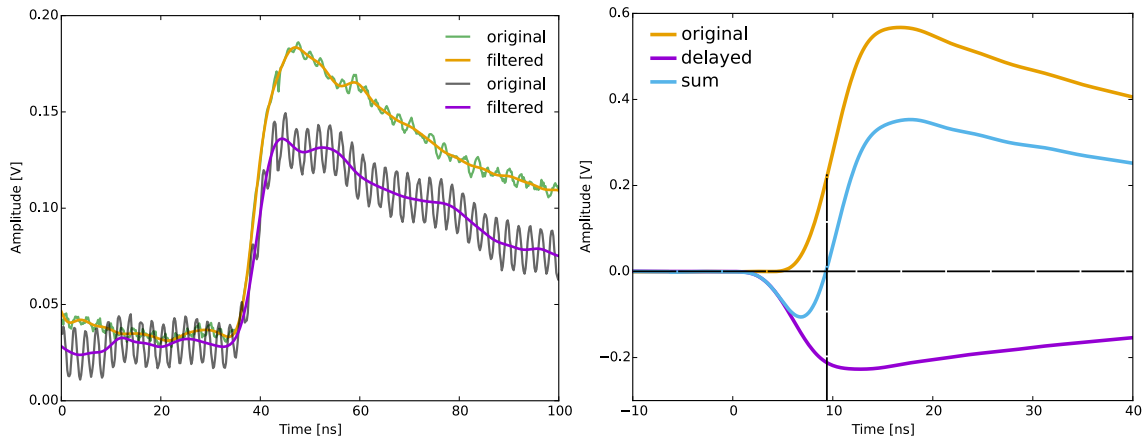
Figure 6.1.: **Left**: effect of FFT filtering, the noisy original waveforms are cleaned, while the rise time of the signal in the filtered waveform is preserved. **Right**: mechanics of the constant fraction implementation. A copy of the original waveform is inverted, delayed, and multiplied with a small number. The sum of both is a bipolar signal with a defined zero crossing at a constant fraction of the signal. This method was chosen as the waveform library [73] and should be able to handle signals that are truncated by the ADC while still providing a reliable CF timestamp.

8. calculate detected charge by integrating over the waveform

9. calculate CF timestamp, *online:* single timestamp, *offline:* arithmetic mean of 10 evenly distributed fractions. The right side of Figure 6.1 shows the principle of operation.

6.2. Data corrections

The pre-analysed data are stored in TTrees, most notably the `HbarEventTree`. Those trees contain all the measured data from the raw analysis in an easily accessible and structured way. A complete summary of all recorded TTree leaves is available in Table B.2 and Table B.1. These data still need to be corrected for differences in cable length, inaccuracies of positioning, and gain drifts, among other corrections.

In the case of the central BGO detector, two types of corrections are applied. First, the individual channels for each of the multi-anode PMTs are calibrated to each other. This was done by Y. Nagata by measuring the gain of each channel in a dark box with a white light-emitting diode (LED) that uniformly illuminates all channels. Additionally, the four PMTs are calibrated to each other by comparing their energy distribution of measured cosmic particles between the PMTs. The energy calibration is determined by comparing the measurements with Geant4 simulations. All calibration data for the BGO detector are supplied by Y. Nagata.

The first correction for the hodoscopes is to compensate differences between upstream and downstream SiPMs. For each individual bar, a factor is calculated to level out gain differences between both sides. This factor is defined by calculating a kernel density estimate (KDE) for every energy distribution and taking the ratio of maximum values (the mode of the distribution). Alternatively, the ratio between the statistical means of both distributions can be used. Afterwards, cable differences are compensated by calculating the median of the timing distributions. The median is a stable central tendency measure, therefore it can be used to calculate the offset between upstream and downstream SiPM.

When investigating the dependence of CF timestamp difference with the mean time of upstream and downstream SiPM, a triangular shaped feature emerges (left graph in Figure 6.2). This shape is determined by the trigger jitter in the FPGA, and depending on the signal path in the FPGA, the mean changes. If time differences are measured this effect cancels. The displayed data are cosmic events recorded during an AD outage. Therefore, almost no additional background is present. The marginalised time difference distribution has a stable central tendency but wide tails, which is partly expected from the $\cos^2$ angular distribution of incident cosmic particles [79]. However, the extent of the tails is unexpected given the small length of the hodoscope bars in comparison to the speed of light. Looking at the mean time distribution, it can be immediately seen that it is highly skewed due to the triangular structure. From the fact that light created by the scintillation process in the bars always needs to travel the whole length of the bars to produce a signal in both SiPMs, one can deduce that the mean time should be a constant. It follows that the distribution is expected to have a Gaussian shape. The skewness[1] of the mean time can be corrected by fitting a linear regression into the data and compensating the time drift. The resulting distribution is shown in Figure 6.2 on the right side.

---

[1]The skewness is a measure for the asymmetry of a distribution, negative skewness inficates an asymmetry towards lower values. Whereas, a positive skewness indicates an asymmetry towards higher values in the unimodal case.
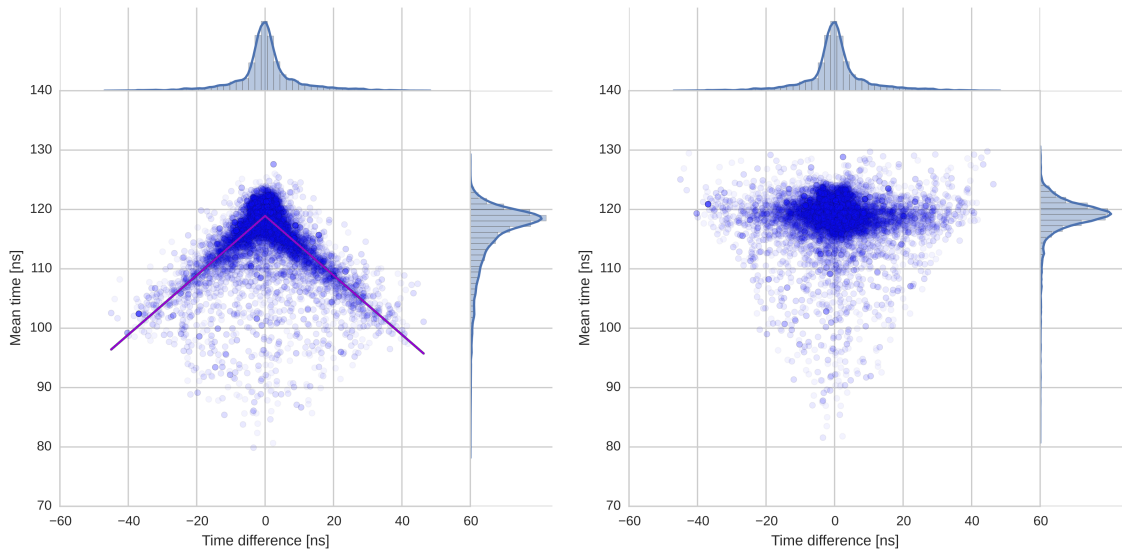
Figure 6.2.: **left**: correlation of difference between upstream and downstream CF timestamp and the mean time of all bars in the outer hodoscope. A linear regression for compensating mean time shifts is drawn in violet. The marginalised distributions are plotted as histograms with their KDEs. **right**: correlation after correcting the mean time shift, the marginalised mean time distribution is now less skewed and narrower. This effect is explained by the trigger jitter from the FPGA.

A numerical summary of the distributions is presented in Table 6.1. In the case of a Gaussian distribution, the skewness and excess kurtosis[2] should both be zero. After correcting for the drift, the skewness and excess kurtosis get close to zero but are not vanishing. This hints at a contamination of the data of some kind.

---

[2]The kurtosis describes the curvature of a distribution. The excess kurtosis describes a deviation of the curvature with respect to the normal distribution. In the case of a positive excess kurtosis, more weight is on the tails of the distribution. Whereas, if the excess kurtosis is negative the peak is emphasised, in the unimodal case.

Table 6.1.: Summary of statistical data for the CF time difference between upstream and downstream SiPM and the mean time distributions before and after correction for both inner and outer hodoscope. The table contains the sample mean (μ), the sample standard deviation (σ), the 25%, 50% (median) and 75% quantiles, the skewness and the excess kurtosis.

	μ [ns]	σ [ns]	25% [ns]	50% [ns]	75% [ns]	skew.	kurt.
outer Δt	0.41	9.53	-2.83	0.00	3.21	0.21	3.53
inner Δt	0.35	5.01	-1.37	0.00	1.61	0.40	9.44
			before correction				
outer mean time	115.58	5.58	113.85	117.44	119.05	-1.90	4.52
inner mean time	118.12	2.96	117.45	118.82	119.78	-2.94	15.58
			after correction				
outer mean time	119.32	1.86	118.14	119.30	120.50	0.01	-0.04
inner mean time	119.75	1.33	118.95	119.79	120.58	-0.13	0.96

6.3. Comparison between cosmic events and pbar annihilations

Determining detector performance is done by comparing measured data with simulation results from Geant4. In the case of data from cosmic events, the angular distribution is $\propto \cos^2$ distributed [79]. The cosmic ray simulation was done in Geant4 with the CRY [45] generator version 1.7. The antiproton annihilations were simulated with the SMI developed annihilation process for Geant4 (chapter 4).

In Figure 6.3 comparisons of angular distributions with simulations are plotted. The measured angular distribution data are shown in the top right graph of Figure 6.3. The graph is split into four separate parts. The left column represents comparisons with cosmic background data. The right column shows the antiproton annihilation data. Each of the columns is split into direct measurements, and simulations (top) and ratios (bottom). For the direct measurements the upper graph displays the measured distributions of both hodoscope layers. The middle graph shows the inner layer with its simulation, and the lower graph shows the outer layer with simulation results. The top graph
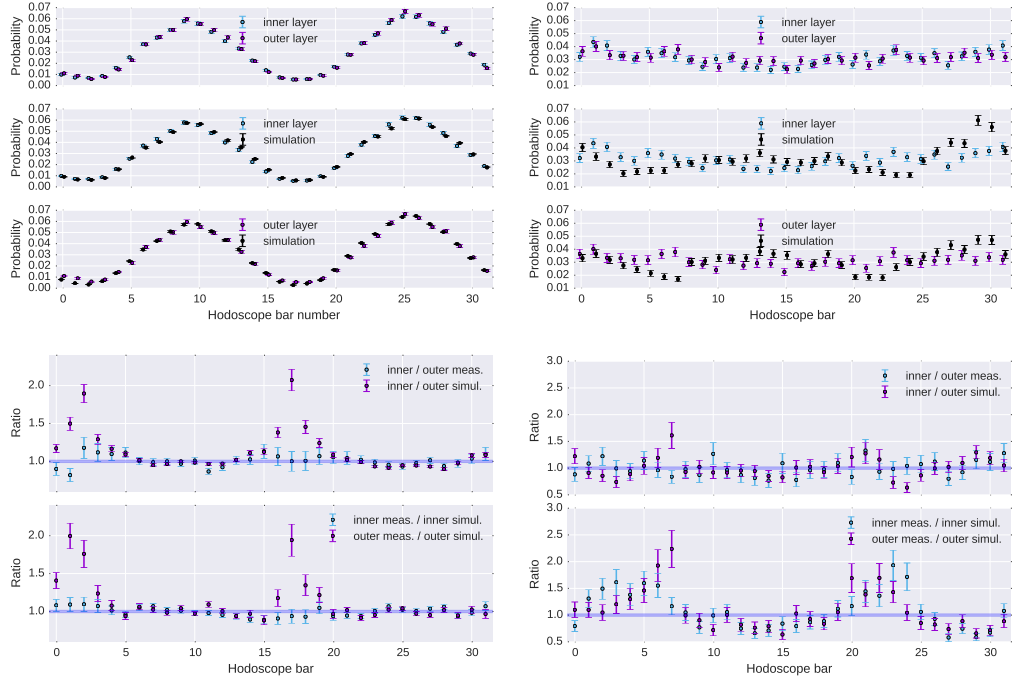
(a) data from cosmic rays　　　　(b) antiproton annihilation data

Figure 6.3.: Comparison of angular distribution of cosmic data (**Left**) and pbar annihilations (**Right**). All data are normalised as PMFs. **Top:** direct comparison of inner and outer hodoscope (top), inner hodoscope data with simulations (middle) and outer hodoscope data with simulations (bottom). **Bottom:** ratios of inner and outer hodoscope data in blue, and ratios for simulations in violet (top). Ratios of inner hodoscope and simulation in blue, and of outer hodoscope and simulations in violet (bottom). In the legend, "meas." is short for measurement, and simulation is shortened to "simul.".
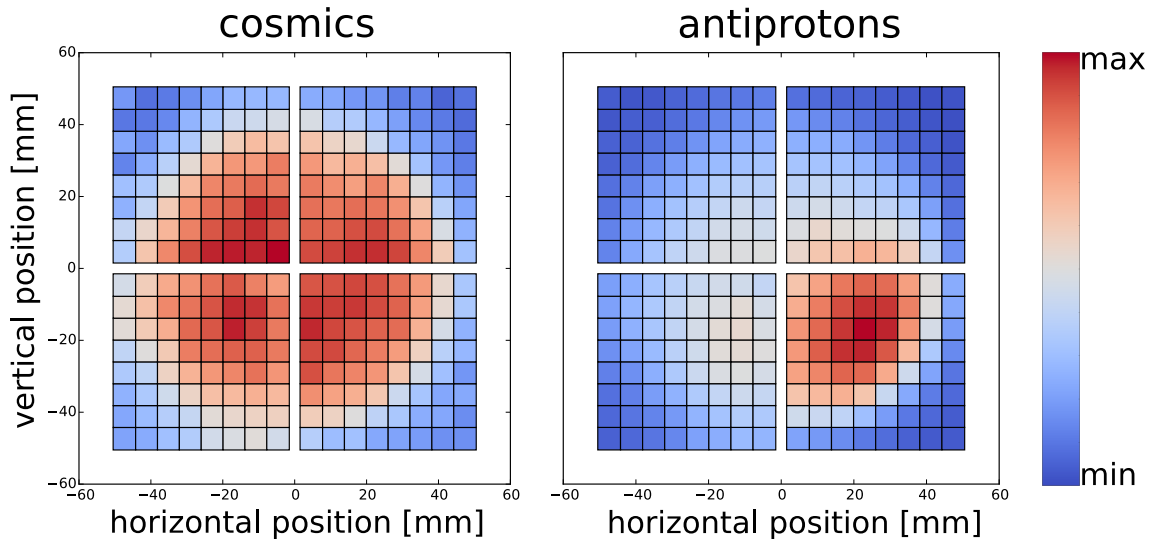
Figure 6.4.: Light distribution in the BGO detector for cosmic rays during machine shup-
down (**left**) and for antiproton annihilations (**right**). The heatmaps are norm-
alised individually to their minimum and maximum integrated ADC values.

shows the ratio between inner and outer hodoscope for measured data and simulations.
Whereas, the bottom graph shows the ratio between the respective hodoscope layer
and the corresponding simulation. When looking at the measured data (top panel) it
can be immediately seen that inner and outer hodoscope produce consistent results.
This is also supported by the ratios of inner and outer hodoscope (right bottom graph).
The simulations create a different picture. Investigating the deviation from simulation
revealed that the hit position of the antiprotons on the BGO have a non-trivial shape and
the angular distribution is strongly dependent on the actual hit position of the antiproton
beam which is difficult to reproduce in simulations (compare Figure 6.4 for the measured
light distribution in the BGO). As a first approximation the simulated antiproton beam
was set to hit the lower right corner of the BGO.

In the case of the outer hodoscope, small deviations from the simulations of cosmic rays
are observed. This is due to the limited particle emitting surface (3×3 m^2, limited due
to computation power) in Geant4 with the CRY library. Therefore, large impact angles
(hodoscope bars 0 to 3 and 16 to 19 - compare Figure 5.2) are not accurately simulated.
This effect is nicely visible in the lower left graph of Figure 6.3. The top panel shows the
ratio of inner and outer hodoscope per detector bar number. In the case of the measured
data, the ratio is very consistent with being one, whereas the ratio of the inner and

outer hodoscope from simulations shows two peaks, with the first one between bar number 0 and 3 and the second one between 16 and 19. Consequently, the same feature appears when calculating the ratios between measured data and simulations (lower panel). It can be seen that the data between inner and outer hodoscope are consistent with each other for the full detector. The data for the inner hodoscope are consistent with simulations. While consistency with simulation for the outer hodoscope is only satisfied for the detector panels that do not directly face to the sides. This effect results from an insufficient simulation of the cosmic background (a very large emitting surface in the CRY library would be necessary).

Another important gauge for the reliability of detector data are hit multiplicities. In Figure 6.5 the measured multiplicities for cosmic rays and antiproton annihilations are compared. Again, the figure displays the cosmic background results in the left column and the antiproton annihilation results in the right column. The two graphs on top of each column show the measured multiplicities for both hodoscope layers in comparison with simulations. The lower graphs display the ratio between measured data and simulations (top) and the ratios between inner and outer layer for measurements and simulations for checking data consistency.

In general, there is a good agreement between simulations and the measured data, if one omits rare events like high multiplicity hits with cosmic rays. When displaying ratios between measurements and simulations for cosmic rays, the prediction holds quite well for the low multiplicity events and creates deviations for high multiplicity events. There is a very good consistency between inner and outer hodoscope of measured data over all multiplicity bins. Comparison with simulations show significant deviations due to boundary effects from the emitting surface of the CRY generator (compare chapter 4).

Regarding $\bar{p}$ annihilations, there is a very good agreement with the simulated multiplicity distribution for both the inner and outer hodoscope. The data are consistent between both detector layers and with simulations. The histogram bin containing multiplicity one is enhanced in both hodoscopes with the outer hodoscope showing a higher enhancement than the inner one. This effect is explained by random coincidences from upstream annihilations. The number of antiprotons annihilating on the beam pipe walls is orders of magnitude higher than the number actually reaching the detector. When comparing the good agreement with simulations for multiplicity one in cosmic rays, one can conclude that this multiplicity enhancement emerges from the $\bar{p}$ beam lost during extraction.
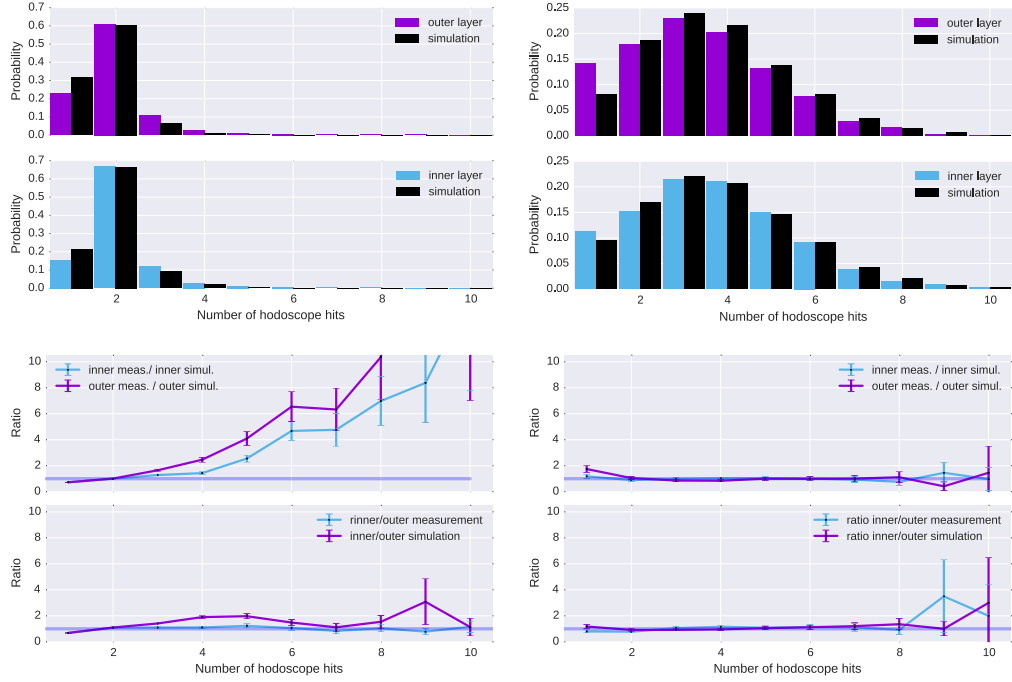
(a) data from cosmic rays   (b) antiproton annihilation data

Figure 6.5.: Comparison of detector hit multiplicity distribution of cosmic data (**a**) and pbar annihilations (**b**). All data are normalised as PMFs. **top:** direct comparison of inner (blue) and outer (violet) hodoscope with Genat 4 simulations using the SMI $\overline{\text{p}}$ annihilation model. **bottom:** ratios of inner hodoscope and simulation (blue) and outer hodoscope with simulations (violet) - upper panel. Ratios of inner and outer hodoscope data (blue) and ratios for simulations (violet) - lower panel. In the legend, "meas." is short for measurement, and simulation is shortened to "simul.".

6.4. Antihydrogen identification

The canonical way of identifying antihydrogen annihilations, within a high level of background signal, which was used in Kuroda et al. [33], is by applying cuts on the energy deposition in the central detector, and on the multiplicities in the hodoscope. Whilst this approach clearly works well, it does have some major drawbacks. For one, not all available information is utilised, rather only a small subset. At the same time there is no gauge to really differentiate an identified event from the background.

In order to improve the existing method, data driven models are being built. Starting from the simple cut method, we assume that all input variables are independent:

$$\mathcal{L}(D|x_0, \dots x_n) = \prod_{i=0}^{n} \mathcal{L}(D|x_n), \tag{6.1}$$

with the probability, or likelihood ($\mathcal{L}$) of data (D) realised with the independent model variables (x_i). Clearly, this simplistic approach will not provide the best possible results. Therefore, we can generalise it by allowing correlations between the model variables. When building a data driven model, there is one catch when relaxing the independence condition. The phase space explodes and huge amounts of data are required to generate a working multivariate model. While abundant data from cosmic rays are available, only a very limited set of antiproton events has been recorded with the detector so far. This leads to a hybrid solution between a fully dependent multivariate model and the combinations of independent univariate statistical quantities.

The trade-off model, with the currently available antiproton data, includes the following quantities; the type of the distribution is written in brackets:

- angular distribution in the inner hodoscope (univariate discrete)

- angular distribution in the outer hodoscope (univariate discrete)

- joint probability distribution for multiplicities in inner and outer hodoscope (bivariate discrete)

- energy deposition in the central BGO detector (univariate continuous)

- joint probability distribution for minimum angle difference in inner and outer hodoscope if more than one bar is hit (bivariate discrete)

Table 6.2.: Bayes factor with corresponding "Bayesian p-value" and interpretation.

$\mathcal{K}$	p	interpretation
< 1	0 to 0.5	negative result
1 to $\sqrt{10}$	0.5 to 0.76	weak
$\sqrt{10}$ to 10	0.76 to 0.91	substantial
10 to $\sqrt{1000}$	0.91 to 0.97	strong
$\sqrt{1000}$ to 100	0.97 to 0.99	very strong
> 100	> 0.99	decisive

Finally, the model is built by creating a histogram of the data for discrete random variables, and by calculating a kernel density estimate for the BGO energy deposit. The background model is built from the data between cusp mixing cycles; the antiproton model is built from a dedicated experiment to collect annihilations from slow extracted antiprotons.

Selecting the appropriate model, and therefore determining if an event is an antiproton/antihydrogen annihilation or background, is done by calculating a Bayes factor ($\mathcal{K}$) for each event, which is the ratio of the likelihoods.

$$\mathcal{K} = \frac{\mathcal{L}_{\text{antiproton}}}{\mathcal{L}_{\text{background}}} \tag{6.2}$$

This Bayes factor is now interpreted according to Jeffreys [80] using Table 6.2. In this table a "Bayesian p-value" is indicated, however please note that this is only for rough guidance and should not be used for data interpretation.

Together with the Bayes factor analysis, and the data driven model preparation, a robust, versatile, and easily expandable framework for identifying antiproton or antihydrogen annihilations has been developed. Furthermore, this method is able to quantify the degree of "belief" in an event to be an annihilation or background.

In Table 6.3 the scores for falsely rejecting antiproton annihilations and for correctly rejecting cosmic events are summarised. The scores were calculated by dividing the available data sets into two parts: the first part was used to prepare the likelihood models, and the second part was used to test the models and calculate their respective scores. In Figure 6.6 two events with their Bayes factor are displayed as examples. The left plot shows a decisive annihilation and the right plot shows an event with a developing shower

Table 6.3.: Probabilities for falsely rejecting antiproton annihilations and cosmic rejection probabilities.

$\mathcal{K}$	$\overline{p}$ rejection [%]	cosmic rejection [%]
$< \sqrt{10}$	25.4	90.7
< 10	38.3	95.5
$< \sqrt{1000}$	53.2	99.0
< 100	68.0	99.2
> 100	81.2	99.9
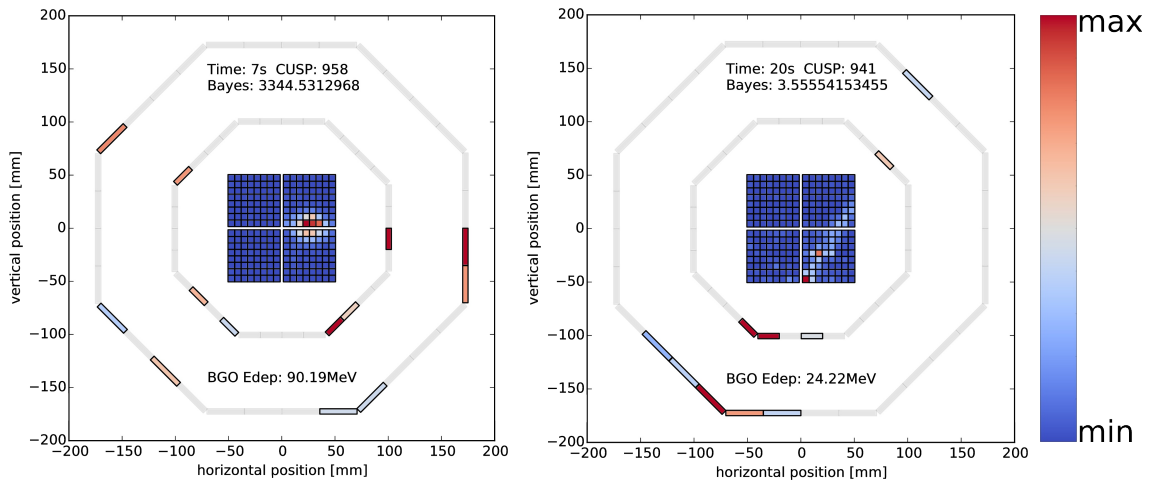
Figure 6.6.: **Left**: Annihilation event that occurred seven seconds after the start of a mixing cycle in run number 958, with a Bayes factor that is considered decisive. The energy deposit in the central BGO detector is 90 MeV. **Right**: A background event with a developing shower. The particle trace is visible inside of the BGO disc, resulting in an energy deposit of 24 MeV. The event is already classified as substantial.

that could be falsely classified as annihilation. Due to the contamination in the histogram bin with multiplicity one, a hard cut was applied in order to only allow multiplicities greater than one (compare Figure 6.5).

6.5. Bayesian estimation of signal above background

When comparing the number of detected antihydrogen annihilations with the measured background from annihilations in the AD ring, the surrounding machines, and from cosmic rays, special care has to be taken to produce valid statistical results. The low number of background counts and signal counts requires sophisticated methods for proper error propagation and difference of means estimation.

In order to calculate the mean signal above background, a new Bayesian method based on Kruschke [81] was developed. To my knowledge this method of non-parametric testing in a Bayesian framework is new in physics. Inside of the cusp trap, antihydrogen is produced in a Poisson process by combination, or "mixing", of antiprotons and positrons. Only a small fraction of antihydrogen produced reaches the detector. It follows that a Poisson distribution can be used as a Likelihood function in the analysis. The same argument holds for background signal, as only a small fraction of produced background particles actually reach the detector. The main difference to the testing scheme described in Kruschke [81] is the adaption to counting experiments. This is done by exchanging the "t-distribution" in the original method by the Poisson distribution following the argument presented above.

$$\mathcal{P}(\lambda|D) \propto \mathcal{P}(D|\lambda)\mathcal{P}(\lambda). \tag{6.3}$$

Equation (6.3) is proportional to Bayes' rule. The "prior" information is denoted by $\mathcal{P}(\lambda)$ and $\mathcal{P}(D|\lambda)$ representing the Likelihood function. The parameter λ of the Poisson distribution describes the central location, and D represents the measured data. In the case of a Poisson distribution, it is commonly known that, the expectation value for a random variable is $E(D) = \lambda$ and also the variance is $\mathrm{var}(D) = \lambda$. The necessary normalisation constant for Bayes' rule is usually hard to compute. From the probability mass function of the Poisson distribution it can be easily computed that the Fisher information is $\mathcal{I} = \lambda^{-1}$.

Assuming we have no prior information, a sensible choice is using Jeffreys' prior [82] which is proportional to $\sqrt{\det(\mathcal{I})}$. In the univariate case of a Poisson distribution this yields:

$$\mathcal{P}(\lambda) \propto \frac{1}{\sqrt{\lambda}}. \tag{6.4}$$

In the following analysis, the results were validated against a uniform prior (highly informative and biased towards high values of λ) and a Gaussian prior with μ chosen as the arithmetic mean of the frequentist expectation values. The parameter σ was chosen to be five times the standard sample error (a Gauß distribution is sensible due to the central limit theorem). Together, both checks allow to test the stability of the estimation against the choice of the prior.

The posterior distribution (the probability of the model parameter λ under observation of the experimental data) is approximated by a markov-chain-monte-carlo method with an affine invariant ensemble sampler [83] implemented in the emcee package [84]. From evaluating the annihilation rate inside of the cusp trap [33], it is known that antihydrogen is produced in a 20 s time window. For comparison with the antihydrogen counts the continuous background measurements are binned by 20 s.

The markov-chain-monte-carlo (MCMC) algorithm is used to calculate Markov-Chains for the posterior distribution of λ. In the following, the Markov-Chain for background data are denoted as $\mathcal{P}_b$ and for the counts that can contain antihydrogen events as $\mathcal{P}_{\bar{H}+b}$. Each value in both chains is by itself a valid element of the respective posterior distribution. Therefore, we can directly calculate:

$$\mathcal{P}_{\bar{H}} = \mathcal{P}_{\bar{H}+b} - \mathcal{P}_b. \tag{6.5}$$

After this subtraction, $\mathcal{P}_{\bar{H}}$ is now a new Markov-Chain representing the distribution of the expected difference from background. In other words, the distribution of the mean antihydrogen production in 20 s after background subtraction. Additionally, to the direct difference of means, we can calculate the effect size for two groups with different means and variances (Cohens d [85])[3] by utilising that $\text{var}(D) = \lambda$ for Poisson distributed variables. It follows, that the distribution of the effect size can be expressed as a Markov-Chain:

$$\mathcal{P}_d = \frac{\mathcal{P}_{\bar{H}}}{\sqrt{0.5(\mathcal{P}_{\bar{H}+b} + \mathcal{P}_b)}}. \tag{6.6}$$

---

[3]The cohen d effect size is generally defined as $\frac{\bar{x}_1 - \bar{x}_2}{0.5(\text{var}(x_1)+\text{var}(x_2))}$ with the mean ($\bar{x}$) and variances (var(x)) of the two samples x_1 and x_2.

In general the strength of an effect is called "large" if the effect size is > 0.8, "medium" if $d > 0.5$ and "small" if $d > 0.2$ [85]. A smaller effect size means more measurements are required to detect the difference when repeating an experiment. The interpretation stated above allows the definition of a region of practical equivalence (ROPE) of $|d| < 0.2$. If the 0.95 highest posterior density interval (HDI) overlaps with the ROPE the effect is marginal [81].

6.6. Results

In the following section the results will be reported with their arithmetic mean for the expected number of events and the mode for the effect size. All errors are reported as 0.95 HDIs. In addition the probability of the signal being above background will be reported. Tables containing the number of counts per run and 20 seconds measurement time with their respective settings for positron and antiproton stacks that were used for this analysis are available in Appendix B tables B.3, B.4 and B.5.

Following the arguments in section 6.5 a Markov-Chain for the location parameter λ is generated for measurements during mixing and for background measurements. As described in equation (6.5) the two chains are pairwise subtracted to compute the signal distribution above background. It should be noted that background correlated with the measurement is not subtracted as background measurements during the mixing process are currently not available. At the same time, as a consequence of the MCMC sampling, an almost perfect error propagation is achieved. In Figure 6.7 two histograms for a decisive Bayes factor are displayed. The left side shows the λ distribution of antihydrogen counts after background subtraction with a 95% HDI. The plot on the right side of Figure 6.7 shows the expected difference between a measurement time of 40 and 20 seconds after the start of mixing and after subtracting the expected background in both cases. It can be immediately seen that the signal above background in the first 20 seconds is highly significant, as the mean and the 95% HDI are clearly separate from the zero line. In contrast, the difference between 40 seconds and 20 seconds after mixing is not significant. This indicates that almost no antihydrogen reaches the detector after the first 20 seconds.

A full summary of the expected signal above background is available in Table 6.4 and in Figure 6.8. The table contains the difference in λ and the corresponding effect size both
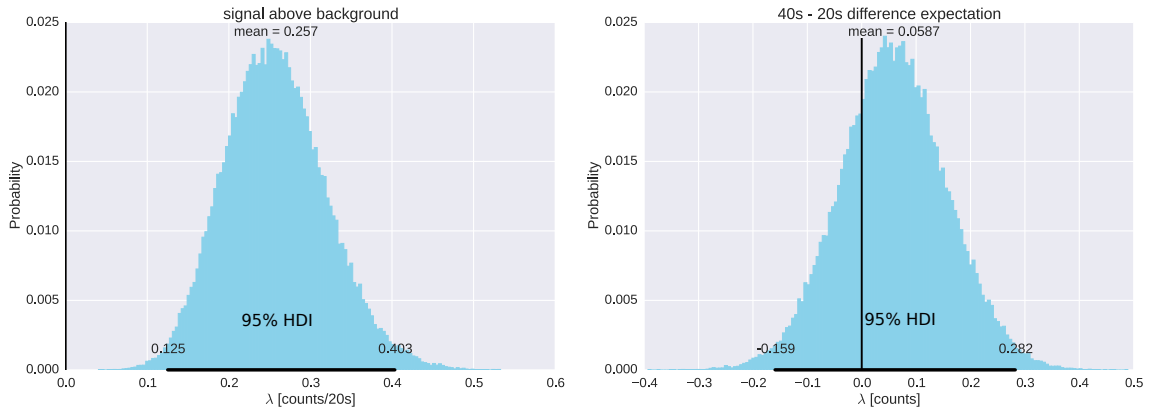
Figure 6.7.: Histogram of two Markov-Chains, the bin size has been calculated via the Freedman–Diaconis rule [86]. Error intervals are given as 95% HDIs. They are represented as black horizontal bar. In the **left** histogram the distribution of $\lambda_{\bar{H}}$ after background subtraction is shown. The **right** histogram displays the $\Delta\lambda$ of 40 and 20 seconds of measurement time after mixing and after background subtraction. The black vertical bar marks the zero line.

with 95% HDI errors. The one-sided probabilities for $\Delta\lambda$ being below zero ($\mathcal{P}(\Delta\lambda < 0)$) and the effect size being above 0.2 ($\mathcal{P}(\text{EffSize} > 0.2)$) were calculated by computing a Gaussian KDE and numerically integrating over the respective range.

In Table 6.5 the ratios between data and background are summarised including error boundaries calculated from MCMC error propagation. The first column $\lambda_{\bar{H}+bg}/\lambda_{bg}$ shows that the ratio between signal and background over background increases with the Bayes factor, whilst at the same time the ratio between signal and background over signal decreases. This trends confirms the effectiveness of the Bayes factor particle identification described in section 6.4. The last column shows the increase of detected anihydrogen over expected background.

Up to this point, only the first 20 seconds after the start of the mixing cycles have been investigated. In Table 6.6 the differences between 40 seconds and 20 seconds of measurement time are reported. The difference is calculated in two steps: first the signal above background ($\lambda_{\bar{H}}$) is computed for 20 and 40 seconds. Then the expected background is subtracted according to equation (6.5). Finally the difference distribution is calculated again by pairwise subtraction of both Markov-Chains. The one-sided probabilities are directly calculated from the Markov-Chains. From the differences, between 20 s and

Table 6.4.: Showing the difference between measured data and background within a 20 seconds time window after the start of a cusp mixing cycle. $\lambda_{\bar{H}+bg}$ denotes the expectation value for data recorded during mixing and λ_{bg} represents background data. The asymmetric error intervals represent the 95% HDI and the $\mathcal{P}$ values indicate a one-sided probability.

Bayes factor	$\lambda_{\bar{H}+bg} - \lambda_{bg}$	$\mathcal{P}(\Delta\lambda < 0)$	Effect Size	$\mathcal{P}(\text{EffSize} > 0.2)$
weak	$0.670^{+0.293}_{-0.281}$	$< 1\text{e-}10$	$0.704^{+0.246}_{-0.286}$	> 0.999999
substantial	$0.537^{+0.248}_{-0.243}$	$< 1\text{e-}10$	$0.690^{+0.261}_{-0.274}$	> 0.99996
strong	$0.442^{+0.205}_{-0.201}$	$< 1\text{e-}10$	$0.661^{+0.240}_{-0.270}$	> 0.9998
very strong	$0.334^{+0.172}_{-0.153}$	$< 1\text{e-}9$	$0.605^{+0.241}_{-0.241}$	> 0.9998
decisive	$0.257^{+0.145}_{-0.130}$	$< 1\text{e-}9$	$0.563^{+0.237}_{-0.234}$	> 0.9995
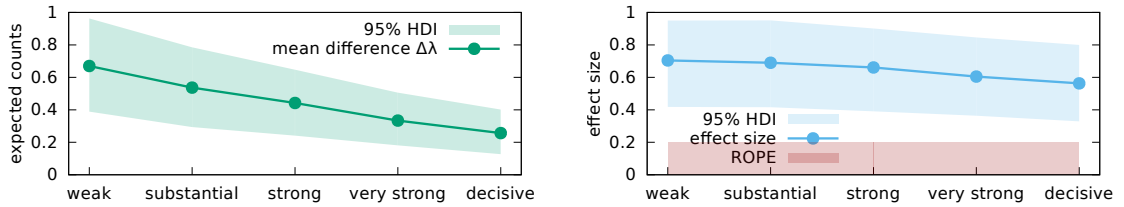
Figure 6.8.: Graphical representation of Table 6.4. The left plot shows the expected counts within the first 20 s during mixing **after background subtraction**. The 95 % HDI does not overlap with zero. It follows that the signal above the background level is significant. The graph on the right shows the effect size of the difference. Again the 95 % HDI does not overlap the ROPE. Therefore, we can conclude that the effect is not marginal but likely of medium strength.

Table 6.5.: Displaying ratios between data and background within a 20 seconds measurement window after the start of a cusp mixing cycle. $\lambda_{\bar{H}+bg}$ represents the measured data during mixing, λ_{bg} represents the measured background and $\lambda_{\bar{H}}$ is the expectation after background subtraction. The asymmetric error intervals represent the 95% HDI.

Bayes factor	$\lambda_{\bar{H}+bg}/\lambda_{bg}$	$\lambda_{\bar{H}+bg}/\lambda_{\bar{H}}$	$\lambda_{\bar{H}}/\lambda_{bg}$
weak	$2.042^{+0.714}_{-0.504}$	$1.834^{+0.787}_{-0.341}$	$1.042^{+0.715}_{-0.504}$
substantial	$2.268^{+0.933}_{-0.667}$	$1.694^{+0.713}_{-0.302}$	$1.268^{+0.933}_{-0.667}$
strong	$2.782^{+1.605}_{-0.977}$	$1.460^{+0.553}_{-0.214}$	$1.782^{+1.605}_{-0.977}$
very strong	$3.345^{+2.644}_{-1.399}$	$1.357^{+0.469}_{-0.197}$	$2.345^{+2.645}_{-0.399}$
decisive	$3.834^{+4.605}_{-1.902}$	$1.254^{+0.473}_{-0.158}$	$2.833^{+4.605}_{-1.902}$

40 s of measurement time with 95% HDIs, together with Figure 6.9, it is evident that the effect is marginal, and the difference is not significant. It can be concluded that most antihydrogen is produced within the first 20 seconds after the start of mixing.

A similar analysis of the first 5 seconds leads to the conclusion that the production of antihydrogen is evenly distributed in the first 20 seconds. In Table 6.7 the results are summarised with the expected mean difference between 5 and 20 seconds and its effect size. The third column shows the ratio between mean antihydrogen counts in 20 seconds and in 5 seconds reported by the mode of the distribution (the most probable value). Although the 95% HDI for the ratio is rather large, the mode is consistent with the expected factor of 4, which in turn leads to the conclusion mentioned above. The results are summarised in Figure 6.10.

For optimising the antihydrogen production efficiency, a comparison between sets of different production settings might be useful. In Table 6.8 the available data sets are separated into two groups. First two groups are defined depending on the effective number of antiprotons stacks in the cusp trap. It should be noted that other parameters, which were not considered during this analysis, vary inside the groups. One group containing all measurements that used less or equal to four stacks of antiprotons, and the other group with more than four stacks. Again, the λs after background subtraction are calculated followed by a subtraction for the two groups.

Table 6.6.: Comparison between expected counts in 40 and 20 seconds of mixing time. The asymmetric error intervals represent the 95% HDI.

Bayes factor	$\lambda_{\bar{H}(40s)} - \lambda_{\bar{H}(20s)}$	$\mathcal{P}(\Delta\lambda > 0)$	Effect Size	$\mathcal{P}(\text{EffSize} > 0.2)$
weak	$0.400^{+0.466}_{-0.481}$	> 0.971	$0.442^{+0.473}_{-0.520}$	> 0.848
substantial	$0.300^{+0.400}_{-0.405}$	> 0.952	$0.364^{+0.463}_{-0.493}$	> 0.777
strong	$0.218^{+0.319}_{-0.322}$	> 0.935	$0.312^{+0.398}_{-0.451}$	> 0.691
very strong	$0.127^{+0.263}_{-0.265}$	> 0.862	$0.194^{+0.397}_{-0.422}$	> 0.503
decisive	$0.058^{+0.224}_{-0.218}$	> 0.727	$0.082^{+0.427}_{-0.386}$	> 0.307
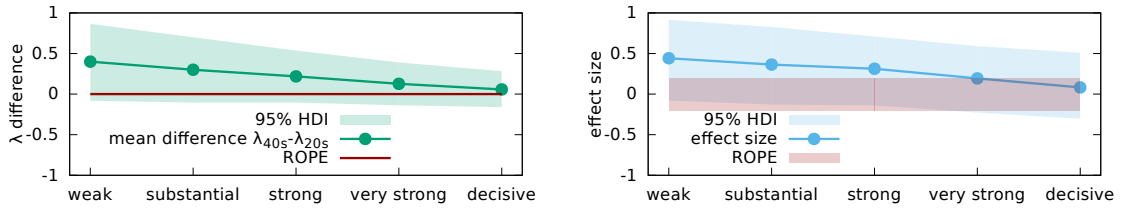
Figure 6.9.: Data from Table 6.6 is summarised. The graphs show the mean difference between the expected counts in 40 s and 20 s of the cusp mixing. The plot on the right shows that the difference is not significant at a 95 % HDI level. Furthermore, the mean of the difference decreases with higher Bayes factor. This indicates that a time window of 20 s the favourable choice. The right side graph shows that effect size, even if the difference would be significant the effect size is marginal.
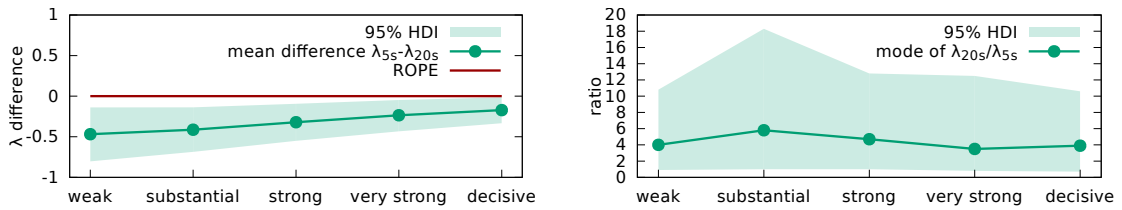
Figure 6.10.: **left:** mean difference between the expected counts in 5 seconds and 20 seconds of the mixing process. **right:** ratio between 20 seconds and 5 seconds of the cusp mixing.

Table 6.7.: Comparison between expected counts in 5 and 20 seconds of mixing time. The asymmetric error intervals represent the 95% HDI.

Bayes factor	$\lambda_{\bar{H}(5s)} - \lambda_{\bar{H}(20s)}$	Effect Size	$\lambda_{\bar{H}(20s)}/\lambda_{\bar{H}(20s)}$
weak	$-0.468^{+0.330}_{-0.335}$	$+0.743^{+0.407}_{-0.500}$	$4.0^{+6.8}_{-3.1}$
substantial	$-0.413^{+0.276}_{-0.273}$	$+0.742^{+0.371}_{-0.454}$	$5.8^{+12.5}_{-4.8}$
strong	$-0.321^{+0.227}_{-0.229}$	$+0.613^{+0.348}_{-0.405}$	$4.7^{+8.1}_{-3.7}$
very strong	$-0.235^{+0.188}_{-0.198}$	$+0.513^{+0.339}_{-0.392}$	$3.5^{+9.0}_{-2.7}$
decisive	$-0.172^{+0.157}_{-0.161}$	$+0.418^{+0.327}_{-0.355}$	$3.9^{+6.7}_{-3.2}$

The amount of available data is not sufficient to show significant differences. An observer might anticipate a tendency regarding weak, substantial, strong and very strong event candidates towards higher numbers if increasing the number of antiprotons. However, the difference within the frame of the available data is not significant with a 0.95 HDI. In addition, it should be considered that larger stacks of antiprotons or positrons add more deadtime in between measurements.

When dividing the data sets by their number of positrons, a similar study can be performed. The data are separated into one group with fewer than 15 positron stacks, and a second group with more or equal to 15 stacks. Again, an observer with a positive attitude might see a tendency towards more produced antihydrogen when using more positrons in the cusp trap. However, there is not enough data for a statistically significant result. The results for both studies are recorded in Table 6.8 and in Figure 6.11.

Table 6.8.: Difference between expected counts for less or equal four $\bar{\text{p}}$ stacks and more than four $\bar{\text{p}}$ stacks and difference between expected counts for less than 15 and more or equal 15 positron stacks. The asymmetric error intervals represent the 95% HDI and the $\mathcal{P}$ values indicate a one-sided probability.

Bayes factor	$\lambda_{\bar{\text{H}}(<5\bar{\text{p}})} - \lambda_{\bar{\text{H}}(\geq 5\bar{\text{p}})}$	$\mathcal{P}(\Delta\lambda_{\bar{\text{p}}}>0)$	$\lambda_{\bar{\text{H}}(<15\text{e}^+)} - \lambda_{\bar{\text{H}}(\geq 15\text{e}^+)}$	$\mathcal{P}(\Delta\lambda_{\text{e}^+}>0)$
weak	$-0.389^{+0.638}_{-0.593}$	> 0.083	$-0.386^{+0.534}_{-0.549}$	> 0.056
substantial	$-0.490^{+0.521}_{-0.454}$	> 0.018	$-0.344^{+0.461}_{-0.468}$	> 0.047
strong	$-0.290^{+0.448}_{-0.401}$	> 0.070	$-0.354^{+0.388}_{-0.386}$	> 0.023
very strong	$-0.232^{+0.367}_{-0.322}$	> 0.071	$-0.266^{+0.316}_{-0.323}$	> 0.029
decisive	$-0.062^{+0.350}_{-0.300}$	> 0.305	$-0.102^{+0.278}_{-0.270}$	> 0.193
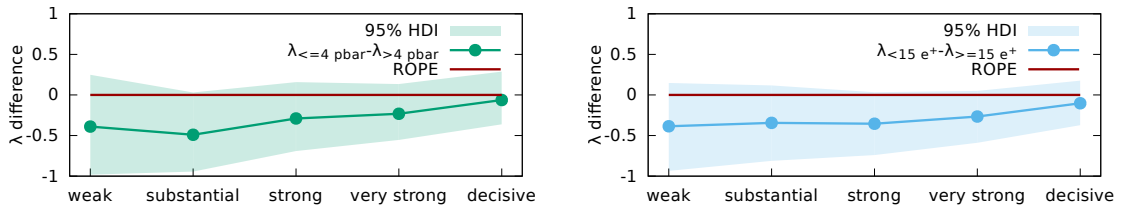
Figure 6.11.: The left graph shows the difference of detected antihydrogen atoms when comparing less than five stacks of antiprotons and more than and including five stacks in the cusp trap. In the 95 % HDI there is no significant difference but a slight tendency. The right graph shows the comparison between smaller 15 and more/equal 15 position stacks in the trap. Again no significant difference can be observed with the available data only a trend.

7. Summary and Outlook

During the course of this thesis, a detector for antihydrogen was developed and successfully tested during beamtime. Furthermore, newly designed readout electronics, the "IFES" modules, were put into operation and their performance was thoroughly analysed. For detector operation a DAQ tool chain was installed, which started with the design of an intelligent trigger system. This was made made possible by a careful design of the IFES modules.

The trigger system was synchronised with veto signals from the accelerator, and a scheme for data synchronisation during readout of the detector was implemented. To achieve the synchronisation, MIDAS drivers for all hardware components and a MIDAS front-end for interrupt controlled detector readout were developed.

The recorded raw data were analysed by means of a novel, versatile, and plugin-based library for waveform analysis. This new library is a general framework for analysing all kinds of waveforms and can be used in various experiments of small to medium sizes.

Followed by the analysis of the waveforms, a probabilistic Bayesian model was developed to identify antiproton and antihydrogen annihilations in the detector from measured background by means of a data driven analysis. This approach allows one to quantify the "belief" (in a Bayesian sense) in single events being annihilations or for them to originate from background.

A fully Bayesian statistical analysis and testing program was implemented with a novel way of statistical testing with perfect error propagation by using Markov-Chain-Monte-Carlo methods. Furthermore, through this analysis the significance of a signal being present during the mixing process above the background level could be shown. In addition, the insight into antihydrogen production was deepened by comparing the mean production rate of three time intervals after the beginning of the antihydrogen production.

Finally, all results are based on sophisticated simulation techniques and numerical calculations that allow a deeper insight into the inner workings of the beamline, the polarisation effects of the magnets, and the final line shape of the ground state hyperfine transition.

7.1. Outlook

One of the most critical points in detector operation is its discrimination efficiency against cosmic and machine induced background. For example, the discrimination efficiency can be improved by optimising the detector timing performance. An improved timing allows the direction of tracks to be detected. Hence, it would be possible to discriminate by checking if a track passes through the whole detector or originates in the centre. This optimisation is actively being worked on and an improved version of the detector will be put into operation during the 2016 beamtime.

A limitation for recording antiproton annihilations in test experiments is the low acceptable trigger rate. Due to incompatibilities between some of the DAQ modules, the data taking rate is limited to ≈ 50 Hz. This could be overcome by utilising the internal buffer system of the waveform digitisers while maintaining synchronisation with the incompatible modules. The DAQ optimisation will be performed during a future master's thesis.

High accuracy simulations of the spectroscopy beamline are essential for deducing information like state and velocity distribution from resonance scans and detector count rates in future measurements. Currently, a code is available to include higher Rydberg states in dependence of the magnetic fields in the simulation. However, a full simulation would also include the Stark effect as well as Stark mixing. This is required to assess the impact of electric fields present in the beamline on the state distributions of produced antihydrogen.

Finally, if more antiproton data become available the discrimination algorithm can be updated to incorporate more correlated information by relaxing the independence conditions even further. In addition, an improved tracking and vertex reconstruction algorithm is under development that would further increase the background discrimination efficiency.

A. Detector tables and figures

A.1. Detector electronics

Table A.1.: Front-end modules

Name	Description	Signals
Arduino Yún	slow control master	Ethernet, SPI via LVDS
CP80190	shaping amplifier, ADC	analogue in/out, data out
H8500	multi anode PMT	HV, analogue out
LC632A	discriminator	analogue in, digital out
LC428F	linear fan IN/OUT	analogue in/out
IFES	power supply, amplifier discriminator	SPI, analogue out LVDS out

Table A.2.: VME modules

Name	Description	Signals
CP80057	readout module	digital in/out
SIS3100	VME master	digital in/out
SIS3820	32 channel scalar	digital in
V1492	FPGA board	digital in
V1742	waveform digitiser 5 GS, 1024$\times$200 ps	analogue in

A.2. Detector wiring tables

Table A.3.: Inner layer upstream wiring

Arduino channel	Hodoscope channel	Panel colour	Wire colour
0	ILU 1	blue	red
1	ILU 0	blue	brown
2	ILU 3	blue	yellow
3	ILU 2	blue	orange
4	ILU 5	violet	blue
5	ILU 4	violet	green
6	ILU 7	violet	grey
7	ILU 6	violet	purple
8	ILU 9	pink	white
9	ILU 8	pink	black
10	ILU 11	pink	red
11	ILU 10	pink	brown
12	ILU 13	red	yellow
13	ILU 12	red	orange
14	ILU 15	red	blue
15	ILU 14	red	green
16	ILU 17	orange	red
17	ILU 16	orange	brown
18	ILU 19	orange	yellow
19	ILU 18	orange	orange
20	ILU 21	yellow	blue
21	ILU 20	yellow	green
22	ILU 23	yellow	grey
23	ILU 22	yellow	purple
24	ILU 25	green	black
25	ILU 24	green	white
26	ILU 27	green	red
27	ILU 26	green	brown
28	ILU 29	dark green	yellow
29	ILU 28	dark green	orange
30	ILU 31	dark green	blue
31	ILU 30	dark green	green

Table A.4.: Inner layer downstream wiring

Arduino channel	Hodoscope channel	Panel colour	Wire colour
96	ILD 20	yellow	green
97	ILD 21	yellow	blue
98	ILD 18	orange	orange
99	ILD 19	orange	yellow
100	ILD 16	orange	brown
101	ILD 17	orange	red
102	ILD 14	red	green
103	ILD 15	red	blue
104	ILD 12	red	orange
105	ILD 13	red	yellow
106	ILD 10	pink	brown
107	ILD 11	pink	red
108	ILD 8	pink	white
109	ILD 9	pink	black
110	ILD 6	violet	purple
111	ILD 7	violet	grey
112	ILD 4	violet	green
113	ILD 5	violet	blue
114	ILD 2	blue	orange
115	ILD 3	blue	yellow
116	ILD 0	blue	brown
117	ILD 1	blue	red
118	ILD 30	dark green	green
119	ILD 31	dark green	blue
120	ILD 28	dark green	orange
121	ILD 29	dark green	yellow
122	ILD 26	green	brown
123	ILD 27	green	red
124	ILD 24	green	white
125	ILD 25	green	black
126	ILD 22	yellow	purple
127	ILD 23	yellow	grey

Table A.5.: Outer layer upstream wiring

Arduino channel	Hodoscope channel	Panel colour	Wire colour
32	OLU 30	dark green	green
33	OLU 31	dark green	blue
34	OLU 28	dark green	orange
35	OLU 29	dark green	yellow
36	OLU 26	green	brown
37	OLU 27	green	red
38	OLU 24	green	white
39	OLU 25	green	black
40	OLU 22	yellow	purple
41	OLU 23	yellow	grey
42	OLU 20	yellow	green
43	OLU 21	yellow	blue
44	OLU 18	orange	orange
45	OLU 19	orange	yellow
46	OLU 16	orange	brown
47	OLU 17	orange	red
48	OLU 14	red	green
49	OLU 15	red	blue
50	OLU 12	red	orange
51	OLU 13	red	yellow
52	OLU 10	pink	brown
53	OLU 11	pink	red
54	OLU 8	pink	white
55	OLU 9	pink	black
56	OLU 6	violet	purple
57	OLU 7	violet	grey
58	OLU 4	violet	green
59	OLU 5	violet	blue
60	OLU 2	blue	orange
61	OLU 3	blue	yellow
62	OLU 0	blue	brown
63	OLU 1	blue	red

Table A.6.: Outer layer downstream wiring

Arduino channel	Hodoscope channel	Panel colour	Wire colour
64	OLD 1	blue	red
65	OLD 0	blue	brown
66	OLD 3	blue	yellow
67	OLD 2	blue	orange
68	OLD 5	violet	blue
69	OLD 4	violet	green
70	OLD 7	violet	grey
71	OLD 6	violet	purple
72	OLD 9	pink	black
73	OLD 8	pink	white
74	OLD 11	pink	red
75	OLD 10	pink	brown
76	OLD 13	red	yellow
77	OLD 12	red	orange
78	OLD 15	red	blue
79	OLD 14	red	green
80	OLD 17	orange	red
81	OLD 16	orange	brown
82	OLD 19	orange	yellow
83	OLD 18	orange	orange
84	OLD 21	yellow	blue
85	OLD 20	yellow	green
86	OLD 23	yellow	grey
87	OLD 22	yellow	purple
88	OLD 25	green	black
89	OLD 24	green	white
90	OLD 27	green	red
91	OLD 26	green	brown
92	OLD 29	dark green	yellow
93	OLD 28	dark green	orange
94	OLD 31	dark green	blue
95	OLD 30	dark green	green

A.3. Trigger timing
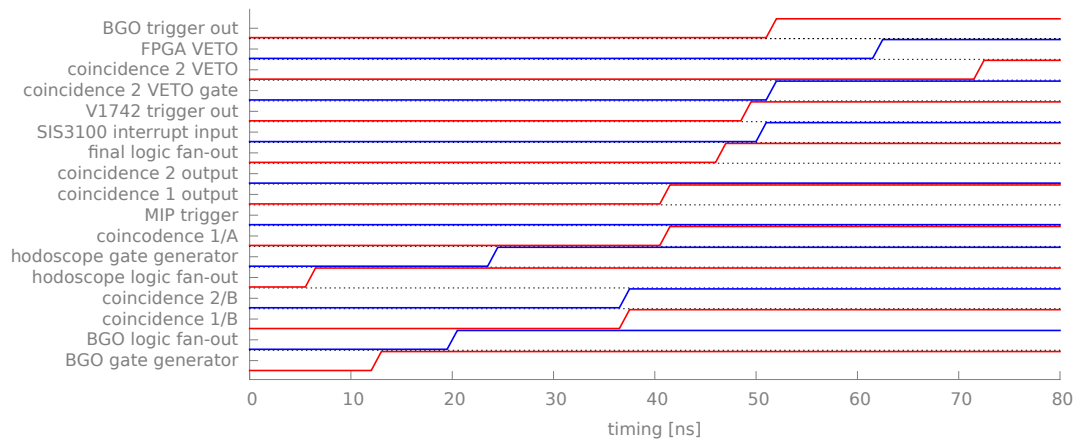
Figure A.1.: Timing of the Hbar trigger.
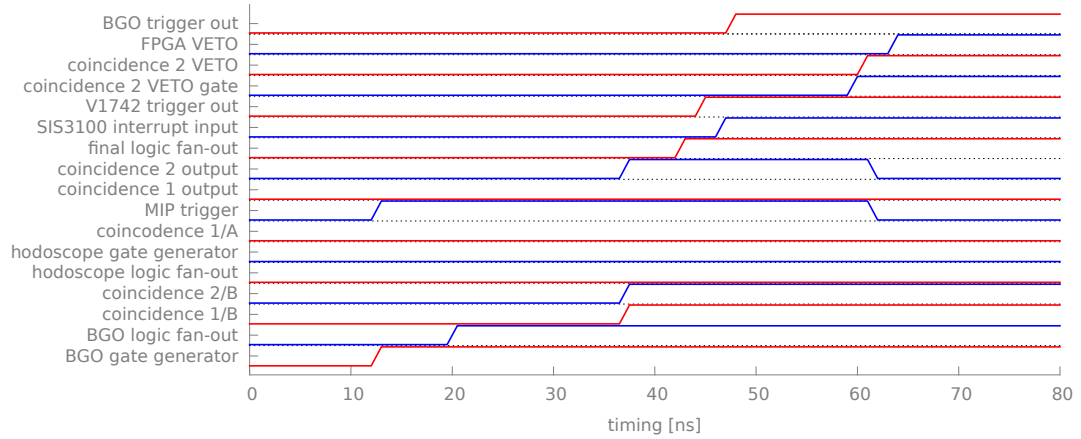
Figure A.2.: Timing of the MIP calibration trigger.
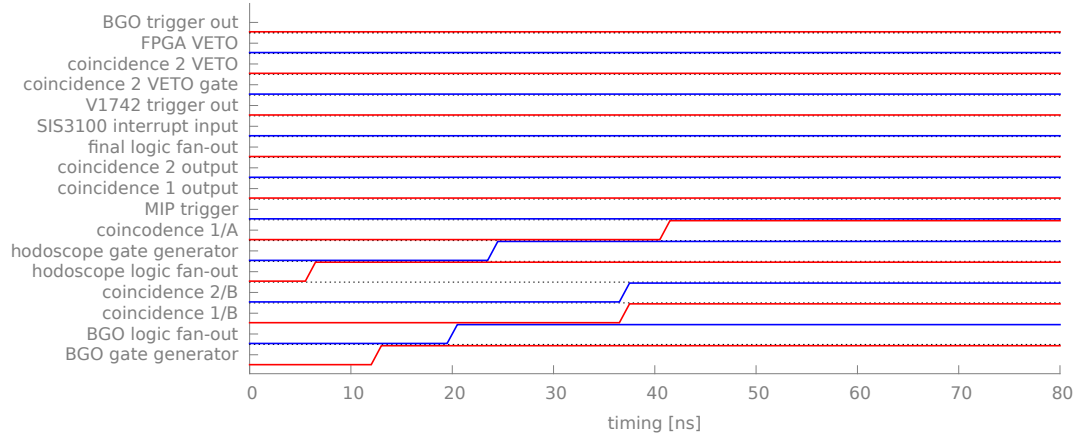
Figure A.3.: Timing of the AD veto signal.

B. Data analysis tables

Table B.1.: TTree structure of pre-analysed data

TTree name	Leaf name	String	Description
ClockEventTree	BGODataPortA	[64]/D	12 bit ADC bins
	BGODataPortB	[64]/D	
	BGODataPortC	[64]/D	
	BGODataPortD	[64]/D	
	BGOHeaderPortA	[2]/i	raw header data
	BGOHeaderPortB	[2]/i	
	BGOHeaderPortC	[2]/i	
	BGOHeaderPortD	[2]/i	
	BGORawDataPortA	[32]/i	raw 12 bit ADC data
	BGORawDataPortB	[32]/i	
	BGORawDataPortC	[32]/i	
	BGORawDataPortD	[32]/i	
	BGOTotalChargePre	[4]/D	charge integral w/o calibration
	BGOTimeStamaps	[2]/i	internal raw timestamp
HbarEventTree	all from ClockEventTree		
	all from ManualEventTree		

Table B.2.: TTree structure of pre-analysed data, continued from Table B.1

TTree name	Leaf name	String	Description
ScalarDataTree	Timestamp	/D	scalar timestamp
	ScalarData	[32]/D	scalar data
ManualEventTree	LEtimeStampsInnerLayerUpstream	[32]/D	
	LEtimeStampsInnerLayerDownstream	[32]/D	
	LEtimeStampsOuterLayerUpstream	[32]/D	LE timestamps [ns]
	LEtimeStampsOuterLayerDownstream	[32]/D	
	LEtimeStampsSpare	[32]/D	
	LEToTInnerLayerUpstream	[32]/D	
	LEToTInnerLayerDownstream	[32]/D	
	LEToTOuterLayerUpstream	[32]/D	LE ToT [ns]
	LEToTOuterLayerDownstream	[32]/D	
	LEToTSpare	[32]/D	
	CFtimeStampsInnerLayerUpstream	[32]/D	
	CFtimeStampsInnerLayerDownstream	[32]/D	
	CFtimeStampsOuterLayerUpstream	[32]/D	CF timestamps [ns]
	CFtimeStampsOuterLayerDownstream	[32]/D	
	CFtimeStampsSpare	[32]/D	
	ChargeInnerLayerUpstream	[32]/D	
	ChargeInnerLayerDownstream	[32]/D	
	ChargeOuterLayerUpstream	[32]/D	charge [204.8e^9 Vs]
	ChargeOuterLayerDownstream	[32]/D	
	ChargeSpare	[32]/D	
	AmplitudeInnerLayerUpstream	[32]/D	
	AmplitudeInnerLayerDownstream	[32]/D	
	AmplitudeOuterLayerUpstream	[32]/D	Amplitude [V]
	AmplitudeOuterLayerDownstream	[32]/D	
	AmplitudeSpare	[32]/D	
	InnerLayerUpstreamDRS4Temp	[32]/D	
	InnerLayerDownstreamDRS4Temp	[32]/D	
	OuterLayerUpstreamDRS4Temp	[32]/D	temperature [°C]
	OuterLayerDownstreamDRS4Temp	[32]/D	
	SpareDRS4Temp	[32]/D	

Table B.3.: Table of measured antihydrogen counts with run numbers and trap settings. Table 1/3

Run number		Settings		Antihydrogen counts per Bayes factor				
CUSP	MIDAS	$\overline{p}$	e^+	$< \sqrt{10}$	< 10	$< \sqrt{1000}$	< 100	> 100
933	1198	7	11	2	1	1	0	0
934	1199	5	30	1	1	1	1	1
935	1200	5	30	3	2	1	1	1
936	1201	3	30	0	0	0	0	0
938	1202	6	30	2	0	0	0	0
939	1203	4	30	0	0	0	0	0
940	1204	6	30	1	1	0	0	0
941	1220	6	30	2	1	1	0	0
949	1223	3	11	1	1	1	1	1
950	1224	3	30	3	3	2	2	2
952	1227	3	30	1	1	0	0	0
955	1230	4	30	0	0	0	0	0
958	1234	4	30	2	2	2	2	2
959	1235	4	11	1	1	1	1	1
960	1236	4	11	1	1	1	1	1
961	1237	4	11	1	1	1	1	1
963	1238	4	30	1	1	1	0	0
972	1246	4	11	3	2	1	1	1
973	1247	4	11	3	3	3	3	3
975	1249	4	11	2	1	1	0	0
976	1252	3	11	1	1	1	1	0
977	1253	4	11	2	2	2	1	1
978	1254	2	11	3	1	1	1	1
979	1255	3	11	2	2	2	1	1
980	1256	3	33	2	0	0	0	0
981	1257	3	33	0	0	0	0	0
982	1258	3	12	3	3	3	3	1
984	1261	3	15	0	0	0	0	0
985	1262	3	15	1	1	1	0	0
986	1263	3	15	0	0	0	0	0
988	1265	4	30	3	2	0	0	0
995	1270	4	11	1	1	1	0	0
996	1271	4	11	2	1	1	1	1
997	1272	4	11	1	1	1	1	1

Table B.4.: Table of measured antihydrogen counts with run numbers and trap settings.
Table 2/3

Run number		Settings		Antihydrogen counts per Bayes factor				
CUSP	MIDAS	$\overline{p}$	e^+	$< \sqrt{10}$	< 10	$< \sqrt{1000}$	< 100	> 100
998	1273	4	11	2	2	1	0	0
999	1274	3	11	2	2	1	0	0
1000	1275	4	11	3	2	2	1	0
1001	1276	3	11	4	4	2	2	1
1002	1277	4	11	1	1	0	0	0
1003	1278	4	12	0	0	0	0	0
1004	1279	4	11	1	0	0	0	0
1005	1280	3	12	1	0	0	0	0
1006	1281	4	12	2	1	1	1	0
1007	1282	4	12	1	0	0	0	0
1008	1283	4	12	1	1	0	0	0
1009	1284	4	12	0	0	0	0	0
1010	1285	4	12	2	1	1	0	0
1011	1287	4	12	3	2	1	1	0
1012	1288	4	12	0	0	0	0	0
1014	1289	3	33	0	0	0	0	0
1015	1290	4	33	0	0	0	0	0
1025	1311	4	11	0	0	0	0	0
1026	1312	4	11	1	1	0	0	0
1027	1313	4	13	1	1	1	0	0
1028	1314	4	13	2	1	1	1	1
1029	1315	4	13	2	2	1	1	1
1030	1317	4	13	2	1	1	0	0
1031	1319	4	13	3	3	3	2	0
1033	1321	4	13	2	1	1	1	1
1034	1322	4	13	1	0	0	0	0
1035	1323	4	13	0	0	0	0	0
1036	1324	4	13	2	1	0	0	0
1037	1327	4	13	1	1	0	0	0
1038	1328	5	13	0	0	0	0	0
1039	1329	5	12	0	0	0	0	0
1040	1330	5	12	0	0	0	0	0
1042	1333	5	12	0	0	0	0	0

Table B.5.: Table of measured antihydrogen counts with run numbers and trap settings. Table 3/3

| Run number | | Settings | | Antihydrogen counts per Bayes factor | | | | |
CUSP	MIDAS	$\overline{p}$	e^+	$< \sqrt{10}$	< 10	$< \sqrt{1000}$	< 100	> 100
1043	1334	5	12	0	0	0	0	0
1044	1335	5	12	1	1	1	1	1
1053	1344	4	13	0	0	0	0	0
1054	1346	4	15	3	2	0	0	0
1056	1348	4	15	0	0	0	0	0
1057	1350	4	15	0	0	0	0	0
1058	1352	4	17	2	1	0	0	0
1059	1354	4	17	1	1	1	1	1
1060	1355	4	11	3	2	2	1	0
1061	1356	4	14	3	3	2	2	1
1062	1357	3	15	0	0	0	0	0
1063	1358	4	15	0	0	0	0	0
1064	1359	5	15	1	1	1	0	0
1065	1360	5	15	0	0	0	0	0
1066	1361	5	15	0	0	0	0	0
1067	1362	4	15	2	2	2	2	1
1068	1364	4	15	3	3	1	0	0
1069	1365	4	17	0	0	0	0	0
1070	1366	5	17	1	1	1	1	1
1071	1368	4	17	1	1	1	1	0
1072	1369	5	17	1	0	0	0	0
1073	1370	5	17	1	0	0	0	0
1074	1371	4	17	1	0	0	0	0
1075	1372	2	17	1	1	1	1	1
1076	1373	4	17	3	2	1	0	0
1077	1375	4	17	0	0	0	0	0
1078	1376	5	17	2	1	1	1	1

C. Acronyms

ADC   analogue to digital converter

AD   Antiproton Decelerator

APD   avalanche photo diode

ASACUSA Atomic Spectroscopy And Collisions Using Slow Antiprotons

BGO   bismuth germanate

CAD   computer-aided design

CERN   Organisation Européene pour la Recherche Nucléaire

CF   constant fraction

CLI   commandline interface

DAC   digital to analogue converter

DAQ   data acquisition

DRS4   Digital Ring Sampler 4

ECL   emitter coupled logic

ELOG   electronic logbook

FFT   fast fourier transform

FPGA field programmable gate array

FWHM full width at half maximum

HDI highest posterior density interval

HFS high field seekers

HV high voltage

ID identification number

IFES intelligent front-end electronics for silicon photo detectors

KDE kernel density estimate

LED light-emitting diode

LE leading edge

LFS low field seekers

LVDS low voltage differential signaling

MCMC markov-chain-monte-carlo

MIDAS Maximum Integrated Data Acquisition System

MIP minimum ionising particle

MUSASHI Monoenergetic Ultra Slow Antiproton Source for High-precision Investigations

NFS network file system

NIM nuclear instrumentation standard

PMF probability mass function

PMT   photo multiplier tube

PSB   Proton Synchrotron Booster

PS   Proton Synchrotron

RFQD   Radio Frequency Quadrupole Decelerator

ROPE   region of practical equivalence

RPC   remote procedure call

SME   standard model extension

SMI   Stefan Meyer Institute for subatomic physics

SPI   serial peripheral interface

SiPM   silicon photo multilpier

ToF   time-of-flight

ToT   time-over-threshold

VHDL   very high speed integrated circuit hardware description language

VME   Versa Module Europa

Bibliography

[1] Andrei D Sakharov. "Violation of $\mathcal{CP}$ invariance, $\mathcal{C}$ asymmetry, and baryon asymmetry of the universe". In: *Soviet Physics Uspekhi* 34.5 (1991), p. 392. URL: http://stacks.iop.org/0038-5670/34/i=5/a=A08.

[2] Carl D. Anderson. "The Positive Electron". In: *Phys. Rev.* 43 (6 Mar. 1933), pp. 491–494. DOI: 10.1103/PhysRev.43.491. URL: http://link.aps.org/doi/10.1103/PhysRev.43.491.

[3] P. A. M. Dirac. "The Quantum Theory of the Electron". In: *Proceedings of the Royal Society of London A: Mathematical, Physical and Engineering Sciences* 117.778 (1928), pp. 610–624. ISSN: 0950-1207. DOI: 10.1098/rspa.1928.0023. eprint: http://rspa.royalsocietypublishing.org/content/117/778/610.full.pdf. URL: http://rspa.royalsocietypublishing.org/content/117/778/610.

[4] Owen Chamberlain et al. "Observation of Antiprotons". In: *Phys. Rev.* 100 (3 Nov. 1955), pp. 947–950. DOI: 10.1103/PhysRev.100.947. URL: http://link.aps.org/doi/10.1103/PhysRev.100.947.

[5] G. Baur et al. "Production of antihydrogen". In: *Physics Letters B* 368.3 (1996), pp. 251–258. ISSN: 0370-2693. DOI: 10.1016/0370-2693(96)00005-6. URL: http://www.sciencedirect.com/science/article/pii/0370269396000056.

[6] G. Blanford et al. "Observation of Atomic Antihydrogen". In: *Phys. Rev. Lett.* 80 (14 Apr. 1998), pp. 3037–3040. DOI: 10.1103/PhysRevLett.80.3037. URL: http://link.aps.org/doi/10.1103/PhysRevLett.80.3037.

[7] M. Amoretti et al. "Production and detection of cold antihydrogen atoms". In: *Nature* 419.6906 (2002), pp. 456–459. DOI: 10.1038/nature01096.

[8] G. Gabrielse et al. "Driven Production of Cold Antihydrogen and the First Measured Distribution of Antihydrogen States". In: *Phys. Rev. Lett.* 89 (23 Nov. 2002), p. 233401. DOI: 10.1103/PhysRevLett.89.233401. URL: http://link.aps.org/doi/10.1103/PhysRevLett.89.233401.

[9]   T. Massam et al. "Experimental observation of antideuteron production". In: *Il Nuovo Cimento A* 63.1 (1965), pp. 10–14. DOI: 10.1007/BF02898804. URL: http://dx.doi.org/10.1007/BF02898804.

[10] Yu.M. Antipov et al. "Observation of antihelium-3". In: *Nuclear Physics B* 31.2 (1971), pp. 235–252. ISSN: 0550-3213. DOI: 10.1016/0550-3213(71)90228-8. URL: http://www.sciencedirect.com/science/article/pii/0550321371902288.

[11] Star Collaboration et al. "Observation of the antimatter helium-4 nucleus". In: *Nature* 473.7347 (2011), pp. 353–356. DOI: 10.1038/nature10079. URL: https://dx.doi.org/10.1038/nature10079.

[12] Nicole Martin and the ALICE Collaboration. "(Anti-)matter and hyper-matter production at the LHC with ALICE". In: *Journal of Physics: Conference Series* 455.1 (2013), p. 012007. URL: http://stacks.iop.org/1742-6596/455/i=1/a=012007.

[13] Karl Popper. *Logik der Forschung*. Springer-Verlag Wien, 1935. DOI: 10.1007/978-3-7091-4177-9. URL: https://dx.doi.org/10.1007/978-3-7091-4177-9.

[14] Thomas S Kuhn. *Structure of Scientific Revolutions*. 3rd ed. University of Chicago Press; 1996. ISBN: 978-0226458083.

[15] Robert Bluhm, V. Alan Kostelecký and Neil Russell. "*CPT* and Lorentz Tests in Hydrogen and Antihydrogen". In: *Phys. Rev. Lett.* 82 (11 Mar. 1999), pp. 2254–2257. DOI: 10.1103/PhysRevLett.82.2254. URL: http://link.aps.org/doi/10.1103/PhysRevLett.82.2254.

[16] Norman F Ramsey. "Experiments with trapped hydrogen atoms and neutrons". In: *Physica Scripta* 1995.T59 (1995), p. 323. URL: http://stacks.iop.org/1402-4896/1995/i=T59/a=044.

[17] V. Alan Kostelecký and Arnaldo J. Vargas. "Lorentz and $\mathcal{CPT}$ tests with hydrogen, antihydrogen, and related systems". In: *Phys. Rev. D* 92 (5 Sept. 2015), p. 056002. DOI: 10.1103/PhysRevD.92.056002. URL: http://link.aps.org/doi/10.1103/PhysRevD.92.056002.

[18] V. Alan Kostelecký and Neil Russell. "Data tables for Lorentz and $\mathcal{CPT}$ violation". In: *Rev. Mod. Phys.* 83 (1 Mar. 2011). newest version on arXiv, pp. 11–31. DOI: 10.1103/RevModPhys.83.11. URL: http://link.aps.org/doi/10.1103/RevModPhys.83.11.

[19] J. M. B. Kellogg, I. I. Rabi and J. R. Zacharias. "The Gyromagnetic Properties of the Hydrogens". In: *Phys. Rev.* 50 (5 Sept. 1936), pp. 472–481. DOI: 10.1103/PhysRev.50.472. URL: http://link.aps.org/doi/10.1103/PhysRev.50.472.

[20] Hans A. Bethe and Edwin E. Salpeter. *Quantum Mechanics of One- and Two-Electron Atoms*. Springer, 1957.

[21] Savely G. Karshenboim. "Precision physics of simple atoms: QED tests, nuclear structure and fundamental constants". In: *Physics Reports* 422.1–2 (2005), pp. 1–63. ISSN: 0370-1573. DOI: 10.1016/j.physrep.2005.08.008. URL: http://www.sciencedirect.com/science/article/pii/S0370157305003637.

[22] Norman F. Ramsey. "Experiments with separated oscillatory fields and hydrogen masers". In: *Rev. Mod. Phys.* 62 (3 July 1990), pp. 541–552. DOI: 10.1103/RevModPhys.62.541. URL: http://link.aps.org/doi/10.1103/RevModPhys.62.541.

[23] Helmut Hellwig et al. "Measurement of the Unperturbed Hydrogen Hyperfine Transition Frequency". In: *Instrumentation and Measurement, IEEE Transactions on* 19.4 (Nov. 1970), pp. 200–209. ISSN: 0018-9456. DOI: [10.1109/TIM.1970.4313902](10.1109/TIM.1970.4313902).

[24] L Essen et al. "Hydrogen Maser Work at the National Physical Laboratory". In: *Metrologia* 9.3 (1973), p. 128. URL: http://stacks.iop.org/0026-1394/9/i=3/a=004.

[25] G. Breit and I. I. Rabi. "Measurement of Nuclear Spin". In: *Phys. Rev.* 38 (11 Dec. 1931), pp. 2082–2083. DOI: 10.1103/PhysRev.38.2082.2. URL: http://link.aps.org/doi/10.1103/PhysRev.38.2082.2.

[26] I. I. Rabi. "On the Process of Space Quantization". In: *Phys. Rev.* 49 (4 Feb. 1936), pp. 324–328. DOI: 10.1103/PhysRev.49.324. URL: http://link.aps.org/doi/10.1103/PhysRev.49.324.

[27] Simone Gilardoni et al. *Fifty years of the CERN Proton Synchrotron: Volume 2*. Comments: 58 pages, published as CERN Yellow Report. Geneva: CERN, 2013. URL: https://cds.cern.ch/record/1597087.

[28] Ryugo Hayano. *ASACUSA STATUS REPORT - Recent progress and plans for 2016*. Tech. rep. CERN-SPSC-2016-001. SPSC-SR-174. Geneva: CERN, Jan. 2016. URL: https://cds.cern.ch/record/2119496.

[29] Y.Bylinsky, A.M.Lombardi and W. Pirkl. "RFQD: A 'Decelerating' Radiofrequency Quadrupole for the CERN antiproton facility". In: *Linac 2000*. Ed. by A. W. Chao. 2000, p. 554. URL: http://arxiv.org/abs/hep-ex/0008030.

[30] N. Kuroda et al. "Development of a monoenergetic ultraslow antiproton beam source for high-precision investigation". In: *Phys. Rev. ST Accel. Beams* 15 (2 Feb. 2012), p. 024702. DOI: 10.1103/PhysRevSTAB.15.024702. URL: http://link.aps.org/doi/10.1103/PhysRevSTAB.15.024702.

[31] H Imao et al. "Positron accumulation and manipulation for antihydrogen synthesis". In: *Journal of Physics: Conference Series* 225.1 (2010), p. 012018. URL: http://stacks.iop.org/1742-6596/225/i=1/a=012018.

[32] Yugo Nagata and Yasunori Yamazaki. "A novel property of anti-Helmholz coils for in-coil syntheses of antihydrogen atoms: formation of a focused spin-polarized beam". In: *New Journal of Physics* 16.8 (2014), p. 083026. URL: http://stacks.iop.org/1367-2630/16/i=8/a=083026.

[33] N Kuroda et al. "A source of antihydrogen for in-flight hyperfine spectroscopy". In: *Nature communications* 5 (2014). DOI: 10.1038/ncomms4089. URL: http://dx.doi.org/10.1038/ncomms4089.

[34] N Kuroda et al. "Towards a spin polarized antihydrogen beam". In: *Hyperfine Interactions* 228.1-3 (2014), pp. 67–76. DOI: 10.1007/s10751-014-1016-9. URL: http://dx.doi.org/10.1007/s10751-014-1016-9.

[35] Francis Robicheaux. "Three-body recombination for electrons in a strong magnetic field: Magnetic moment". In: *Physical Review A* 73.3 (2006), p. 033401. DOI: 10.1103/PhysRevA.73.033401. URL: http://journals.aps.org/pra/abstract/10.1103/PhysRevA.73.033401.

[36] B Radics et al. "Scaling behavior of the ground-state antihydrogen yield as a function of positron density and temperature from classical-trajectory Monte Carlo simulations". In: *Physical Review A* 90.3 (2014), p. 032704. DOI: 10.1103/PhysRevA.90.032704. URL: http://journals.aps.org/pra/abstract/10.1103/PhysRevA.90.032704.

[37] I. I. Rabi, J. M. B. Kellogg and J. R. Zacharias. "The Magnetic Moment of the Proton". In: *Phys. Rev.* 46 (3 Aug. 1934), pp. 157–163. DOI: 10.1103/PhysRev.46.157. URL: http://link.aps.org/doi/10.1103/PhysRev.46.157.

[38] I. I. Rabi, J. M. B. Kellogg and J. R. Zacharias. "The Magnetic Moment of the Deuton". In: *Phys. Rev.* 46 (3 Aug. 1934), pp. 163–165. DOI: 10.1103/PhysRev.46.163. URL: http://link.aps.org/doi/10.1103/PhysRev.46.163.

[39] Silke Federmann. "A Spin-Flip Cavity for Microwave Spectroscopy of Antihydrogen". PhD thesis. Universität Wien, 2012.

[40] S. Agostinelli et al. "Geant4—a simulation toolkit". In: *Nuclear Instruments and Methods in Physics Research Section A: Accelerators, Spectrometers, Detectors and Associated Equipment* 506.3 (2003), pp. 250–303. ISSN: 0168-9002. DOI: 10.1016/S0168-9002(03)01368-8. URL: http://www.sciencedirect.com/science/article/pii/S0168900203013688.

[41] J. Allison et al. "Geant4 developments and applications". In: *Nuclear Science, IEEE Transactions on* 53.1 (Feb. 2006), pp. 270–278. ISSN: 0018-9499. DOI: 10.1109/TNS. 2006.869826. URL: http://ieeexplore.ieee.org/xpl/articleDetails.jsp?arnumber= 1610988.

[42] R Lundmark et al. "Towards a precise measurement of the antihydrogen ground state hyperfine splitting in a beam: the case of in-flight radiative decays". In: *Journal of Physics B: Atomic, Molecular and Optical Physics* 48.18 (2015), p. 184001. DOI: 10.1088/0953-4075/48/18/184001. URL: http://stacks.iop.org/0953-4075/48/i=18/a=184001.

[43] Bernadette Kolbinger. "Numerical Simulations of Hyperfine Transitions in Antihydrogen". MA thesis. Uiversität Wien, 2014.

[44] B. Kolbinger et al. "Numerical simulations of hyperfine transitions of antihydrogen". In: *Hyperfine Interactions* 233.1 (2015), pp. 47–51. ISSN: 1572-9540. DOI: 10.1007/ s10751-015-1130-3. URL: http://dx.doi.org/10.1007/s10751-015-1130-3.

[45] C. Hagmann, D. Lange and D. Wright. "Cosmic-ray shower generator (CRY) for Monte Carlo transport codes". In: *Nuclear Science Symposium Conference Record, 2007. NSS '07. IEEE*. Vol. 2. Oct. 2007, pp. 1143–1146. DOI: 10.1109/NSSMIC.2007. 4437209. URL: http://ieeexplore.ieee.org/xpl/articleDetails.jsp?arnumber=4437209.

[46] M. Hori et al. "Analog Cherenkov detectors used in laser spectroscopy experiments on antiprotonic helium". In: *Nuclear Instruments and Methods in Physics Research Section A: Accelerators, Spectrometers, Detectors and Associated Equipment* 496.1 (2003), pp. 102–122. ISSN: 0168-9002. DOI: 10.1016/S0168-9002(02)01618-2. URL: http://www.sciencedirect.com/science/article/pii/S0168900202016182.

[47] James S Cohen. "Capture of negative exotic particles by atoms, ions and molecules". In: *Reports on Progress in Physics* 67.10 (2004), p. 1769. URL: http://stacks.iop.org/ 0034-4885/67/i=10/a=R02.

[48] A. Trzci ńska et al. "Neutron Density Distributions Deduced from Antiprotonic Atoms". In: *Phys. Rev. Lett.* 87 (8 Aug. 2001), p. 082501. DOI: 10.1103/PhysRevLett. 87.082501. URL: http://link.aps.org/doi/10.1103/PhysRevLett.87.082501.

[49] A. Trzcińska W. J. Świąteck and and J. Jastrzębski. "Difference of the root-mean-square sizes of neutron and proton distributions in nuclei: Comparison of theory with data". In: *Phys. Rev. C* 71 (4 Apr. 2005), p. 047301. DOI: 10.1103/PhysRevC.71. 047301. URL: http://link.aps.org/doi/10.1103/PhysRevC.71.047301.

[50] J. Hüfner and M. Thies. "Pion-nucleus scattering and absorption as a solution of the Boltzmann equation". In: *Phys. Rev. C* 20 (1 July 1979), pp. 273–285. DOI: 10.1103/PhysRevC.20.273. URL: http://link.aps.org/doi/10.1103/PhysRevC.20.273.

[51] J. Cugnon and J. Vandermeulen. "Transfer of energy following p̄-annihilation on nuclei". In: *Nuclear Physics A* 445.4 (1985), pp. 717–736. ISSN: 0375-9474. DOI: 10.1016/0375-9474(85)90568-8. URL: http://www.sciencedirect.com/science/article/pii/0375947485905688.

[52] J. Cugnon, P. Jasselette and J. Vandermeulen. "Nucleus excitation and deexcitation following p-annihilation at rest". In: *Nuclear Physics A* 470.3–4 (1987), pp. 558–572. ISSN: 0375-9474. DOI: 10.1016/0375-9474(87)90587-2. URL: http://www.sciencedirect.com/science/article/pii/0375947487905872.

[53] J. Cugnon et al. "Geometrical effects in antiproton annihilation on nuclei". In: *Phys. Rev. C* 63 (2 Jan. 2001), p. 027301. DOI: 10.1103/PhysRevC.63.027301. URL: http://link.aps.org/doi/10.1103/PhysRevC.63.027301.

[54] Alan C Hindmarsh. "ODEPACK, A Systematized Collection of ODE Solvers". In: *Scientific Computing*. Ed. by R. S. Stepleman et al. Vol. 1. IMACS transactions on scientific computation. Elsevier, 1983, pp. 55–64. URL: https://computation.llnl.gov/casc/nsde/pubs/u88007.pdf.

[55] Peter N. Brown, George D. Byrne and Alan C. Hindmarsh. "VODE: A Variable-Coefficient ODE Solver". In: *SIAM Journal on Scientific and Statistical Computing* 10.5 (1989), pp. 1038–1051. DOI: 10.1137/0910062. eprint: http://dx.doi.org/10.1137/0910062. URL: http://dx.doi.org/10.1137/0910062.

[56] S. van der Walt, S.C. Colbert and G. Varoquaux. "The NumPy Array: A Structure for Efficient Numerical Computation". In: *Computing in Science Engineering* 13.2 (Mar. 2011), pp. 22–30. ISSN: 1521-9615. DOI: 10.1109/MCSE.2011.37. URL: http://ieeexplore.ieee.org/xpl/articleDetails.jsp?arnumber=5725236.

[57] Eric Jones, Travis Oliphant, Pearu Peterson et al. *SciPy: Open source scientific tools for Python*. [Online; accessed 2016-01-28]. 2001–. URL: http://www.scipy.org/.

[58] Martin Diermaier. PhD thesis. Technische Universität Wien, 2016.

[59] M. Diermaier et al. "An atomic hydrogen beam to test ASACUSA's apparatus for antihydrogen spectroscopy". In: *Hyperfine Interactions* 233.1 (2015), pp. 35–40. ISSN: 1572-9540. DOI: 10.1007/s10751-015-1151-y. URL: http://dx.doi.org/10.1007/s10751-015-1151-y.

[60] C. Malbrunot et al. "Spectroscopy apparatus for the measurement of the hyperfine structure of antihydrogen". In: *Hyperfine Interactions* 228.1 (2014), pp. 61–66. ISSN: 1572-9540. DOI: 10.1007/s10751-014-1013-z. URL: http://dx.doi.org/10.1007/s10751-014-1013-z.

[61] C B Jepsen. "Work Project Report by C. B. Jepsen". In: *CERN CDS* (Aug. 2014). URL: https://cds.cern.ch/record/1752579.

[62] Clemens Sauerzopf et al. "Intelligent Front-end Electronics for Silicon photodetectors (IFES)". In: *Nuclear Instruments and Methods in Physics Research Section A: Accelerators, Spectrometers, Detectors and Associated Equipment* 819 (2016), pp. 163–166. ISSN: 0168-9002. DOI: 10.1016/j.nima.2016.02.098. URL: http://www.sciencedirect.com/science/article/pii/S0168900216300158.

[63] Y Nagata, C Sauerzopf, A Capon et al. "The development of the antihydrogen beam detector and the detection of the antihydrogen atoms for in-flight hyperfine spectroscopy". In: *Journal of Physics: Conference Series* 635.2 (2015), p. 022061. DOI: 10.1088/1742-6596/635/2/022061. URL: http://stacks.iop.org/1742-6596/635/i=2/a=022061.

[64] Aaron Capon. "Construction of a scintillating hodoscope detector for measurements on the hyperfine splitting of antihydrogen". MA thesis. Universität Wien, 2015.

[65] Stefan Ritt. "Design and performance of the 6 GHz waveform digitizing chip DRS4". In: *Nuclear Science Symposium Conference Record, 2008. NSS '08. IEEE*. Oct. 2008, pp. 1512–1515. DOI: 10.1109/NSSMIC.2008.4774700. URL: http://ieeexplore.ieee.org/xpl/articleDetails.jsp?arnumber=4774700.

[66] *90V Boost DC/DC Converter with APD Current Monitor, LT3482*. LT 0207 REV A. Linear Technology. 2007.

[67] *Pin-/Software-Compatible, 16-/12-Bit, Voltage-Output DACs, MAX5134-MAX5137*. 19-4209; Rev 2; Maxim Integrated. Jan. 2010.

[68] *Low Distortion Differential RF/IF Amplifier, AD8351*. Rev B. Analog Devices. Feb. 2004.

[69] P. Jarron et al. "Time based readout of a silicon photomultiplier (SiPM) for Time Of Flight Positron Emission Tomography (TOF-PET)". In: *IEEE Nuclear Science Symposium Conference Record* 58.3 (Apr. 2009), pp. 567–604. DOI: 10.1109/NSSMIC.2009.5402391. URL: http://ieeexplore.ieee.org/xpl/articleDetails.jsp?arnumber=5402391.

[70] F. Anghinolfi et al. "NINO: an ultrafast low-power front-end amplifier discriminator for the time-of-flight detector in the ALICE experiment". In: *IEEE Transactions on Nuclear Science* 51.5 (Oktober 2004), pp. 1974–1978. D O I: [10.1109/TNS.2004.836048](). U R L: [http://ieeexplore.ieee.org/xpl/articleDetails.jsp?arnumber=1344270]().

[71] S E Brunner et al. "Time resolution below 100 ps for the SciTil detector of PANDA employing SiPM". In: *Journal of Instrumentation* 9.03 (2014), p. C03010. U R L: [http://stacks.iop.org/1748-0221/9/i=03/a=C03010]().

[72] L. Gruber. "Studies of SiPM photosensors for time-of-flight detectors within PANDA at FAIR". PhD thesis. Technische Universität Wien, 2014.

[73] Clemens Sauerzopf. *waveformlibrary v1.0.0.* Dec. 2015. D O I: [10.5281/zenodo.35341](). U R L: [http://dx.doi.org/10.5281/zenodo.35341]().

[74] Rene Brun and Fons Rademakers. "ROOT — An object oriented data analysis framework". In: *Nuclear Instruments and Methods in Physics Research Section A: Accelerators, Spectrometers, Detectors and Associated Equipment* 389.1–2 (1997). New Computing Techniques in Physics Research V, pp. 81–86. I S S N: 0168-9002. D O I: [10.1016/S0168-9002(97)00048-X](). U R L: [http://www.sciencedirect.com/science/article/pii/S016890029700048X]().

[75] Noel Dawe et al. *rootpy: 0.8.0.* June 2015. D O I: [10.5281/zenodo.18897](). U R L: [http://dx.doi.org/10.5281/zenodo.18897]().

[76] *AR9331 Highly-Integrated and Cost Effective IEEE 802.11n 1x1 2.4 GHz SoC for AP and Router Platforms.* Atheros. Dec. 2010.

[77] *SIS 1100/3100 PCI/cPCI-VME link/interface manual.* Struck innovative systeme. Mar. 2008.

[78] *V1742, Technical information manual.* 6th ed. CAEN Nuclear Instruments. Feb. 2012.

[79] K. A. Olive et al. "Review of Particle Physics". In: *Chin. Phys.* C38 (2014). Particle Data Group (PDG), p. 090001. D O I: [10.1088/1674-1137/38/9/090001](). U R L: [http://dx.doi.org/10.1088/1674-1137/38/9/090001]().

[80] Harold Jeffreys. "The Theory of Probability". In: 3rd. Oxford, 1961, p. 432.

[81] John K. Kruschke. "Bayesian estimation supersedes the t test". In: *Journal of Experimental Psychology: General* 142(2) (May 2013), pp. 573–603. D O I: [10.1037/a0029146](). U R L: [http://dx.doi.org/10.1037/a0029146]().

[82] Harold Jeffreys. "An Invariant Form for the Prior Probability in Estimation Problems". In: *Proceedings A of The Royal Society* 186(1007) (Sept. 1946). D O I: [10.1098/rspa.1946.0056](). U R L: [http://dx.doi.org/10.1098/rspa.1946.0056]().

[83] Jonathan Goodman and Jonathan Weare. "Ensemble samplers with affine invariance". In: *Communications in Applied Mathematics and Computational Science* 5.1 (Jan. 2010). DOI: 10.2140/camcos.2010.5.65. URL: http://dx.doi.org/10.2140/camcos.2010.5.65.

[84] Daniel Foreman-Mackey et al. "emcee: The MCMC Hammer". In: *Publications of the Astronomical Society of the Pacific* 125.925 (2013), pp. 306–312. ISSN: 00046280, 15383873. DOI: 10.1086/670067. URL: http://www.jstor.org/stable/10.1086/670067.

[85] Jacob Cohen. "Statistical Power Analysis for the Behavioral Scinces". In: 2nd. Lawrence Erlbaum Associates Inc, 1988, p. 25.

[86] David Freedman and Persi Diaconis. "On the histogram as a density estimator:L^2 theory". In: *Zeitschrift für Wahrscheinlichkeitstheorie und Verwandte Gebiete* 57.4 (1981), pp. 453–476. ISSN: 1432-2064. DOI: 10.1007/BF01025868. URL: http://dx.doi.org/10.1007/BF01025868.

[87] N. Kuroda et al. "The ASACUSA CUSP: an antihydrogen experiment". In: *Hyperfine Interactions* 235.1 (2015), pp. 13–20. ISSN: 1572-9540. DOI: 10.1007/s10751-015-1205-1. URL: http://dx.doi.org/10.1007/s10751-015-1205-1.

Curriculum vitae

Clemens Sauerzopf

Nationality	Austrian
Date of birth	17th December 1986
E-mail	contact@csauerzopf.at

Employment

Stefan Meyer Institute, Austrian Academy of Sciences

Duration	since March 2012
Position	Researcher
Additional responsibilities	System administrator for GNU/Linux and FreeBSD servers, OpenAccess officer
Secondary workplace	Organisation Européenne pour la Recherche Nucléaire (CERN)

Scientific community

September 2015 – February 2016 President of the ÖPG Young Minds section of the EPS Young Minds

January 2015 – September 2015 Chairperson of the Austrian physical society students working group

Education

Doctoral study Technical Physics   **PhD**

Focus	Particle physics, anti-matter, precision physics, computational physics, statistical data analysis
Research institute	Stefan Meyer Institute for Subatomic Physics of the Austrian Academy of Sciences
University	Technische Universität Wien
Funded by	ERC Advanced Grant of Prof. Widmann Doctoral college Particles and Interactions – DK-PI
Supervisor	Prof. Eberhard Widmann
Duration	since March 2012

Master Program Technical Physics, passed with distinction   **MSc**

Acquired grade	Diplom-Ingenieur (equivalent to "Master of Science")
Focus	Particle physics, atomic / subatomic physics precision physics
University	Technische Universität Wien
Duration	February 2010 – January 2012

Bachelor Technical Physics   **BSc**

Acquired grade	Bachelor of Science
University	Technische Universität Wien
Duration	October 2006 – February 2010

Bundesgymnasium und Bundesrealgymnasium Neusiedl am See

Name of acquired qualification	Matura
Type of education	Realgymnasium with descriptive geometry and French
Duration	September 1998 – June 2005

Peer-reviewed scientific publications

- Clemens Sauerzopf et al. "Intelligent Front-end Electronics for Silicon photodetectors (IFES)". in: *Nuclear Instruments and Methods in Physics Research Section A: Accelerators, Spectrometers, Detectors and Associated Equipment* 819 (2016), pp. 163–166. ISSN: 0168-9002. DOI: 10.1016/j.nima.2016.02.098. URL: http://www.sciencedirect.com/science/article/pii/S0168900216300158

- N. Kuroda et al. "The ASACUSA CUSP: an antihydrogen experiment". In: *Hyperfine Interactions* 235.1 (2015), pp. 13–20. ISSN: 1572-9540. DOI: 10.1007/s10751-015-1205-1. URL: http://dx.doi.org/10.1007/s10751-015-1205-1

- R Lundmark et al. "Towards a precise measurement of the antihydrogen ground state hyperfine splitting in a beam: the case of in-flight radiative decays". In: *Journal of Physics B: Atomic, Molecular and Optical Physics* 48.18 (2015), p. 184001. DOI: 10.1088/0953-4075/48/18/184001. URL: http://stacks.iop.org/0953-4075/48/i=18/a=184001

- Y Nagata, C Sauerzopf, A Capon et al. "The development of the antihydrogen beam detector and the detection of the antihydrogen atoms for in-flight hyperfine spectroscopy". In: *Journal of Physics: Conference Series* 635.2 (2015), p. 022061. DOI: 10.1088/1742-6596/635/2/022061. URL: http://stacks.iop.org/1742-6596/635/i=2/a=022061

- M. Diermaier et al. "An atomic hydrogen beam to test ASACUSA's apparatus for antihydrogen spectroscopy". In: *Hyperfine Interactions* 233.1 (2015), pp. 35–40. ISSN: 1572-9540. DOI: 10.1007/s10751-015-1151-y. URL: http://dx.doi.org/10.1007/s10751-015-1151-y

- B. Kolbinger et al. "Numerical simulations of hyperfine transitions of antihydrogen". In: *Hyperfine Interactions* 233.1 (2015), pp. 47–51. ISSN: 1572-9540. DOI: 10.1007/s10751-015-1130-3. URL: http://dx.doi.org/10.1007/s10751-015-1130-3

- N Kuroda et al. "Towards a spin polarized antihydrogen beam". In: *Hyperfine Interactions* 228.1-3 (2014), pp. 67–76. DOI: 10.1007/s10751-014-1016-9. URL: http://dx.doi.org/10.1007/s10751-014-1016-9

- C. Malbrunot et al. "Spectroscopy apparatus for the measurement of the hyperfine structure of antihydrogen". In: *Hyperfine Interactions* 228.1 (2014), pp. 61–66. ISSN: 1572-9540. DOI: 10.1007/s10751-014-1013-z. URL: http://dx.doi.org/10.1007/s10751-014-1013-z

- N Kuroda et al. "A source of antihydrogen for in-flight hyperfine spectroscopy". In: *Nature communications* 5 (2014). DOI: 10.1038/ncomms4089. URL: http://dx.doi.org/10.1038/ncomms4089

- E. Widmann et al. "Measurement of the hyperfine structure of antihydrogen in a beam". In: *Hyperfine Interactions* 215.1 (2013), pp. 1–8. ISSN: 1572-9540. DOI: 10.1007/s10751-013-0809-6. URL: http://dx.doi.org/10.1007/s10751-013-0809-6

- G Konrad et al. "Neutron Decay with PERC: a Progress Report". In: *Journal of Physics: Conference Series* 340.1 (2012), p. 012048. DOI: 10.1088/1742-6596/340/1/012048. URL: http://stacks.iop.org/1742-6596/340/i=1/a=012048

Conference contributions

February 2016, Austria "A Detector For In-Beam Measurement of the Ground State Hyperfine Splitting of Antihydrogen" , *14th Vienna Conference on Instrumentation – VCI2016*, Vienna, Austria, oral contribution

September 2015, Austria "Progress towards measuring the ground state hyperfine splitting of antihydrogen" , *ÖPG/SPS annual meeting,* Vienna, Austria, oral contribution

June 2015, USA "A detector for in-beam measurements of the ground state hyperfine splitting of antihydrogen" , *IUCSS summer school*, Bloomington, Indiana, USA, poster

June 2015, Canada "Towards measuring the ground state hyperfine splitting of antihydrogen - a progress report" , *6th International Symposium on Symmetries in Subatomic Physics – SSP2015*, Victoria, Canada, poster and talk, DOI: 10.5281/zenodo.35348

December 2014, Switzerland "Hbar HFS DAQ system 2014 and online data analysis"
, *ASACUSA collaboration meeting*, CERN, Switzerland, oral contribution

September 2014, Austria "Measuring the ground state hyperfine structure of anti-
hydrogen", *ÖPG annual meeting*, Pöllau, Austria, oral contribution

September 2014, Austria "A detector for in-beam measurements of the groundstate
hyperfine structure of antihydrogen", *International Conference on Exotic Atoms and
Related Topics – EXA2014*, Vienna, Austria, poster, DOI: 10.5281/zenodo.35338

May 2014, Germany "Simulations for the measurement of the groundstate hyperfines-
tructure of antihydogen", *FLAIR workshop*, Heidelberg, Germany, poster, DOI: 10.
5281/zenodo.35334

December 2013, Austria "Developments in simulations for the hyperfine spectroscopy
of antihydrogen", *ASACUSA collaboration meeting*, Vienna, Austria, oral contribu-
tion

September 2013, Austria "A progress report on detector and analysis development for
the Hbar-HFS experiment within the ASACUSA collaboration", *ÖPG/SPS annual
meeting*, Linz, Austria, oral contribution

October 2012, Japan "The CPT detector and Geant4 simulations", *CUSP goup meeting*,
Tokyo, Japan, oral contribution

September 2012, Austria "Measuring the hyperfine-splitting of Antihydrogen", *ÖPG
annual meeting*, Graz, Austria, oral contribution

Academic theses

Master's thesis "Installation and commissioning of a detector system for the Neutron
beta decay", *Atominstitut, Technische Universität Wien*, supervised by Prof. Abele,
2011

Bachelor's thesis "Analysis of isomere states in lead on the basis of prompt gamma
spectra", *Atominstitut, Technische Universität Wien*, supervised by Dr. Jericha, 2009